On the Development of Memsensors

Dissertation
by
Alexander Vahl

submitted to obtain the degree of
Doctor of Engineering (Dr.-Ing.)
at the
Faculty of Engineering, Kiel University
Institute for Material Science

First Supervisor:	Prof. Dr. Franz Faupel *Chair for Multicomponent Materials* Faculty of Engineering, Kiel University
Second Supervisor:	Prof. Dr. Lorenz Kienle *Chair for Synthesis and Real Structure* Faculty of Engineering, Kiel University
Third Supervisor:	Prof. Dr. Paolo Milani *Fisica Sperimentale della Materia* Dipartimento di Fisica, Universitá degli Studi di Milano

Date of Disputation
August 19th 2019

Declaration of Authorship

I hereby declare that this thesis and the respective research was independently composed and authored by myself.

This work complies with the DFG recommendations for safeguarding good scientific practice. All content and ideas drawn directly or indirectly from external sources are clearly indicated.

This thesis has not been published or been submitted to any other examining body and all related research items that have been composed and published in peer-review journals are clearly indicated as such.

I declare that no academic degree has been withdrawn from me.

_____

Kiel, 06.05.2019

Acknowledgements - Danksagungen

Reich ist nicht der, der viele Kerzen hat,
sondern der, dessen Weg auch im Sturm erleuchtet wird.
in Memoriam: Horst Mamerow † 19.03.2018

Mein Dank gilt allen voran Franz, der mir die Möglichkeit zur Anfertigung dieser Arbeit gegeben hat und mir so einen Einblick in dieses spannende, interdisziplinäre Forschungsgebiet ermöglicht hat. Durch seine Unterstützung und Vertrauen entstand eine besondere Arbeitsumgebung, die einen großen Anteil an den in dieser Arbeit entstandenen Ergebnissen hat.

Weiterhin möchte ich mich bei allen Kollegen aus dem Umfeld der Arbeitsgruppe, der TF allgemein und der Forschergruppe 2093 bedanken, die mich in den letzten Jahren begleitet haben und durch ihre Kreativität, Aufgeschlossenheit und eine Vielzahl an spannenden Gesprächen für ein wundervolles Arbeitsumfeld gesorgt haben. Ein großer Dank geht in diesem Zusammenhang an die Bürogemeinschaft aus dem Büro A-026, die neben dem üblichen Büroalltag auch stets für die eine oder andere Unternehmung zu motivieren war. Besonders danken möchte ich auch Nico, Wiebke und Jan, die als Master- bzw. Bachelorstudenten meine Arbeit persönlich und wissenschaftlich bereichert haben, sowie meinen Doktoranden-Buddies aus der Forschergruppe, allen voran Sven, Victor, Niko und Julian. In vielen Diskussionen ist über die Jahre eine fruchtbare Kooperation und Freundschaft entstanden, bei der die Zusammenarbeit sogar in einem Hecht-Angeln auf einer schwedischen Insel mündete. Außerdem möchte ich mich bei Klaus, Niko, Sven, Jonas und Sascha bedanken, die durch ihr prüfendes Auge die eine oder andere Verbesserung an dieser Arbeit ermöglicht haben.

Ein besonderer Dank gilt ebenso Stefan Rehders und den zentralen Werkstätten der Technischen Fakultät (unter der Federführung von Berndt Neumann), die mich bei der Planung und Umsetzung von experimentellen Anlagen stets außerordentlich kompetent und freundlich unterstützt haben und bei denen auch ausgefallene Ideen nie auf taube Ohren stießen.

Ein großer Dank gilt auch meiner Familie und meinen Freunden, die mich während des Studiums begleitet haben und deren Gesellschaft mir neben Freude und Motivation auch stets das nötige Maß an Ablenkung geboten hat, wodurch ich die Zeit der Promotion auch ganz besonders durch die vielen schönen Momente abseits des Schreibtisches in guter Erinnerung behalten werde.

Zu guter Letzt möchte ich mich ganz besonders bei meinen Eltern, Angela und Uwe, sowie meiner Freundin Claudia bedanken, die mir stets großen Rückhalt gegeben haben und mir mit Rat und Tat während der Promotion zur Seite standen.

Publications in the Context of this Dissertation

in chronological order, first or equally contributing authors are underlined

[A] **A. Vahl**, J. Strobel, W. Reichstein, O. Polonskyi, T. Strunskus, L. Kienle, F. Faupel, *Single target sputter deposition of alloy nanoparticles with adjustable composition via a gas aggregation cluster source*, Nanotechnology. 28 (2017) 175703. doi:10.1088/1361-6528/aa66ef.

[B] B. Henkel, **A. Vahl**, O.C. Aktas, T. Strunskus, F. Faupel, *Self-organised nanocrack networks: A pathway to enlarge catalytic surface area in sputtered ceramic thin films, showcased for photocatalytic TiO_2*, Nanotechnology. 29 (2018). doi:10.1088/1361-6528/aa9d35.

[C] V. Postica, **A. Vahl**, J. Strobel, D. Santos-Carballal, O. Lupan, A. Cadi-Essadek, N.H. de Leeuw, F. Schütt, O. Polonskyi, T. Strunskus, M. Baum, L. Kienle, R. Adelung, F. Faupel, *Tuning doping and surface functionalization of columnar oxide films for volatile organic compound sensing: experiments and theory*, J. Mater. Chem. A. (2018) 21–27. doi:10.1039/C8TA08985J.

[D] V. Postica, **A. Vahl**, N. Magariu, M.-I. Terasa, M. Hoppe, B. Viana, P. Aschehoug, T. Pauporté, I. Tiginyanu, O. Polonskyi, V. Sontea, L. Chow, L. Kienle, R. Adelung, F. Faupel, O. Lupan, *Enhancement in UV Sensing Properties of ZnO:Ag Nanostructured Films by Surface Functionalization with Noble Metallic and Bimetallic Nanoparticles*, Journal of Engineering Science. 3 (2019) 41-51. doi:10.5281/zenodo.2557280.

[E] K. K. Neelisetty, X. Mu, S. Gutsch, **A. Vahl**, A. Molinari, F. v. Seggern, M. Hansen, T. Scherer, M. Zacharias, L. Kienle, V. S. K. Chakravadhanula, C. Kübel, *Electron beam effects on oxide thin films – Structure and electrical properties*, Microscopy and Microanalysis. (2019) 1-9. doi:10.1017/S1431927619000175

[F] **A. Vahl**, J. Carstensen, S. Kaps, O. Lupan, T. Strunskus, R. Adelung, F. Faupel, *Concept and modelling of memsensors as two terminal devices with enhanced capabilities in neuromorphic engineering*, Scientific Reports. 9 (2019) 4361. doi: 10.1038/s41598-019-39008-5.

[G] **A. Vahl**, J. Dittmann, J. Jetter, S. Veziroglu, S. Shree, N. Ababii, O. Lupan, O. C. Aktas, T. Strunskus, E. Quandt, R. Adelung, S. K. Sharma, F. Faupel, *Reactive sputtering of metal oxide thin films: The impact of O_2/Ar ratio on thin film morphology*, Nanotechnology. 30 (2019) 235603. doi:10.1088/1361-6528/ab0837.

Further Publications

in chronological order, first or equally contributing authors are underlined

[H] M.Z. Ghori, S. Veziroglu, B. Henkel, **A. Vahl**, O. Polonskyi, T. Strunskus, F. Faupel, O.C. Aktas, *A comparative study of photocatalysis on highly active columnar TiO_2 nanostructures in-air and in-solution*, Solar Energy Materials and Solar Cells. 178 (2018). doi:10.1016/j.solmat.2018.01.019.

[I] S. Veziroglu, K. Röder, O. Gronenberg, **A. Vahl**, O. Polonskyi, T. Strunskus, H.-G. Rubahn, L. Kienle, J. Adam, J. Fiutowski, F. Faupel, O.C. Aktas, *Cauliflower-like CeO_2-TiO_2 Hybrid Nanostructures with Extreme Photocatalytic and Self-Cleaning Properties*, Nanoscale. *in print* (2019). doi: 10.1039/C9NR01208G.

[J] M. Hoppe, N. Magariu, V. Cretu, O. Polonskyi, B. Viana, M. Ulfa, V. Postica, R. Adelung, V. Sontea, M.-I. Terasa, F. Faupel, **A. Vahl**, S. Shree, T. Pauporte, N. Ababii, *Effect of noble metal functionalization and film thickness on sensing properties of sprayed TiO_2 ultra-thin films*, Sensors & Actuators: A. *in print* (2019).

Zusammenfassung

Die Jahre seit der Erfindung des Transistors sind gekennzeichnet durch ein stetiges Wachstum der Komplexität und Bedeutung von digitalen Rechnern, angefeuert unter anderem durch fortschreitende Miniaturisierung. Neue Algorithmen, wie beispielsweise „Deep Learning“, erweitern stetig die Funktionalitäten, unter anderem im Bereich Bilderkennung. Neuronale Netze, wie beispielsweise das Gehirn, können derartige komplexe Aufgabenstellungen mit erstaunlicher Effizienz abarbeiten. Die zugrunde liegende Architektur mit über Synapsen hochvernetzten Neuronen steht in deutlichem Kontrast zur von-Neumann-Architektur siliziumbasierter Rechensysteme. Im Zuge der Suche nach neuartigen, energieeffizienten, biologisch motivierten Rechnerarchitekturen wird Memristoren eine besondere Beachtung zuteil. Seit der Verknüpfung von memristiven Bauelementen mit dem resistiven Schalten von TiO_2-basierten Dünnfilmen im Jahr 2008 wurden diverse Konzepte zur Herstellung memristiver Bauteile verfolgt und die zugrunde liegenden Schaltungsmechanismen untersucht. Aus der Vielzahl der Konzepte stechen besonders metallionen-basierte Bauteile heraus, in denen die feldgetriebene Bewegung mobiler Metallionen (wie beispielsweise Silber-Ionen) zur reversiblen Ausbildung leitfähiger Pfade führt und somit der elektrische Widerstand des Bauteils kontrolliert geschaltet werden kann. Memristive Bauelemente werden unter dem Gesichtspunkt einer Anwendung als potentielle neuartige Speichermedien untersucht und zudem in den Kontext effizienter, biologisch motivierter Rechenkonzepte gestellt. Neben den großen Fortschritten in der Anwendung von memristiven Bauteilen, beispielsweise im Bereich „In-Memory Computing“ oder zur Nachbildung der Änderung der synaptischen Kopplung zweier Neuronen, blieb ein Aspekt neuronaler Systeme bislang größtenteils unbeachtet: Die Verbindung zwischen der Detektion von Umweltsignalen und der direkten Auswertung dieser Signale. Die enge Kopplung dieser Prozesse in biologischen neuronalen Netzwerken, beispielsweise durch Adaption, ist ein essentieller Baustein für die hohe Effizienz. In diesem Kontext erscheinen Memsensoren, also Bauteile, die memristive und sensitive Eigenschaften vereinen, als verheißungsvoller neuer Forschungsbereich.

Im Rahmen dieser Arbeit wurden Konzepte für Memsensoren erarbeitet, in denen sowohl memristives Schalten als auch eine Änderung des Widerstands in Abhängigkeit eines externen Stimulus genutzt werden, um biologisch motivierte Funktionen und Eigenschaften neuronaler Netze nachzustellen. Mithilfe einer numerischen Simulation konnte gezeigt werden, dass Memsensoren Adaption gegenüber externen Stimuli aufweisen können. In ZnO-basierten Bauelementen wurde memristives Schalten nachgewiesen, das durch das Anlegen eines externen Stimulus in Form von UV-Licht moduliert werden kann. Für die Umsetzung der entwickelten Memsensor-Konzepte wurden im Rahmen dieser Arbeit memristive Bauelemente hergestellt und charakterisiert sowie nanostrukturierte Sensoren für die Detektion von UV-Licht und Gasmolekülen untersucht.

Die Grundlage der nanostrukturierten Sensoren bildeten halbleitende Metall-Oxid-Dünnschichten. In diesem Zusammenhang wurde die vakuumbasierte Methode der Kathodenzerstäubung (in Anwesenheit von reaktivem Sauerstoff) zur Abscheidung von Titandioxid und Kupferoxid angewandt. Durch eine gezielte Wahl des Sauerstoff-Anteils während des Depositionsprozesses sowie eine anschließende Temperaturbehandlung konnten säulenartige Nanostrukturen mit definierten Rissen zwischen einzelnen Säulen erzielt werden. Ein hoher Sauerstoff-Anteil erwies sich dabei als vorteilhaft, um beispielsweise separierte CuO-Säulen-Strukturen mit einem Durchmesser von etwa 20 nm zu erzielen. Die so erhaltenen Nanostrukturen erwiesen sich als sensitiv gegenüber organischen Gas-Spezies (beispielsweise Butanol). Um eine weitere Steigerung der Sensitivität und Selektivität der untersuchten Gas-Sensoren zu erzielen, wurden die nanostrukturierten Dünnfilme zudem mit metallischen Nanopartikeln beschichtet.

Als Ansatz für die Herstellung und Untersuchung memristiver Bauelemente wurde die feldgetriebene Bewegung von Metallkationen in einer dielektrischen Matrix gewählt. Aufbauend auf diesem Konzept wurden in dieser Thesis nanopartikelbasierte memristive Bauelemente entwickelt, bei denen einzelne silberhaltige Nanopartikel in eine isolierende SiO_2-Matrix eingebunden wurden. Gegenüber herkömmlichen memristiven Bauelementen mit planaren Elektroden bietet die Einbeziehung von Nanopartikeln den Vorteil, dass die Abstände zwischen den einzelnen Partikeln frei einstellbar sind und sich durch die lokale Feldverstärkung zwischen den Nanopartikeln definierte Pfade vorgeben lassen, wodurch die Notwendigkeit eines Formier-Prozesses potentiell vermieden werden kann. Der Übergang zu Legierungspartikeln des Systems AgAu und AgPt eröffnet hierbei weitere Möglichkeiten: Zum einen kann deren Gold- oder Platin-Komponente als stabiler Anker in der Matrix dienen. Zum anderen bietet eine gezielte Wahl der Nanopartikel-Zusammensetzung die Möglichkeit, die Verfügbarkeit mobiler Silber-Ionen zu steuern. Für die Herstellung der Legierungspartikel wurde das Verfahren der „Gas Aggregation Source“ um eine neuartige Target-Geometrie erweitert. Mit dieser Änderung war es möglich, Legierungspartikel des Systems AgAu mit einstellbaren Zusammensetzungen und einem Durchmesser von etwa 10 nm zu erzeugen. Memristive Dünnschichtbauelemente auf der Basis dieser Legierungs-partikel wurden mikroskopisch mittels Rasterkraftmikroskopie mit leitfähiger Spitze und makroskopisch mittels Zwei-Punkt-Messungen elektrisch charakterisiert. Die nanopartikel-basierten memristiven Bauelemente zeigen über viele Zyklen hinweg diffuses memristives Schaltverhalten mit zwei definierten Widerstands-Zuständen, die abhängig von der Schichtfolge und den verwendeten Nanopartikeln eingestellt werden konnten. Die statistische Analyse der Setz- und Rücksetzspannungen ergab ein klares Arbeitsfenster, in dem ein Schalten zwischen beiden Zuständen möglich ist.

Die Untersuchungen zum Konzept von Memsensoren sowie zu experimentell realisierten Sensoren und memristiven Bauelementen als mögliche Memsensor-Komponenten haben gezeigt, dass Memsensoren das Potential haben, Signaldetektion und Signalverarbeitung eng zu verknüpfen und somit einen interessanten Ansatz zur Entwicklung fortschrittlicher, effizienter Schaltungskonzepte darstellen.

Summary

Since the discovery of the transistor, digital computing architectures have steadily gained complexity and impact on society, with the unprecedented progress in transistor-based computing being mainly driven by miniaturization. Modern computational techniques like deep learning are constantly expanding the application purposes, for example in the field of pattern separation and completion. In the biological context, neural networks are capable of accomplishing such complex tasks with outstanding efficiency. The underlying architecture is based on a complex network of neurons, highly connected by synapses. This paradigm is in strong contrast to the von-Neumann architecture of modern silicon-based systems. Alongside the exploration of novel, biologically motivated computing architectures with high efficiency, memristive devices have gained considerable attention. Since the postulation of the experimental realization of memristive devices in 2008, a broad variety of concepts for the fabrication of memristive devices has been pursued and the underlying switching mechanisms have been studied in detail. Special interest is paid to memristive devices relying on the reversible formation of a conductive path upon field-driven motion of mobile metal cations (e.g. silver cations) between two electrodes. Despite their potential application as novel memory devices, the high research interest in memristive devices is also driven by their applicability in the context of efficient, biologically motivated computing architectures. Although in the past decade there have been extensive studies, e.g. regarding in-memory computing or mimicking synaptic plasticity, one particular aspect of complex neural systems remains rather disregarded: The connection between sensing (detecting environmental signals) and data processing (e.g. by memristive switching). In biological neural networks, however the incoming data are processed already at the location of data detection (e.g. by adaptation), which is an essential contribution to the high efficiency of neural networks. In this context, memsensors as devices combining memristive and sensitive functionalities emerge as a promising research field.

In the framework of this thesis, concepts for memsensors were developed with a focus on enabling advanced neuromorphic functionalities by merging memristive switching and stimulus dependent resistivity. Applying a numerical simulation, it could be demonstrated that memsensors are capable of showing adaptation behaviour towards the external stimulus. In ZnO based devices, the extent of memristive switching was observed to depend on the applied external stimulus (UV light). In order to pave the way towards an experimental realization of the memsensor concepts developed in this thesis, on the one hand memristive devices were fabricated and thoroughly characterised and on the other hand sensing of UV-light and gas molecules was studied in nanostructured thin films.

Thin films of semiconducting metal oxides (e.g. TiO_2, CuO) were studied in the context of their applicability as sensors for UV-light and gas molecules. To that end, the vacuum-based deposition method of magnetron sputtering in the presence of reactive O2 gas was employed in order to deposit thin films with tailored morphologies. Nanostructured thin films with well-defined crack networks between individual metal oxide columns were obtained by tuning the composition of the oxygen/argon mixture during the deposition process and

performing a post deposition heat treatment step. A high oxygen content in the reactive gas atmosphere turned out to be advantageous, e.g. for the formation of well separated CuO columns with a diameter of 20 nm. The nanostructured CuO thin films prepared using this approach exhibited a high sensitivity towards volatile organic compounds such as butanol. For a further enhancement of the sensor's sensitivity and selectivity, the interplay between nanostructured thin films and metallic nanoparticles was investigated at the example of noble metal nanoparticles such as Ag, Au, AgAu and AgPt.

In the framework of this thesis, the investigation of memristive devices was based on the concept of the field driven migration of mobile metal cations through a dielectric matrix. A memristive device was developed, in which nanoparticles act as the source of mobile silver cations and are embedded in a dielectric SiO_2 matrix with nanometer thickness. The incorporation of nanoparticles yields several advantages compared to conventional memristive devices with planar electrodes: The inter-particle distances can be tailored and the local field enhancement in between the nanoparticles results in predefined pathways for memristive switching. By this approach, the common necessity of an electroforming step can be potentially avoided. The transition towards alloy nanoparticles of the systems AgAu or AgPt offers further advantages: On the one hand, the noble Au- or Pt- component may act as a stable anchor in the dielectric matrix. On the other hand, the amount of mobile species can be controlled deliberately by using alloy nanoparticles with a tailored composition. For this purpose, the gas phase synthesis of nanoparticles via magnetron sputtering was extended by a novel segmented target geometry for the deposition of alloy nanoparticles with well-defined diameter (about 10 nm) and adjustable composition.

Nanoparticle-based memristive devices were characterised regarding their memristive switching properties. Applying conductive atomic force microscopy on individual nanoparticles as well as two probe measurements with macroscopic tips on multiple stacks of nanoparticles revealed binary diffusive switching (also known as threshold switching) characteristics. Reproducible memristive switching with well-defined high- and low-resistance states was observed for multiple switching cycles. The choice of the nanoparticle composition as well as the separation by the dielectric matrix allows for tailoring of the resistance states. The statistical evaluation of the voltages associated with the set and reset process revealed a clear operational window, which allows stable switching between the two individual resistance states.

The fundamental investigations concerning the general concept of memsensors as well as the experimental studies on sensors and memristive devices as potential memsensor building blocks accentuate the high application potential of memsensors in the context of closing the gap between signal detection and processing. Therefore, memsensors constitute a highly interesting approach to be included in the development of biologically motivated, efficient computing architectures.

Table of Contents

1. Introduction

As we are writing the year 2019, in modern information society the usage of computation-based technologies is ubiquitous. Conventional silicon-based architectures have reached an unprecedented complexity, mainly driven by the miniaturization of transistors as their fundamental building units. Modern computing units excel at a high availability at low costs, a high clock speed and a high computing power, especially when it comes to sequential mathematical operations. Despite their steady improvements, the general underlying concept of contemporary computing architectures still relies on transistors arranged in a typical von-Neumann architecture, i.e. with a distinct separation of processing and memory functionalities. This is in strong contrast to the biological approach on computing: Neuronal networks such as the neuron assembly the reader is using right now are characterised by running at low power and at low clock speeds. The neurons as fundamental building blocks are arranged in three dimensions with a complex network of highly parallel synapses. In such networks, memory and computing are not separated. These neuronal networks are well suited for complex tasks such as pattern separation and completion at outstanding energy efficiency. Contemporary algorithms like deep learning networks adopt certain aspects of biological neural networks onto the platform of conventional silicon-based processing units, which allows for trainable networks to perform similar tasks. However, as the underlying hardware realization is still relying on conventional von-Neumann architectures, the energy efficiency is nowhere close to that of highly parallel and interconnected neuronal networks. Considering the inevitable energy consumption alongside the growing demand on computing power, the necessity of developing new, more efficient computational concepts becomes obvious. In this context, learning from biological concepts, optimised by millennia of evolution, attracts a high research interest.

In the past decade, since the postulation of the experimental realization of a memristor by Strukov et al. in 2008, memristive devices with their key features pinched IV hysteresis and reconfigurable resistance state (as depicted in Figure 1) attracted a high research interest for their potential application as emerging memory technology or to enable novel computing paradigms.[1–4] A broad variety of memristive devices (typically fabricated as metal-insulator-metal structures) relying on various memristive switching mechanisms has been reported since.[3,5,6] Among the multitude of concepts for reconfigurable memristive switching, a special interest lies on devices based on field-driven migration of mobile charge carriers, such as oxygen vacancies or metal cations. In the latter case, the oxidation, migration and reduction of the metallic species leads to the formation of metallic filaments, bridging the electrodes and significantly reducing the device's resistivity. At reverse polarity the filament dissolution is typically attributed to Joule heating and electromigration. In addition to the use of planar electrodes, recently nanostructured electrodes and nanoparticle assemblies have attracted high research interest in the context of memristive switching.[7–11]

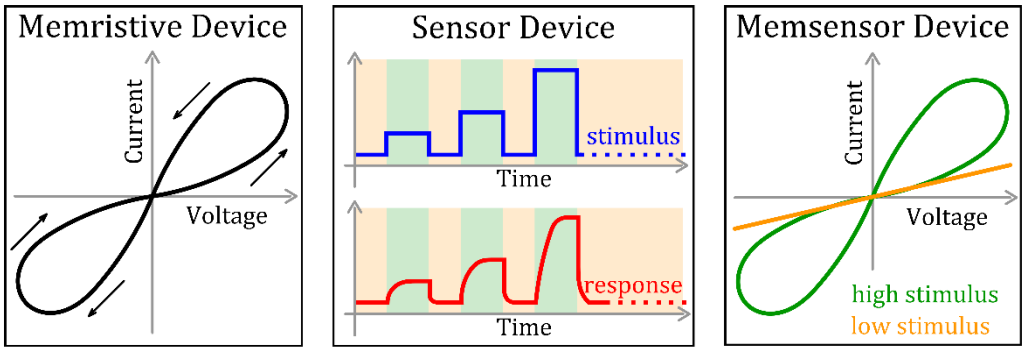

Figure 1: The electrical characteristics of idealised devices: A memristive device exhibits a pinched hysteresis loop and its resistance can be switched between different resistance states. A sensor device responds in a certain measurable quantity (e.g. resistance) to an applied stimulus (e.g. light). The response and recovery typically involve time constants resulting in a delay. A memsensor device unifies properties of a memristive device and a sensor device. As such, the memsensor device can exhibit a stimulus dependent memristive switching.

The unique electronic properties of memristive devices inspire applications that go beyond conventional electronics, such as using memristive devices as programmable interconnects, to realise logics for in array computing or in neuromorphic engineering. In this context, a broad variety of neural and synaptic properties has already been realised on the basis of memristive elements, including spike time dependent plasticity and spike frequency adaptation as well as coupling of oscillators by memristive junctions.[12–15] In order to make use of the scaling potential, two-terminal memristive devices are commonly arranged as crossbar arrays. Using arrays of memristive devices, complex tasks such as learning and recognition of artificial inputs, e.g. the MNIST database of handwritten digits, or in memory computing have already been successfully realised.[16,17]

For learning to be possible, any neural network, irrespective of its biological or artificial origin, needs to be subjected to a meaningful input. In the biological context, this can either be electrical inputs (signal transmission from neuron to neuron) or environmental signals, that are being converted (such as visual signals converted by our visual system). The latter case relates to the general concept of a sensor, which exhibits a certain measurable property (response) that is altered upon application of an external stimulus (as depicted in Figure 1). For a technical realization, a vast amount of materials and methods to design sensor structures for the detection of different stimuli is known, including semiconducting metal oxide thin film structures, whose resistance is altered upon applying adequate photons (UV light) or gas molecules.[18,19]

One key aspect concerning the efficiency of biological neural networks is the close connection between the detection of environmental signals and the data processing. In this light, the junction between sensing and memristive devices recently attracted increasing research interest. The reports on the realization of memsensors, combining memristive switching and sensing properties, range from a light sensitive Si/Al_2O_3 stack[20] over single Si-nanowires with bio-sensing capabilities[21] and mechanically stimulated CuO-nanowires[22] towards crossbar memristive devices with nanostructured top electrodes for oxygen sensing[23]. Using photons as stimulus, optically modulated memristive

switching[24] as well as an optical synapse[25] have been realised. On the background of the novelty of memsensors and the vast choice of sensitive and memristive devices, a consistent theoretical framework on this matter is not fully developed yet.

This work evolves around the concept of memsensors, which unifies the characteristic features of memristive devices and sensor devices. In the following sections, memsensors are explored by modelling simple memsensor circuits and developing and characterizing different memristive and sensitive devices. In this context, the motivation behind this work can be summarised by the following key questions:

How can memristive switching and sensing be combined in memsensors in order to achieve emerging properties?

How do these properties relate to properties observed in biological neuron assemblies?

Which memristive and sensitive devices are suitable as building blocks for the design of memsensor devices?

In order to attain a thorough treatment of memsensors as well as sensors and memristive devices as the respective components of a memsensor, this thesis is structured as follows:

Section 4.1 is devoted to the development, fabrication and characterization of a nanoparticle-based memristive device with diffusive memristive switching characteristics. In this device the reversible change in the resistance state is attributed to the migration of silver cations in an electrical field. The novelty of the nanoparticle-based memristive devices compared to similar electrochemical metallization devices is to be found in the application of noble metal alloy nanoparticles as well-defined source of the mobile silver species. Applying sequential deposition, alloy nanoparticles relying on the components AgAu or AgPt are embedded into a dielectric SiO_2 matrix. In this context, a novel, facile approach for the deposition of alloy nanoparticles from gas phase synthesis was developed, which utilises a segmented bimetallic target with concentrically embedded wires to fabricate alloy nanoparticles with tailorable composition and narrow size distribution. A detailed characterisation of the memristive switching properties on the level of individual nanoparticles as well as for larger multistack assemblies revealed diffusive memristive switching with a distinct separation of the switching events.

In section 4.2, semiconducting metal oxide thin films are studied in the context of sensing of UV-photons and gas molecules. Two routes are explored in order to tailor the sensing properties: On the one hand the impact of attaching noble metal nanoparticles to the thin film sensor surface is examined. In this context, a drastic increase in gas response at the example of ZnO thin films is observed, which is related to a change in electron depletion layer in the surrounding of a nanoparticle. On the other hand, reactive DC magnetron sputtering was studied with respect to the deposition of CuO and TiO_2 thin films with controllable morphologies. A special attention is paid to the role of the availability of oxygen during the deposition process and a deliberate variation of the oxygen flow allowed for the preparation of nanocolumnar CuO thin films and TiO_2 thin films with pronounced

nanocrack morphology. Ultimately, both approaches are combined at the example of nanocolumnar, nanoparticle-decorated CuO thin film sensors. In the latter case, the presence of AgAu nanoparticles results in a change in selectivity towards certain volatile organic compounds.

Finally, the topic of memsensors as the junction of memristive devices and sensors is covered in section 4.3. In a numerical simulation, memsensor circuits relying on individual sensitive and memristive components are investigated with respect to their electrical response towards the application and withdrawal of stimuli. On the one hand, the memristive and sensitive devices prepared in this work are modelled and incorporated into the numerical simulation. On the other hand, the simulation is extended to an abstract model of idealised memristive devices with analog, multilevel switching behaviour. In the framework of these numerical simulations, emerging properties such as stimulus dependent hysteresis (as depicted in Figure 1), suppression of response to subthreshold signals and amplitude adaptation to subsequent stimulus pulses are discussed in terms of the applied memsensor models. In particular, these features show striking similarities to certain properties of biological neuron assemblies such as spike-frequency adaptation, which renders memsensors a very interesting research topic in the field of neuromorphic engineering. As an outlook, a rational design for two-terminal memsensor devices, involving a thin film stack and lateral contacts, is motivated and the applicability of the nanoparticle-based memristive devices and semiconducting metal oxide sensors, which have been investigated in this work, is discussed.

2. Theoretical Background

Research on the matter of memsensors involves insights on memristive switching and sensing as well as the relation to neuromorphic engineering. Due to the highly interdisciplinary character of this topic, reaching into the fields of material science, biology and electrical engineering, this section serves to give a brief introduction into the theoretical background on electronic devices with memristive and sensitive properties as well as their potential applications and common fabrication methods.

For this purpose, in section 2.1 the underlying principles of electrical conduction with respect to specific materials (e.g. semiconductors), across interfaces (e.g. metal-semiconductor interfaces) and in heterostructures (e.g. metal-insulator-metal structures) are summarised.

Section 2.2 covers the topic of memristive switching. Starting with a thorough discussion of the term "memristive switching", the most common memristive device classes are summarised based on their switching characteristics or the underlying switching mechanism (cf. section 2.2.1). Within the framework of this thesis, especially metal cation based memristive devices were investigated. Accordingly, section 2.2.2 specifically focusses on the detailed description of memristive switching in metal cation-based devices. Furthermore, in section 2.2.3, a general overview on modelling of memristive devices is given, which closes the link to the memsensor model that was elaborated in the framework of this thesis. Finally, the application of memristive devices in conventional electronics and beyond is motivated in section 2.2.4. In particular, the necessity of selector devices in crossbar structures is discussed with respect to the potential application of nanoparticle-based memristive devices with diffusive characteristics.

A brief introduction into the field of neuromorphic engineering with a focus on the application potential of memristive devices and memsensor devices within this field is given in section 2.3.

Section 2.4 covers the topic of sensor devices with a special focus on metal oxide semiconductor nanostructures for sensing of photons and gas molecules, relating to the sensing devices presented in this thesis. Additionally, the enhancement of sensing properties by nanoparticle decoration and the junction between memristive switching and sensing in the context of memsensors are discussed.

Within the framework of this thesis, devices with memristive and sensitive functionalities are prepared using different thin film and nanostructure deposition methods. Accordingly, a comprehensive introduction into the main deposition methods (section 2.5) will be given and the particular focus lies on physical vapour deposition methods like magnetron sputtering for thin films and the gas aggregation source for nanoparticle deposition.

2.1 Electrical Conductivity in Solids

The electrical conductivity in solids strongly depends on the respective material and its band structure. The majority of the memristive devices, sensors and memsensors discussed in the context of this thesis rely on metal oxide thin films or nanostructures, which are contacted by metal contacts. Thus, these devices often exhibit a so-called metal-insulator-metal (MIM) or metal-semiconductor-metal (MSM) structure. Depending on the oxide material, the band gap corresponds either to an insulator (e.g. in case of SiO_2 or Al_2O_3) or a wide band gap semiconductor (TiO_2, ZnO). Essential for the application of a device as a sensor or memristive device is its capability to change its resistance state. While memristive devices are discussed in detail in section 2.2 and sensor devices are introduced in section 2.4, in this section the underlying concepts of electronic conduction in MIM or MSM heterostructures will be motivated. The fundamental concepts of the density of states, band structure and Fermi-Energy will not be discussed here. More details on that matter can be found in introductory text books on solid state physics, such as the book of H. Ibach and H. Lüth.[26]

Idealised band diagrams for a metal, a semiconductor and an insulator are depicted in Figure 2. The characteristic feature of a metal is the presence of unoccupied states in the conduction band, which allows for the possibility of electron transport and results in a low resistivity. Considering the vacuum energy level, the energy which is necessary to release an individual electron from the conduction band to the vacuum is given by the work function E_W. In case of a semiconductor at low temperatures, the valence band is fully occupied. As there are no free charge carriers available, the resistivity of a semiconductor in this state is high. The energy difference between the valence band (with E_V) and the conduction band (with E_C) is the band gap (with E_G). The occupation of the valence and conduction band is described by the Fermi distribution. Due to thermal excitation, electrons from the valence band can be ejected into the conduction band. As a consequence, an unoccupied state in the valence band remains, which is called hole. In case of an undoped semiconductor, the Fermi energy E_F (i.e. the energy for which the Fermi distribution has the value of 0.5) is centred between the conduction band and the valence band. Due to the presence of electrons in the conduction band at non-zero temperatures, the resistivity of a semiconductor decreases for increasing temperatures. The conductivity of semiconductors can also be tailored by doping. In a doped semiconductor, a small fraction of atoms from the host lattice is replaced by different atom species or (e.g. in case of metal oxide semiconductors) oxygen vacancies. These can either act as donors or acceptors, resulting in n-doping and p-doping respectively. In case of n-doping, the dopant introduces a state close to the conduction band. Thus, an electron is ejected (i.e. "donated") to the conduction band, while there remains a hole at the dopant state. Consequently, the Fermi energy of the doped semiconductor is in between the conduction band and the energy level of the dopant state. In case of p-doping, the dopant state is introduced close to the valence band and occupied by an electron from the valence band (i.e. it accepts an electron). In this case, the Fermi energy is centred between the valence band and the energy level of the donor state. The resistivity of a semiconductor at a given temperature can be tailored to a broad range upon the introduction of free charge carriers (electrons or holes) by doping. Materials with a very high band gap are typically

highly insulating and show a high resistivity even at elevated temperatures. Thus, such materials are termed insulators.

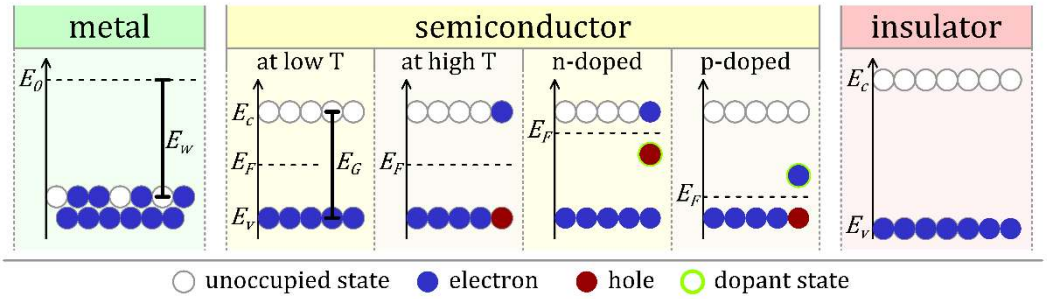

Figure 2: Idealised band diagrams illustrating the occupation of states in case of metals (left, green background), semiconductors (middle, yellow background) and insulators (right, red background).

2.1.1 Electrical Conductivity at Interfaces

In a MIM or MSM heterostructure, the interfaces towards the metal contacts strongly affect the overall resistance of the device. In general, two main types of contacts are distinguished: Ohmic contacts with a linear IV characteristics and nonlinear (rectifying) IV characteristics such as observed in Schottky contacts. The formation of Schottky barriers in metal-semiconductor contacts is a common observation. A detailed treatise of this matter is covered for example in the book "Electronic Thin Film Science" by K-N. Tu, J. W. Mayer and L. C. Feldmann.[27] The essential mechanism of Schottky barrier formation at a metal-semiconductor interface can be reasoned from the idealised band diagram as depicted in Figure 3 (a). In this example, a metal with work function E_W is brought in contact with a n-doped semiconductor with an electron affinity E_A. The electron affinity corresponds to the energy difference between the conduction band (at E_C) of the semiconductor and the vacuum level (at E_0). At the interface, the Fermi levels line up and an energy barrier E_B is formed, which corresponds to the difference between the work function of the metal and the electron affinity of the semiconductor.

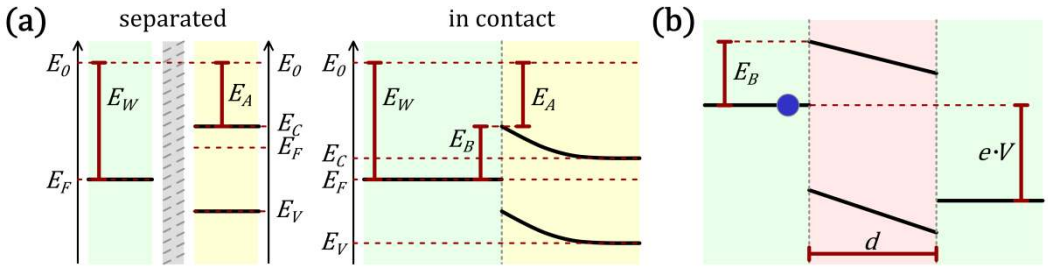

Figure 3: (a) Idealised band diagram for the formation of a Schottky barrier at a metal-semiconductor interface; (b) Idealised band diagram for a metal-insulator-metal (MIM) structure at an applied voltage *V*.

Applying a negative (or positive) potential to the semiconductor, the position of the conduction band is raised (or lowered). In the first case, the so-called forward bias, the barrier for electrons being transported from the semiconductor to the metal is decreased, allowing for a higher current. In the latter case, the so-called reverse bias, the current of electrons from metal to semiconductor is determined by the energy barrier E_B. The current

density j can be described by Eq. 2.1, with A being the Richardson's constant, k_B being the Boltzmann constant and T being the temperature: [27]

$$j = A \cdot T^2 \cdot \exp\left(\frac{-E_B}{k_B T}\right) \cdot \left(\exp\left(\frac{e \cdot V}{k_B T}\right) - 1\right) \tag{2.1}$$

In section 2.2.1, the most common types of memristive devices are introduced. Commonly, most of these devices resemble a thin film heterostructure with metal contacts to both interfaces of semiconductor or insulator layer (with thickness d) as depicted in Figure 3 (b). Accordingly, the choice of adequate contact materials (e.g. metals with a suitable work function) is very important: For example, in case at both interfaces Schottky barriers with high energy barriers are present, independent of the polarity of the applied voltage one interface will be under reverse bias condition, which results in a very high device resistance. However, the contact material can impact the characteristics of a memristive device even beyond the modulation of the resistivity upon formation of Schottky barriers. The impact of metal contacts on electrochemical reactions in memristive devices will be discussed in section 2.2.2.

2.1.2 Electrical Conductivity in MIM or MSM Devices

The resistance of a MIM or MSM device is determined on the one hand by the respective interfaces to the metal contacts and on the other and by the conductivity through the insulating or semiconducting layer itself. The most relevant conduction mechanisms in the framework of memristive devices are thoroughly discussed in the work of E. Lim and R. Ismail.[28] In the following section, these mechanisms and the dependence of the current density related to these mechanisms are introduced shortly. The respective equations (Eq.2.2 to Eq.2.11) are reduced to show the dependence of the current density j on the applied voltage V as well the temperature T. Further components in the equations are summarised for a better readability as constants C or $\tilde{C}$ individually for each equation (i.e. C in Eq.2.2 does not match C in Eq.2.3 etc.).

The idealised band diagrams, indicating the transport of a single electron (blue dot) are depicted for selected conductivity mechanisms in Figure 4.

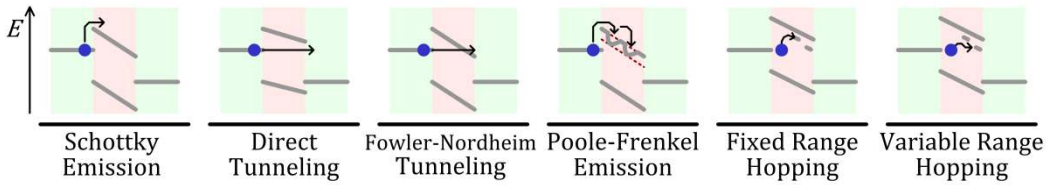

Figure 4: Schematic depiction of typical conductivity mechanisms in memristive devices, including Schottky Emission, Direct Tunneling, Fowler-Nordheim Tunneling, Poole-Frenkel-Emission, Fixed Range Hopping and Variable Range Hopping.[28]

Schottky Emission

In case of Schottky emission, the conductivity is determined by thermally activated electrons, which are injected over the energy barrier into the conduction band. The corresponding current density dependence is given in Eq.2.2: [28]

$$j \propto T^2 \cdot \exp\left(C \cdot \frac{\sqrt{V}}{T} - \tilde{C} \right) \tag{2.2}$$

Tunnelling

For thin insulating layers with a thickness in the low nanometer regime, tunnelling may occur as an additional conductivity mechanism. In this context, tunnelling is a consequence of a finite barrier height, which leads to a non-zero probability density for electrons on both sides of the insulator. In case of direct tunnelling, the electron overcomes the whole barrier (with thickness *d* corresponding to the thickness of the insulating layer). Accordingly, as described by Eq.2.3, the current density due to direct tunnelling is neither a function of the applied voltage nor the temperature.[28] In contrast, in Fowler-Nordheim tunnelling, an applied voltage of appropriate polarity results in a band bending, which effectively lowers the barrier width and allows electrons to pass through the barrier into the conduction band. The corresponding current density as described by Eq.2.4 is a function of the applied voltage, but not the temperature.[28]

$$j \propto \exp\left(-C \cdot d\right) \tag{2.3}$$

$$j \propto V^2 \cdot \exp\left(-\frac{C}{V} \right) \tag{2.4}$$

Poole-Frenkel Emission

While Schottky emission and tunnelling mainly considered the interfacial barrier, in case of Poole-Frenkel emission and electron hopping, potential wells and trapping states within the bulk of the insulating layer are to be considered respectively. Such trapping states typically are located below the conduction band. The origin of such traps in metal oxide thin films is commonly attributed to the presence of defects such as oxygen vacancies.

For Poole-Frenkel emission, the conductivity is a result of electrons being thermally excited from individual potential wells and successively being transported through the insulating layer in the presence of an applied potential. The corresponding current density is given by Eq.2.5: [28]

$$j \propto V \cdot \exp\left(C \cdot \frac{\sqrt{V}}{T} - \tilde{C} \right) \tag{2.5}$$

Electron Hopping

Electron hopping is typically distinguished between fixed range hopping (also termed nearest neighbour hopping) and variable range hopping. The respective expressions for the current densities are given in Eq.2.6 and Eq.2.7.[28]

In electron hopping, electrons occupy trap states within the bulk of the insulating layer and are transported via subsequent tunnelling events from one trap state to another. The main difference between fixed range and variable range hopping is the position of the trapping states, to which the electron migrates (cf. Figure 4). In case of fixed range hopping, the electron hops to the neighbouring trap state, although this state may exhibit a higher energy. In order to occupy a higher energy state, the interaction of the respective electron with a phonon is necessary, which essentially adds a temperature dependence to the equation for the current density. In case of variable range hopping, the electron hops into a trap state, which exhibits a lower energy difference (resulting in a less significant temperature dependence), although this might involve the necessity of overcoming a greater distance (which relates according to Eq.2.3 for direct tunnelling in a lower tunnelling current).

$$j \propto V \cdot \exp\left(\frac{-C}{T}\right) \tag{2.6}$$

$$j \propto V \cdot \exp\left(\frac{-C}{T}\right)^{\frac{1}{4}} \tag{2.7}$$

Ohmic conduction

Despite the considerable band gap, thermal excitation at non-zero temperatures may lead to the presence of electrons in the conduction band. The current density related to Ohmic conduction is given by Eq.2.8, where the constant C essentially describes the band gap.[28]

$$j \propto V \cdot T^{\frac{3}{2}} \cdot \exp\left(\frac{-C}{T}\right) \tag{2.8}$$

Space-Charge-Limited conduction

The description of space-charge-limited conduction is based on the assumption of charge carriers being injected from the metal contacts into the dielectric layer upon the application of a strong electrical field across the dielectric layer. The injected charge carriers are treated as a space-charge (i.e. the charge is distributed continuously within a certain spatial region). In the picture of SCLC, in case the transit time of the respective charge carrier is smaller than the characteristic relaxation time, the subsequent drift of charge carriers towards the opposite electrode can efficiently result in a current contribution.[29] The current density follows the square of the voltage (Mott-Guerney law):[28]

$$j \propto V^2 \tag{2.9}$$

Ionic conduction

The conductivity mechanisms so far focussed on the transport of electrons as charge carriers. However, in memristive devices the transport of further charge carriers, such as metal cations or oxygen vacancies, is a common phenomenon. Accordingly, in case the insulating layer exhibits a sufficiently high ion conductivity, also the contribution of the ion current has to be considered. In case of low (high) electrical fields, the current density approximately follows the relation described in Eq.2.10 (Eq.2.11): [28]

$$(2.10) \qquad j \propto \frac{V}{T} \cdot \exp\left(\frac{-C}{T}\right)$$

$$(2.11) \qquad j \propto \exp\left(\frac{V-C}{T}\right)$$

In a real device, a variety of the conduction mechanisms mentioned in this section can be present simultaneously and a particular mechanism can become dominant at certain temperature or voltage regimes. In the framework of this thesis, a memristive device based on metal cation migration in a metal oxide matrix was developed and sensor devices based on different metal oxide materials were investigated. For a rational design of any electronic device such as the devices prepared in this thesis, the knowledge of the respective conductivity mechanisms present in the specific device is a necessity. The dependencies of the current density on temperature and applied voltage (cf. Eq.2.2 – Eq.2.11) related to the respective conduction mechanism can be used to identify the dominating conductivity mechanism in a device. For this purpose, C. Acha proposed a power exponent ($d\ln(j)/d\ln(V)$) vs. $V^{½}$ plot and applied it to determine the conductivity mechanisms in memristive devices.[30] In principle, additional insights on the switching mechanism can be obtained using a similar $d\ln(j)/d\ln(T)$ vs. T plot. However, experimentally the variation of the applied voltage is easier than the variation of the temperature. The idealised graphs for the temperature and voltage dependencies are depicted in Figure 5. This scheme for evaluating memristive switching phenomena regarding the dominant conductivity mechanisms is also applied to the nanoparticle-based memristive devices in section 4.1.4.

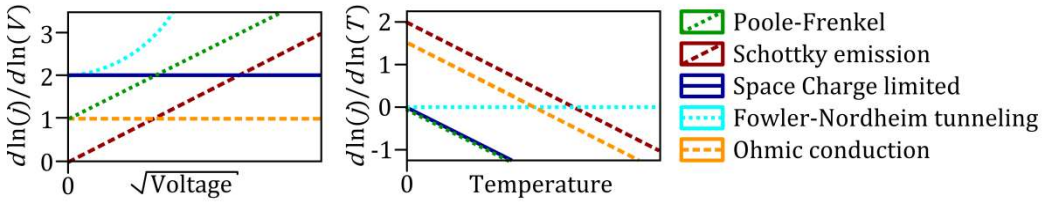

Figure 5: Schematic depiction the voltage dependency (left) and the temperature dependency (right) of the power exponent for Poole-Frenkel emission, Schottky emission, Space-Charge-limited conduction, Fowler-Nordheim tunnelling and Ohmic conduction.[30]

2.1.3 Additional Considerations for Thin Film Devices

In most cases, the active material in a memristive device or a sensor device is used as a thin film or nanostructure. The conductivity of thin films and nanostructures may deviate strongly from the behaviour observed in the bulk counterparts of the identical material. The simple band structure considerations presented for metals, semiconductors and insulators typical rely on the assumption of periodic boundary conditions, which relates to infinite size of material. For bulk materials this approximation is at hand, the unit cell of the material is orders of magnitude smaller than the dimensions of the conductor. However, in thin films the dimension of the material approaches in at least one dimension the size of the unit cell. At the surface, the bonding states are different from those in the bulk. Another layer of complexity is added by the fact that some metal oxides tend to form oxygen vacancies, e.g. in contact to air or reactive metals. For example, in TiO_2 the impact of oxygen vacancies is widely studied and results in a n-doping of the TiO_2 and hence strongly impacts its resistance.[31] Such deviations in electronic behaviour in nanoscale materials will not be discussed in detail here. However, the importance of oxygen vacancies in metal oxide thin films will be discussed in section 2.2.1 in relation to memristive switching devices and surface effects will be discussed in section 2.4 with respect to sensing.

2.2 Memristive Switching

This section gives a comprehensive introduction to the broad field of memristive switching. First, the term memristive switching as used within the context of this thesis will be thoroughly defined based on a short overview on memristive switching milestones. Section 2.2.1 serves as a comprehensive introduction on the variety of classes of memristive devices with an emphasis on the underlying switching mechanisms and IV characteristics. In section 2.2.2 the class of cation movement based memristive devices (which includes the nanoparticle-based devices investigated within this thesis) is thoroughly discussed. The main concepts of memristive device modelling are summarised in section 2.2.3. Finally, a short introduction into application scenarios for memristive devices is given in section 2.2.4.

In 1971 Leon O. Chua introduced the "Memristor" as the fourth basic two-terminal circuit element[32]. Based on symmetry arguments and the classical Maxwell equations, Chua predicted the memristor as a passive circuit element linking magnetic flux φ and electrical charge q. Much like the three other passive basic circuit elements, namely a resistor (with resistance R), an inductor (with inductance L) and a capacitor (with capacity C), the memristor exhibits an intrinsic property. This is the memristance M, which is defined as: [32]

$$M(q) = \frac{\partial \varphi(q)}{\partial q} \tag{2.12}$$

In this early work, apart from theoretical considerations also circuit realizations with active elements were presented. A physical passive memristor device however was not described at that time. Five years later, in 1976, Chua generalised the initial theory from the ideal charge-flux memristor to the broader class of memristive devices, exhibiting the so-called pinched IV hysteresis as a key characteristic.[33]

Almost four decades later, in 2008, Strukov et al. linked bipolar resistive switching in an oxygen deficient TiO_2 thin film device to the concept of a memristor in their paper "The missing memristor found".[2] In their device, changes in the resistance are attributed to oxygen vacancy drift in an applied electrical field. However, comparable reports on devices with binary or multiple resistivity states can be found earlier.[34–38] The real novelty of this work was the link drawn towards the memristor and the modelling of the memristance in a current-based model closely related to Chua's generalised model on memristive devices.[33]

The proposal of the discovery of the missing memristor spiked a scientific controversy, which is mainly driven by the fact that in the model by Strukov and the TiO_2 device representation the link between magnetic flux φ and electrical charge q is unapparent.[39,40] However, the strong attention on this discourse stimulated further research in the field of resistance switching phenomena and coined the term "memristor" in the research on resistive switching.

Over the past years, the research on memristive devices was motivated by broad application promises: On the one hand memristive devices are envisioned to complement FLASH and DRAM as novel storage media.[3,38,40] On the other hand there are many concepts for

applications in advanced computation, such as brain-inspired (neuromorphic) beyond von-Neumann computing.[41–44] Accordingly, research on memristive devices became an interdisciplinary field with contributions from electrical engineering, material science, physics and chemistry as well as close links to biology and neuroscience. This heterogeneity also reflects in the occurrence of synonyms: memristive switching, resistive switching or resistive random access memory (RRAM). Within the framework of this thesis the term memristive switching will be used to describe any switching between two or more resistance states and every device that shows memristive switching is described as memristive device.

2.2.1 Categorization of Memristive Switching

In 2008 Burr et al. wrote in their review on emerging technologies for non-volatile memory (NVM): [38]

"Over the past 50 years, a large number of materials have been explored for use as a resistive NVM. Although most of these materials can be switched between two distinct resistance states using suitable voltages, the switching mechanism is believed to vary from material to material and is poorly understood."

With the increased interest in memristive devices in the following years, also the number of reports on various devices with memristive switching behaviour and the underlying physics of their respective switching mechanisms increased drastically. Especially the underlying switching mechanisms have been investigated in close detail for many devices relying on different materials and material combinations. This diverse landscape of memristive devices is typically categorised by two main ways:

- Categorization by the switching characteristics in their IV hysteresis curve
- Categorization by the underlying switching mechanism

Categorization by the switching characteristics in their IV hysteresis curve

First, the classification of memristive switching based on the generalised shape of the IV curve is discussed. The memristive device in its pristine state exhibits typically a high resistance, i.e. it is in its high resistance state (HRS). By applying a certain voltage, the resistance of the device decreases and the device is set to its low resistance state (LRS). The corresponding voltage is commonly called set voltage (SET). Depending on the type of switching, the device exhibits one low resistance state (binary switching) or a multitude of intermediate resistance states (IRS, analog switching). In case the device shows a limited number of low resistance states, it is also termed quasi-analog or multilevel switching. For analog and quasi-analog devices, each IRS corresponds to an individual SET voltage, i.e. for higher applied SET voltages the device switches to a lower resistance state. After the device is SET, the resistance state of the memristive device is conserved (with a finite retention time) until the device is subjected to a certain reset voltage (RESET). At this voltage, the device switches back into its HRS. Idealised IV curves with the main characteristics for these three switching scenarios are shown in Figure 6.

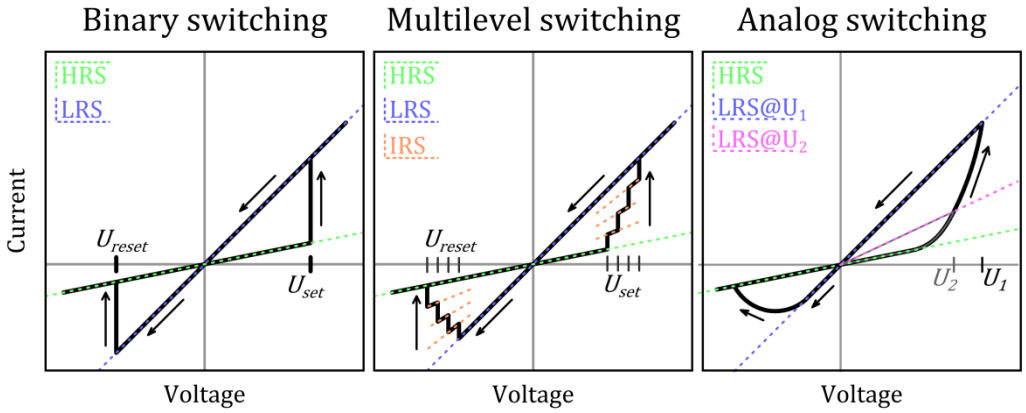

Figure 6: Idealised IV hysteresis loops for memristive devices with two distinct resistance states (binary, left), a limited number of resistance states (multilevel, middle) and a multitude of resistance states (analog, right).

The three idealised IV hysteresis loops depicted in Figure 6 are examples of bipolar memristive switching. In bipolar memristive devices the SET and RESET occur at opposite polarities. Thus, the device is initially in its HRS, the voltage is ramped up and at a given SET voltage, the device switches to the LRS. Subsequently, the voltage is ramped down and the LRS is conserved upon crossing zero voltage. At a certain RESET voltage at negative polarity, the device switches back to its HRS. Complementary to this bipolar switching behaviour, also unipolar and diffusive switching is commonly reported. Idealised IV hysteresis loops for bipolar, unipolar and diffusive switching are shown in Figure 7.

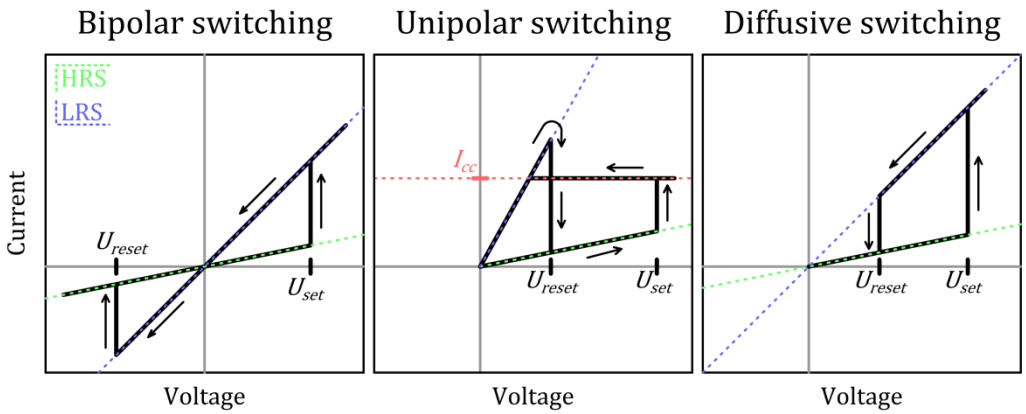

Figure 7: Idealised IV hysteresis loops for memristive devices with bipolar (left), unipolar (middle) and diffusive (right) switching behaviour.

In contrast to bipolar switching, in unipolar switching, the RESET and SET processes occur at the same polarity. The device initially starts in its HRS. The voltage is ramped up to the SET voltage and the device switches to its LRS. The current is limited to a compliance current in order to secure the device from hard breakdown. Subsequently, the voltage is ramped down to zero voltage and the LRS is conserved. In the following ramping step, the current compliance is no longer present. As the voltage reaches the RESET voltage, the device switches back to its initial HRS.

In diffusive memristive switching, similar to unipolar switching, the SET and RESET voltage also occur at the same polarity. The device is initially in its HRS and switches abruptly to its LRS upon ramping of the voltage to the SET voltage. When the voltage is ramped down, the device switches back to its HRS as soon as the RESET voltage is reached. Accordingly, for a diffusive memristive device, the resistance state is not conserved for a full cycle in the hysteresis loop. The device always exhibits its HRS at zero voltage. Accordingly, a diffusive memristive device in itself is not suitable for operation as a long-term low power memory device, because the conservation of the resistance state is only possible by constantly applying a voltage.

In order to reach a stable operation regime, where the device can be repeatedly be switched between LRS and HRS, some devices have to be conditioned by a so-called electro-forming step. This step typically involves the application of a higher voltage than for the later SET step. Commonly, a current compliance limits the current, so that a hard breakdown of the device is avoided. For application purposes, memristive devices that don't need any electroforming step after fabrication (i.e. forming-free memristive devices) are typically preferred, because high voltages and the necessity of limiting the current complicate circuit design.

Categorization by the underlying switching mechanism

Apart from the categorization based on the shape and characteristic features of the IV curve, memristive devices are also commonly described based on the underlying physical phenomena that lead to the change in resistivity. This section will give an overview on the most common memristive device classes that bear a certain relevance for the work presented in this thesis. In this context, the following three mechanisms for memristive switching will be discussed:

- Electrochemical metallization (ECM) based memristive switching
- Valence change mechanism (VCM) based memristive switching
- Interface based memristive switching

These three mechanisms for memristive switching are schematically illustrated in Figure 8 by depicting idealised cross sections of typical devices.

Due to the broad diversity of memristive devices that have been reported, a detailed discussion of all devices and all underlying physical mechanisms would go beyond the scope of this section. For detailed information on other memristive switching phenomena, ranging from an all-carbon-memristive device[12] or a carbon-nanotube-array based switching[45] over the growing field of organic memristive devices[6,46,47] and phase change material based memristive switching (PCM)[5] to spin-torque transfer magnetic memories (STT-MRAM)[48,49], the reader is encouraged to look directly into the referenced literature.

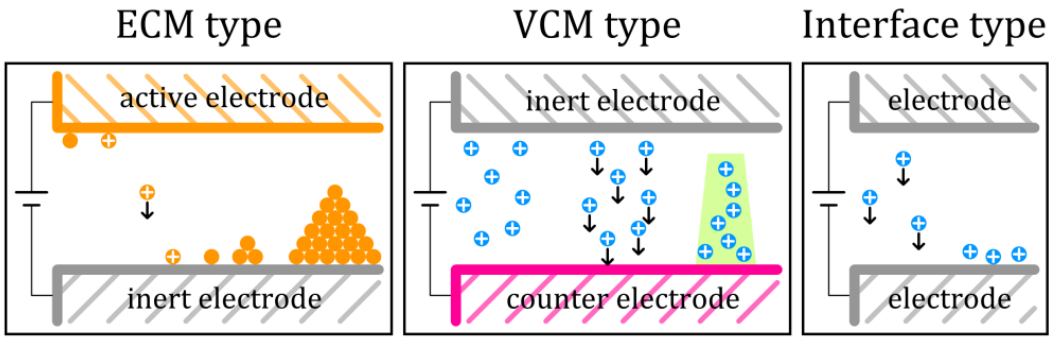

Figure 8: Idealised cross sections through typical ECM, VCM and Interface memristive switching devices. The electrodes are connected to a DC voltage source and the resulting charge carrier migration is indicated by black arrows.

Electrochemical metallization (ECM) based memristive switching

ECM based memristive switching relies on the oxidation, migration and reduction of metal atoms and ions respectively. A typical ECM memristive device is a metal-insulator-metal (MIM) structure, in which an insulating layer is sandwiched between an active and an inert electrode. In its pristine state, the insulating layer contains a negligible concentration of metal cations and the memristive device is in its HRS. As soon as the active electrode is put on a positive potential and the inert electrode is put on a negative potential, atoms from the active electrode can get ionised, which is an oxidation reaction. In Eq.2.13 this reaction is shown at the example of the oxidation of a silver atom.

$$\mathrm{Ag} \rightarrow \mathrm{Ag}^{+} + \mathrm{e}^{-} \tag{2.13}$$

The potential drop over the insulating layer results in an electrical field acting between both electrodes. Within this electrical field the positively charged metal cations experience a net transport towards the inert electrode. Subsequently, the mobile cations are reduced, which is shown at the example of a positively charged silver cation in Eq.2.14.

$$\mathrm{Ag}^{+} + \mathrm{e}^{-} \rightarrow \mathrm{Ag} \tag{2.14}$$

As this whole process of oxidation, transport and reduction occurs for a multitude of metal atoms, over the time a metallic filament evolves inside the insulating matrix. This process of filament formation is facilitated by the increase in electrical field at the position of protrusions in the insulating layer. As soon as the metallic filament is bridging the two electrodes, the resistance of the overall device drastically decreases and the device is SET to its LRS. In order to RESET the device to its HRS, typically the voltage polarity has to be reversed. Accordingly, such devices commonly show bipolar switching.

At a reverse polarity, the net transport of mobile metal cations would be directed towards the active electrode. In the LRS however, there is no considerable electrical field between the two electrodes because the metallic filament connects both electrodes (short circuit). Therefore, ECM memristive devices are also known under the term “conductive bridge random access memory” (CBRAM). It is commonly believed that the high current density

inside the metallic filament yields strong Joule heating, which in turn results in a dissolution of the filament tip.[42,50] However, recent results based on kinetic Monte-Carlo simulations have indicated that the effect of Joule heating alone may not be sufficient to explain the filament dissolution and other effect such as electromigration have to be considered.[51] As soon as the connection between both electrodes is initially dissolved, the strong electrical field results in a further dissolution of the filament. The device is RESET to its HRS. The pristine, flat interface between electrode and insulating layer is typically not fully restored. For that reason, commonly such simple ECM devices require an electroforming step at higher voltages, in which the initial filament is formed. In the following operation cycles, this initial filament is dissolved (LRS to HRS) and reformed (HRS to LRS). The corresponding SET voltage is considerably smaller than the electroforming voltage, because the preformed protrusion from the remaining filament considerably decreases the distance between the two electrodes and hence enhances the electrical field in the relevant area.

A broad variety of materials has been investigated in the context of ECM memristive devices. In Figure 9 reported materials for the successful implementation as insulating layer as well as the active electrode are summarised.

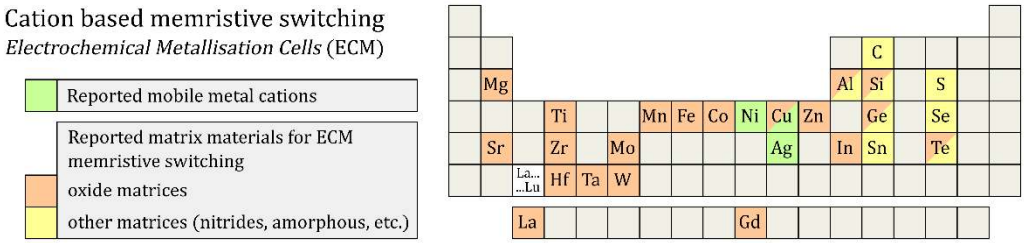

Figure 9: Overview over typical material combinations applied for metal cation based memristive switching. As mobile cations typically cations of the elements Ni, Cu or Ag are used (green colour). The matrices through which these cations are transported are most commonly oxide materials (orange colour), non-oxide matrices matrix materials are marked in yellow colour.[5,42]

For the use as an insulating matrix, a huge number of materials has been reported, which are mostly either oxides, nitrides (such as AlN and Si_3N_4), polymers or higher chalcogenides.[5,42,47] For low power operation the resistivity of the insulating layer is highly important, because it determines the HRS of the device. The choice for the active electrode is governed by two basic considerations: Firstly, the metal cations need to have a reasonable ion mobility inside the insulating matrix. Secondly, the oxidation and reduction reaction have to be possible at reasonable voltages. In addition, especially in contact with metal oxide insulating layer, the active electrode has to be stable against reactions with the insulating layer. As a consequence, copper (Cu), nickel (Ni) and silver (Ag), of which Ag is by far the most common, are typically used as active electrode materials.[5,42] A more detailed treatment of metal cation based memristive devices is given in chapter 2.2.2.

Valence change mechanism (VCM) based memristive switching

A typical VCM memristive device consists of an insulating layer, commonly a metal oxide layer, which is surrounded by two metal contacts. An idealised cross section through such a device is depicted in Figure 8. The switching mechanism in VCM memristive devices shows certain similarities to the ECM switching mechanism discussed above. Thus, also in most VCM memristive devices the underlying mechanism behind the resistivity change is the formation and dissolution of a conducting filament. In contrast to ECM devices however, the mobile charge carriers that are transported through the metal oxide matrix, are oxygen vacancies. These oxygen vacancies can either be present in the pristine device through deliberate processing or can be formed in an electrochemical reaction: [52,53]

$$(2.15) \quad O_O \rightarrow V_O^{\bullet\bullet} + 2e^- + \frac{1}{2}O_2$$

The release of oxygen due to this anodic oxidation reaction described in Eq.2.15 can even lead to the formation of gas bubbles underneath the respective electrode.[54] In case the electrode itself is reactive towards oxygen (e.g. a titanium (Ti) electrode in contact with a TiO_2 insulating layer), the formation of oxygen vacancies can also involve the electrode material:

$$(2.16) \quad Ti + 2O_O \rightarrow 2V_O^{\bullet\bullet} + 4e^- + TiO_2$$

Once the oxygen vacancies reach the opposite electrode, a cathodic reduction of the oxygen vacancies, as described by Eq.2.17, is possible under the prerequisite of available oxygen gas:

$$(2.17) \quad V_O^{\bullet\bullet} + 2e^- + \frac{1}{2}O_2 \rightarrow O_O$$

The oxygen vacancies are mobile within the insulating layer and migrate in the electrical field between the electrodes. The presence of oxygen vacancies acts as local doping by adding additional states in the band structure of the metal oxide. Accordingly, the resistance in the regions with high oxygen vacancy concentration is significantly reduced. Much like in case of ECM switching, also in VCM switching a filament with low resistivity is formed. As soon as this filament bridges both electrodes, the device switches from its HRS to LRS. As already described for ECM devices, also in VCM devices the partial dissolution of the filament (RESET) is assumed to be aided by Joule heating. Furthermore, electroforming is commonly necessary to form the initial filament.[53]

Typical model systems for VCM memristive devices are metal oxide thin films such as TiO2 with inert noble metal electrodes or in combination with an ohmic electrode (e.g. in the configuration Pt-TiO_2-Pt or Pt-TiO_2-Ti) or perovskite materials such as $SrTiO_3$.[53] As summarised in Figure 10, a huge variety of oxide materials has been reported as VCM memristive device.

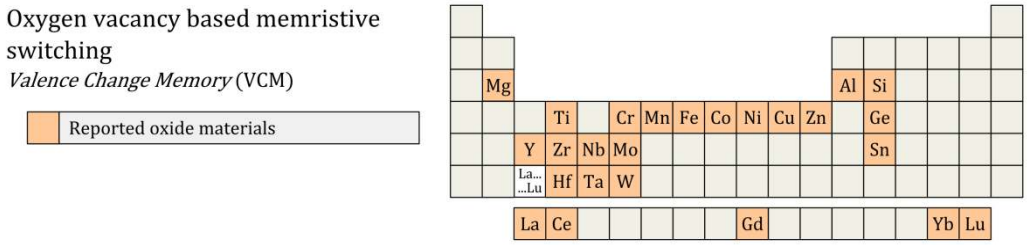

Figure 10: Overview over oxide materials typically used for oxygen vacancy migration based VCM memristive devices.[3,41,52,53]

Interface type memristive switching

The majority of ECM and VCM memristive devices rely typically on the formation and dissolution of a conducting filament, which leads to a binary or multilevel switching of the resistance over many orders of magnitude. A promising approach to avoid the necessity of electroforming and expand the number of resistance states to analog switching is found in interface-based memristive switching. These memristive devices are essentially MIM structures with two electrodes and an insulating layer in between, as illustrated in Figure 8. The nanoscopic dimension of the insulating layer suppresses the formation of conductive filaments as active current paths. The switching of the resistance states in such devices is based on the migration of mobile charge carriers towards the interface between an electrode and the insulating layer as well as trap states at this interface. Typically, the electrode materials are chosen such, that one electrode forms a Schottky barrier to the insulating layer while the other electrode forms an ohmic contact. The height of the Schottky barrier depends on the local stoichiometry of the oxide thin film at the interface. The gradual migration of oxygen vacancies (or oxygen ions[55]) in the electrical field across the thin insulating layer results in a high number of possible resistance states and consequently leads to a memristive device with analog switching behaviour and without the necessity of electroforming. One example of such devices is the double barrier memristive device, which relies on a stack of Au-Nb_xO_y-Al_2O_3-Al layers.[55–57]

Common to all three discussed classes of memristive switching devices is the importance of choosing appropriate electrode materials. The most commonly used electrode materials for memristive devices are summarised in Figure 11. For ECM memristive devices, Ag and Cu (and occasionally Ni) are reportedly applied as active electrodes. The high chemical stability makes noble metals such as Au or Pt common choices as inert electrodes. In addition, their high work function typically allows realizing Schottky barriers in contact with most semiconducting metal oxides, which is used for interface type memristive devices. Apart from metallic electrodes, also further electrode materials like the transparent indium tin oxide (ITO), the CMOS compatible titanium nitride (TiN) or carbon-based electrodes (CNTs, graphite) are reported. The influence of different electrode materials on the memristive switching behaviour in ECM devices will be discussed separately in section 2.2.2.

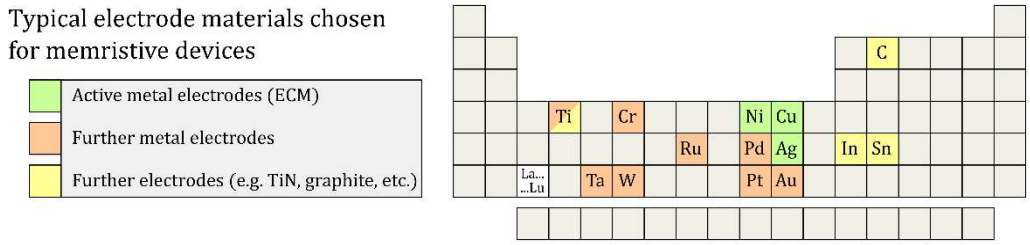

Figure 11: Overview over common electrode materials for the contacting of memristive devices. In addition to active metallic electrodes applied as depot for metal cations in ECM memristive devices (green colour), other metals (orange colour) and further electrode materials (yellow colour) such as TiN, graphite or ITO are commonly applied.[3,41,52,53,58]

Reports of vacancy movement and cation movement as competing mechanisms in the same device indicate that classification into VCM and ECM is not always exclusive and devices can exhibit certain characteristics of more than one device class.[59,60]

2.2.2 Cation-based Memristive Switching

In cation-based memristive devices, the transport of the metal cations and the resulting formation and dissolution of a conducting metallic filament is crucial for the change in electrical resistance. The switching kinetics in such redox based systems thus depend on the ion drift currents of the mobile metal cations. The ion drift current density j_i is described by the Mott-Gurney equation: [42,61,62]

$$(2.18) \qquad j_i \propto q \cdot a \cdot f \exp\left(-\frac{E_0}{k_B T}\right) \cdot \sinh\left(\frac{a \cdot q}{2 k_B T} E\right) \qquad \text{with } q = z \cdot e$$

The ion current depends on the charge q of the respective ions as well as the hopping distance a, the hopping frequency f and the hopping barrier E_0. The directed drift of ions is caused by an applied electrical field E. The charge of the respective ions is given in multiples z of the elementary charge e. In Eq.2.18, k_B denotes the Boltzmann-constant and T the temperature.

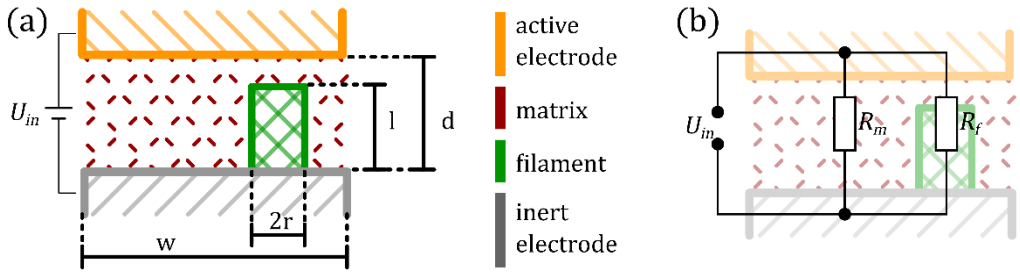

Figure 12: (a) Schematic cross section and (b) idealised equivalent circuit corresponding to a filament based memristive device.

Based on the Mott-Gurney relation for the ion current, a compact switching model for filamentary ECM memories was developed by Mahalanabis et al..[42,63,64] In this model, a single cylindrical filament with length l and radius r between two electrodes with the lateral

dimension *w* is assumed to be responsible for the memristive switching process. The cross section of such idealised ECM device is sketched in Figure 12 (a).

The filament growth in length and radial dimension can be expressed by Eq.2.19 and 2.20. As the filament length itself influences the electrical field strength *E* between the filament tip and the opposing electrode, Eq.2.19 is a differential equation with respect to *l*. The constant pre-factors C_l and C_r respectively serve as fitting parameters or can be derived from the physical model.[42]

$$\frac{\mathrm{d}l}{\mathrm{d}t} = C_l \cdot \exp\left(-\frac{E_0}{k_B T}\right) \sinh\left(\frac{aze}{2k_B T} E\right) \quad \text{with } E = \frac{U_{in}}{d-l} \tag{2.19}$$

The growth in lateral dimension does not impact the distance between the filament tip and the opposing electrode and hence does not alter the electrical field between them. The growth in radius is expressed by introducing an electrical field parameter for lateral growth β.[42]

$$\frac{\mathrm{d}r}{\mathrm{d}t} = C_r \cdot \exp\left(-\frac{E_0}{k_B T}\right) \sinh\left(\frac{aze\beta U_{in}}{k_B T}\right) \tag{2.20}$$

The assumption of a single cylindrical filament between the two electrodes results in two possible current paths: The current can go through the dielectric matrix (with R_m) and through the metallic filament (with R_f). The total resistance R_t of such filamentary metal cation based memristive devices is given by the parallel connection of these two resistances (Eq.2.21).[42] The corresponding equivalent circuit with its relation to the idealised cross section is shown in Figure 12 b.

$$R_t = \left(\frac{1}{R_f} + \frac{1}{R_m}\right)^{-1} = \left(\frac{\pi \cdot r^2}{\rho_f \cdot l} + \frac{w^2 - \pi \cdot r^2}{\rho_m \cdot d}\right)^{-1} \tag{2.21}$$

The applicability of this rather compact model was demonstrated by reproducing experimental data recorded for a memristive device with an active electrode made of silver and germanium selenide as matrix.[42]

However, the assumption of a strictly cylindrical shape of the metallic filament does not adequately represent the complexity of filament formation in metal-cation-based memristive devices. The shape of the filament and its growth direction strongly depends on the ion conductivity of the matrix and the rates of the oxidation and reduction reactions, which results in the filament either growing with its base at the active or inert electrode.[58] The following four cases have to be distinguished:

Case A: High ion mobility and high redox rates.

In this case, the high ion mobility leads to the metal ions being transported easily towards the inert electrode, where they are readily reduced. Accordingly, the metallic filament starts growing in a conical shape with its base at the inert electrode.

Case B: High ion mobility but low redox rates.

In this case, the metal cations are readily transported through the matrix due to the high ion mobility. The filament starts to grow with its base at the inert electrode, but has a rather branched shape because of the limited redox rates.

Case C: Low ion mobility but high redox rates.

In this case, the low ion mobility impedes the transport of metal cations from the active electrode to the inert electrode. The high redox rates allow for the formation of metallic nuclei within the matrix due to reduction of the impeded metal cations. As soon as a nucleus is formed, the gap between the nucleus and the active electrode will be filled by subsequently reduced metal cations. Thus, effectively the filament grows from the active electrode towards the inert electrode.

Case D: Low ion mobility and low redox rates.

In this case, the migration of metal cations through the matrix is impeded by the low ion mobility. The low redox rates prevent metallic nuclei from being formed easily in the matrix. In fact, the metal cations may pile up in the matrix until critical nucleation conditions are fulfilled and clusters are formed. The filament grows effectively from the active electrode towards the inert electrode. This case typically corresponds to the situation in matrices such as Si or SiO_2, in which the ion conductivities are very low.[58] The observation of a chain of Ag nanoparticles in a Ag/a-Si/Pt device was among the first *in situ* transmission electron microscopy (TEM) studies on the matter of filament formation in memristive devices.[65] However, the strong influence of the electron beam on the nanoscopic device imposes an additional depth to the interpretation of such *in situ* TEM investigations.[66]

These four cases show, that although the general set-up of an ECM memristive switching device is fairly simple and only involves the three components “active electrode”, “insulating matrix” and “inert electrode”, the choice of the materials for the individual components as well as the counter play between these components strongly affects the memristive switching characteristics.

In section 2.2.1, an overview on possible material combinations for ECM switching memristive devices is given (cf. Figure 9 and Figure 11). The mobile metal cations, typically Cu^{2+} or Ag^{+}, are transported through the matrix to the counter electrode. As matrix materials either ion conductors ($RbAg_4I_5$), mixed conductors (Ag_xS, Cu_xS, NiO) or insulators (TiO_2, Ta_2O_5, SiO_2, HfO_2) are applied. Many of these oxide insulators are also used in VCM memristive devices, thus they also exhibit a certain mobility of oxygen vacancies. The third component, the inert electrode or counter electrode, strongly impacts the ECM switching mechanism. The reason behind this lies in the electrochemical aspects of the redox reactions involved. In order to allow for a continuous ion migration within the matrix, the oxidation reaction at the active electrode as well as the reduction reaction are necessary, otherwise the Coulomb repulsion would act as an effective counter field for further ion migration. Accordingly, the slower reaction (reduction or oxidation) limits the switching kinetics of the memristive device. The Butler-Volmer relation describes the current density j_e at the electrode-matrix interface, which results from those electron-transfer reactions: [62]

$$j_e = j_0 \cdot \left[\exp\left(\frac{(1-\alpha) q}{k_B T} \cdot \left(E_o - E_{et} \right) \right) - \exp\left(-\frac{\alpha q}{k_B T} \cdot \left(E_o - E_{et} \right) \right) \right] \tag{2.22}$$

Here, j_0 denotes the current pre-factor, α is the charge transfer coefficient, E_{et} is the activation energy and E_o is the electron transfer overpotential. In case the overpotential is zero, the oxidation process (described by the first exponential term) and the reduction process (described by the second exponential term) occur at the same rate. For silver and copper as active electrode materials, the overpotential is typically very small.[42]

The electrochemical processes involved in the redox reactions with a cation-based memristive device can be investigated with cyclic voltammetry measurements for voltages below the switching voltages. In cyclic voltammetry, each reduction and oxidation process results in a specific peak in the IV loop. This method was used to investigate the oxidation state of the mobile cations, which turn out to be Cu^{2+} in case of copper and Ag^{+} in case of silver as active electrode. Also the effect of different counter electrodes on the redox reactions was studied.[58,67–70] Apart from a direct effect of the counter electrode to the redox reactions of the metal cations, also an effect on a parallel reaction with moisture was reported. In case the reduction reaction at the counter electrode itself is strongly inhibited, the additional reaction with moisture can serve as alternative route to achieve charge neutrality.[58] A good overview over the impact of different counter electrodes to the system Ag/SiO_2 is given by Lübben et al..[67]

An inhomogeneity of ion distribution during cycling of the memristive device can result in a deviation from the pinched hysteresis loop. This inhomogeneity leads to a potential difference across the device, which can typically reach several mV and implies a non-zero crossing in the IV hysteresis. This effect is called nanobattery effect and is observed for different ECM (and VCM) devices, such as $Ag/SiO_2/Pt$..[68,71]

There have also been reports on different approaches to alter the active electrode with respect to its morphology or composition. As already discussed, typically the metals Ag, Cu or Ni are applied as active electrode materials. The standard potentials for the relevant redox couples are:

Ag^{+}/Ag: 0.79 V
Cu^{2+}/Cu: 0.34 V
Ni^{2+}/Ni: -0.25 V

Accordingly, silver is the most noble among these three metals. By alloying the more noble gold (Au) to an Ag active electrode, a strongly facilitated release of silver (oxidation reaction) from the active electrode was reported, which resulted in a considerable decrease in electroforming voltage in $Ag(Au)/SiO_2/Pt$ devices.[72] Apart from manipulation of the active electrode material, also the approach of structuring of the active electrode for more defined switching has been reported, for example by using nanocones of silver or copper.[8,11] Additionally, also the use of nanoparticles in the context of memristive switching is discussed as a method to make use of the enhanced electrical fields between the nanoparticles for better switching characteristics.[73,74] In the framework of this thesis, the nanoparticle-based memristive device was developed and realised unifying these considerations on alloying and nanostructuring of the active electrode. In 2010, Jo et al. reported on a related memristive device, which relied on a layer of amorphous silicon with a gradient of embedded Ag nanoparticles.[7] This device exhibits analog switching behaviour without the need of electroforming, which was attributed to the collective shift in a front of silver within the matrix. Considering the information presented in this section, this explanation seems to need further refinement. According to "Case 4" described in this section, the absence of necessity of electroforming is more likely explained by the broad distribution of nanoscopic Ag particles, which merge together upon application of an external field. The analog switching would then be more likely a result of a multitude of nanoscopic filaments, whose general structure was predefined by the position of the nanoparticles in the matrix.

2.2.3 Modelling and Simulation of Memristive Switching

In the model of memristive devices and systems from Chua in 1976, memristive devices are described in a very general way.[33] This general model is shown in Eq.2.23 and Eq2.24. The output *y* is linked by a function *g* to the input *u*. The function *g* itself depends on the internal state *x* as well as the time *t* and the input *u*. The internal state *x* is treated as a n-dimensional vector and can be considered as a set of state variables x_i. The time derivative of the internal state variable *x* is described by a function *f*.

$$y = g\left(\vec{x}, u, t\right) \cdot u \tag{2.23}$$

$$\frac{\partial \vec{x}}{\partial t} = f\left(\vec{x}, u, t\right) \tag{2.24}$$

With this description it was possible to model the current voltage (IV) characteristics of certain systems and devices, such as thermistors, neon bulbs and Josephson junctions. Furthermore, even the Hodgkin-Huxley neuron model was modelled by Chua et al. using this set of equations. [33]

In 2008, Strukov et al. adopted this general model for memristive devices and related it to a TiO_2 thin film device.[2] Under the assumption of a current-controlled time invariant memristive device, Eq.2.24 can be transformed to Eq.2.25, in which the time derivative of the internal state variable ω is a function of the current *I* and the state variable itself. In analogy to Eq. 2.23, the voltage *V* is given by the product of the current and the resistance *R*, which is a function of the internal state variable and the current (Eq.2.26).

$$\frac{\partial \omega}{\partial t} = f\left(\omega, I\right) \tag{2.25}$$

$$V = R\left(\omega, I\right) \cdot I \tag{2.26}$$

From Eq.2.26 the most prominent feature of a memristive device can be concluded: the pinched hysteresis. Any IV hysteresis loop necessarily exhibits zero current at zero voltage. The occurrence of a hysteresis itself is strongly connected to the dependence of the resistance on the internal state variable.

The choice of a current-based model for memristive switching is at hand, because in the original proposal of a memristor, the memristance was defined as the link between the charge and the magnetic flux (as shown by Eq.2.12). The charge *q* itself is linked to the current *I* by the time derivative (Eq.2.27).

$$I\left(t\right) = \frac{\mathrm{d}q\left(t\right)}{\mathrm{d}t} \tag{2.27}$$

The model system proposed by Strukov et al. is a TiO_2 thin film with a thickness *D*, which is surrounded by two electrodes. The thin film can be separated into two subsections, one with high and one with low dopant concentration, which are connected in series. In such device,

the resistance varies between a high resistive state (with R_{HRS}) and a low resistive state (with R_{LRS}). The internal state variable describes the fraction of the TiO_2 thin film that is doped by oxygen vacancies and hence has a lower resistivity than the undoped region. Accordingly, the voltage is linked to the current by Eq.2.28.

$$V(t) = \left(R_{LRS} \cdot \omega(t) + R_{HRS}\left(1-\omega(t)\right)\right) \cdot I(t) \quad \text{with } \omega \in [0,1] \tag{2.28}$$

Any electrical field across the device will result in migration of the charged dopants (e.g. oxygen vacancies) and accordingly the ratio of the undoped and doped region will be changed. Assuming ohmic electronic conduction as well as linear ionic drift (with mobility μ_v), the corresponding change in internal state variable can be expressed by Eq.2.29.

$$\frac{\partial \omega}{\partial t} = \frac{\mu_v}{D} \cdot \frac{R_{LRS}}{D} \cdot I(t) \tag{2.29}$$

$$M(q) = R_{HRS}\left(1 - \frac{\mu_v R_{LRS}}{D^2} \cdot q(t)\right) \quad \text{with } M(q) = \frac{V(t)}{I(t)} \tag{2.30}$$

Inserting the time integral of Eq.2.29 into Eq.2.28 and assuming the resistance of the doped TiO_2 thin film to be much lower than in the undoped state, the memristance M of the model system can be formulated by Eq.2.30. With this expression, a link between the concept of a memristive device with the memristance as a characteristic property and an experimental representation of a resistive switching TiO_2 device is drawn. The Strukov model is well suited to describe some core features of memristive devices, such as the pinched hysteresis and its dependence on the cycling frequency (i.e. the ratio of R_{HRS} and R_{LRS} (ON/OFF ratio) depends on the voltage ramping rate which was used to record the hysteresis loop). However, this model describes analog switching behaviour and completely falls short in describing filament-based binary or multilevel switching as observed in the majority of VCM memristive switching devices, including this TiO_2 model system (cf. section 2.2.1). In addition, the model implies an ultimate retention time of the resistance state, which is in strong contrast to experimentally obtained memristive devices.

As the insights in the physical origins of memristive switching for different device classes grew, also more elaborate models were proposed to describe either of the various memristive device classes.[75–78] In general, two different approaches were commonly pursued to enhance memristor models: On the one hand the abstract linear model such as presented by Strukov et al. was refined by introducing appropriate window functions to confine the internal state variable to a certain interval (typically between 0 and 1, c.f. Eq.2.23).[79–84] On the other hand, models were developed on the basis of the physical origins of memristive switching and in those models the internal state variable is closely linked to a physical quantity (e.g. tunnel barrier width).[76,78] A good overview on the various models for memristive switching and their applicability in the context of simulations is given in the work of Ascoli et al. and Linn et al..[75,77]

By applying molecular dynamics simulations (MD), it was possible to investigate processes on the atomic level on very fast time. Examples for such studies are MD simulations on field-enhanced ion transport in solids and the atomic origin of switching in nanoscale ECM devices.[85,86] Kinetic Monte Carlo simulations (KMC) were used to study charge carrier motion in ECM[56,87], VCM[88] and interface type memristive devices[57] at longer time scales, allowing to gain insights on many consecutive switching cycles. These studies offer good observability of the underlying processes of memristive switching on different time scales and have a certain predictive power for the development of new memristive devices.

However, due to the high computational effort, such simulations are not able to describe the memristive properties of a device in real time. For this purpose, a wave digital synthesis based emulation of a double barrier memristive device was developed, which allows for real time emulation of single devices and an integration into electrical circuits.[87]

2.2.4 Application Scenarios

The main motivation to incorporate memristive devices in application scenarios is twofold: On the one hand, the unique electronic properties of memristive devices inspire applications that go beyond conventional electronics, such as using memristive devices as programmable interconnects, to realise logics for in array computing or in neuromorphic engineering.[16,43,44,89–92] On the other hand, memristive devices are under investigation as non-volatile memory (NVM) with advantageous characteristics in conventional computing architectures.

As the concept of memsensors falls into the first application scenario, the discussion of the applicability of memristive devices will be mainly limited to general application considerations alongside the integration of single devices (in this section) and neuromorphic engineering (in the next section). In order to provide the full picture, a general overview on the topic of memory applications of memristive devices is given in Appendix A.

For application purposes, memristive devices are typically arranged in crossbar arrays[93] to make use of the potentially small footprint of a single memory cell. A w **x** b crossbar array is an arrangement of w parallel wires (word lines) stacked with the active layer (in this case memristive devices) and b parallel wires (bit lines). The bit lines are rotated by 90° with respect to the word lines, thus the term "crossbar". Each crossing point corresponds to an individual memory cell $c_{i,j}$ (e.g. memristive device). In a crossbar array each single cell $c_{i,j}$ can be addressed individually by applying a voltage between the corresponding word line i and bit line j. A typical problem in crossbar arrays with memristive devices are sneak path currents or leakage currents.

Sneak path currents may flow through half-selected (cells that share either the word or bit line with the selected cell) or non-selected cells. This could result in read errors in case the selected cell is in its HRS. In addition, the sneak path currents can contribute strongly to the power dissipation, because the number of half- and non-selected cells is far larger than the individual selected cell.[94] Although large crossbar arrays seem beneficial for their effective area usage, there are several drawbacks to large array sizes: With increasing size, also the length of the individual wires for the word and bit line has to increase. This results in a considerable increase in resistance and capacitance, especially at advanced technology nodes, in which the width and spacing of the wires approaches nanometer dimensions.[95,96]

In order to avoid the sneak path problem, selector devices are discussed as additional elements in the crossbar array, which offer a high nonlinearity. A variety of selector devices, including the use of transistors, diodes or bipolar two-terminal selectors, is under discussion for the application in crossbar arrays of memristive devices.[94,95] Field-effect transistors, although offering excellent nonlinearity and being well established, are three terminal devices and as such impose a high constraint on the scaling of the whole crossbar array. The nanoparticle-based memristive devices prepared in the framework of this thesis exhibit diffusive memristive switching characteristic. Amongst others, diffusive switching

memristive devices and complementary memristive switching devices, which are made up of two memristive devices in an anti-serial connection, are discussed to be highly promising in the context of two-terminal selector devices.[94,95,97]

2.3 Neuromorphic Engineering with Memristive Devices

Despite the ubiquitous presence of modern silicon-based computing devices, there is one particular class of computing devices that still outnumbers them: neural networks, such as the brain, which are found in a plethora of species and basically on every inch of this world. These neuronal systems have been optimised by ages of evolution, enabling the individual to efficiently survive in its environment. As such, the human brain is able to perform advanced computing tasks, such pattern separation and completion, with ease at an extremely low power consumption and low frequency of neuron spiking. The foundation of this outstanding efficiency and robustness of the operation in neural networks is given by the complex underlying structure: In a human brain, the respective neurons are interconnected in a highly parallel manner and with a certain hierarchy (i.e. different brain regions), resulting in the capability of dynamic parallel reconfiguration and a certain level of redundancy. The individual neurons and synapses act as processing units and memory in itself and the event-driven scheme of computation allows for energy to be consumed only when and where it is needed for processing of the information.

Neuromorphic engineering describes the effort to mimic neural structures and transfer certain aspects of their advanced functionalities into electronic circuits. The field of neuromorphic engineering evolved in the late 1980s around the work of Carver Mead on the realization of neuron-inspired devices like an adaptive retina in terms of integrated electronic analog systems.[98] Since then, the concept of neuromorphic engineering was extended to approaches ranging from deep learning networks, which typically rely on conventional von-Neumann-based computing devices and elaborate software, to the realization of biologically inspired computing paradigms on the basis of novel hardware components. Although the latter approach is still far from reaching full technological maturity, it exhibits a stunning long-term research potential as it imposes high promises on the realization of highly parallel, efficient, biologically motivated computing devices.[99]

Memristive devices are considered as very interesting in this particular field of neuromorphic engineering, as they are capable to mimic certain aspects of neurons and synapses (representing the connections of two neurons) as depicted in Figure 13 a. In particular, memristive devices are applied as the electronic analogue of synapses. Especially interesting in this area are memristive devices with analog, multilevel switching characteristics, which respond to the application of voltage pulses by a gradual reversible change in resistance (Figure 13 b). The link between memristors and the Hodkin-Huxley model for neurons was already drawn in the work of L. Chua in 1971.[32] The matter of spiking neuron models for single neurons as well as neuron assemblies is explained in full detail in the comprehensive book by W. Gerstner and W. Kistler and will not be discussed in more detail here.[100] In its essence, the neuron is by default in its resting state and can be excited by a sufficiently large stimulus to expose a voltage spike (action potential). After this spiking event the neuron is in a refractory period and further spiking events are effectively suppressed. Upon connecting two neurons by a synapse, the change in synaptic weight (essentially describing the resistance of this connection) is governed by the time interval between the spiking events in the pre- and postneuron (top and bottom neuron in Figure 13 a). In other words, an adequate

time interval leads to a strengthening of the synaptic connection, while a mismatch in spike timing leads to a weakening of the connection. This so-called spike-timing dependent plasticity (STDP) is illustrated in Figure 13 c. Depending on the time difference, the synaptic weight is increased (long–term potentiation, red graph) or reduced (long-term depression, blue graph), basically relating to learning. This behaviour is readily reproduced by artificial neuronal and synaptic devices based on memristive devices.[98,110,111] Two-terminal memristive devices offer a high potential for integration of large numbers of such artificial synapsed with high density into cross-bar arrays. In this context, also multilayer networks with one or more hidden layers (much like in software-based deep learning) are in the focus of investigation. A good overview over the research activities in this field is given by the reviews by T. Chang et al. and by D. Ielmini.[101,102]

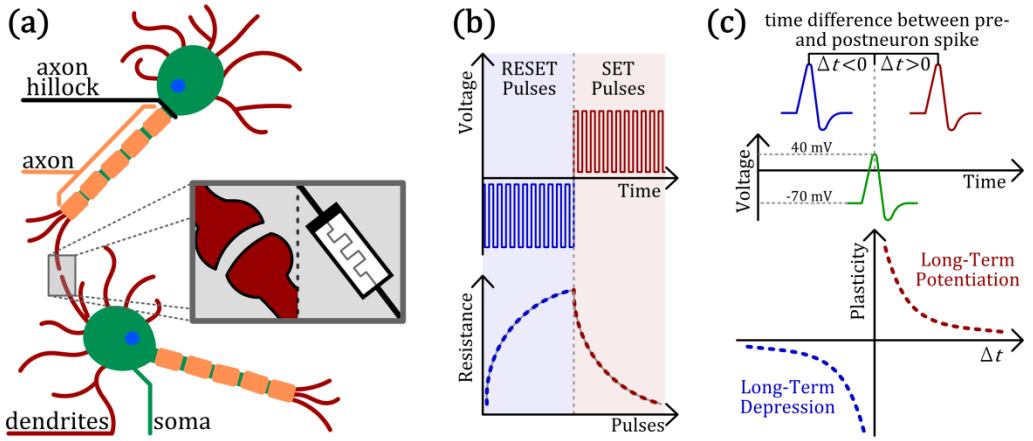

Figure 13: (a) Simplified schematic depiction of two neurons and the main constituents, upon connection of the two neurons a synapse is formed (grey inset). In neuromorphic engineering, memristive devices (grey inset) are applied to reproduce synaptic behaviour. Memristive devices with analog switching behaviour exhibit a gradual resistance change to subsequent voltage pulses (b), indicating high applicability for example for mimicking spike timing-dependent plasticity (c). As observed in neurons [103,104]**, the time difference between the preneuron spike (red and blue) and the postneuron spike (green) impacts the change in plasticity. In this context, long –term potentiation (red) and long-term depression (blue) are readily reproduced by artificial neuronal and synaptic devices based on memristive devices.**[101,105,106]

Apart from mimicking STDP, memristive devices are also under consideration for the realization of further biologically motivated functionalities, e.g. spike frequency adaptation has been reported in memristively coupled oscillators.[15,107] One particularly important aspect in biological neural networks is the close connection between signal detection and processing. In fact, neurons are not only to be found in our brain, but are spread over the whole human body and serve to transmit and process sensory signals. Until recently, in the field of neuromorphic engineering this aspect has remained mainly unaddressed. The concept of memsensors promises to offer a technical realization of the close connection of signal detection and processing by merging sensing and memristive switching.

2.4 Sensing with Metal Oxide Nanostructures

The use of sensors in contemporary electronics is ubiquitous, ranging from distance sensors in cars and acceleration sensors in mobile phones to anti-theft protection devices installed at almost any store. The term sensor in its most general meaning is described in the Oxford Dictionary as follows: [108]

"A device which detects or measures a physical property and records, indicates, or otherwise responds to it."

Such broad definition serves the purpose of describing the broad diversity of sensors, which are applied in different application scenarios. In the context of this thesis, metal oxide nanostructures are investigated as an especially promising class of sensors. Accordingly, a sensor in the context of this thesis is a two terminal device that features a metal oxide structure (e.g. thin film or nanowire). At least one physical quantity (e.g. the resistivity) of the sensor device depends on an externally applied stimulus. Stimuli can be, amongst others, the presence of gas molecules attached to the surface of the sensor or photons. The four main criteria for the description of the performance of a sensor are its sensitivity, selectivity, speed and stability.

The sensitivity S describes the ratio of the device resistances in the presence or absence of a stimulus, which can be in analogy to the states in memristive devices described as the high resistance state (R_{HRS}) and low resistance state (R_{LRS}).[18]

$$S = \frac{R_{HRS} - R_{LRS}}{R_{LRS}} \tag{2.31}$$

Typically, sensors are optimised with respect to a high sensitivity. From Eq. 2.31 can be concluded, that the sensitivity can be increased by either increasing R_{HRS} or decreasing R_{LRS}. However, in order to allow for low power operation, an increase in R_{HRS} is the more viable option, as long as it does not impact the readability of the signals.

The selectivity of a sensor describes its sensitivity towards multiple stimuli. A single sensor device can be sensitive to more than one stimulus. In case of a gas sensor for example, the resistance of the device can be impacted by different applied gas species. In case of a photon sensor, the device can change its resistivity for photons of different wavelengths. A high selectivity indicates, that the sensor responds highly to one stimulus while being unaffected by other stimuli.

The third sensor criterion is the speed of operation, which is characterised by the response time and recovery time. Assuming a step-wise applied stimulus (rectangular stimulus signal), the sensor's resistance changes with a certain time delay. The response time is defined as the time that the sensor needs to reach 90% of its final resistance under the applied stimulus. The recovery time is defined analogously with respect to the withdrawal of this stimulus. These definitions for response and recovery time are visualised for an idealised sensor device in Figure 14 a.

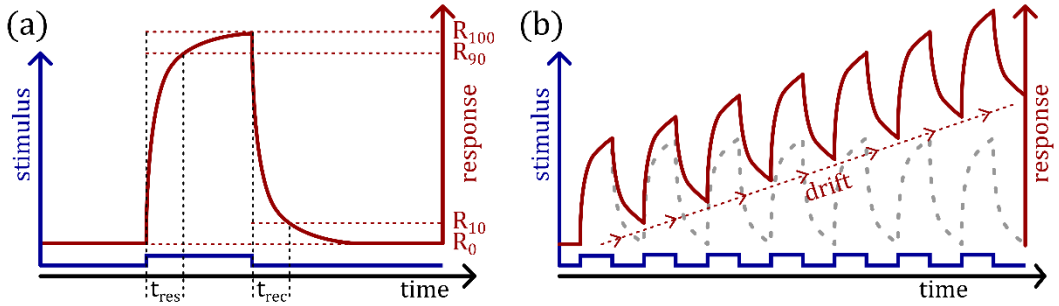

Figure 14: (a) Dynamic response (red line) of an idealised sensor to a square stimulus signal (blue line). The response time (t_{res}) is defined as the time between the application of the stimulus and the time, when the sensor response reaches 90% (R_{90}) of the final response (R_{100}). The recovery time (t_{rec}) is defined as the time between the withdrawal of the stimulus and the time, when the sensor response reaches 10% (R_{10}) of the final response (R_{100}); (b) Drift in the sensor response (red line) upon application of multiple consecutive stimulus pulses. For comparison, the sensor response without drift (dotted grey line) is shown.

The stability of a sensor device describes its long term applicability with respect to multiple stimuli cycles. In case the response is gradually altered for consecutively applied stimulus pulses, the sensor is prone to drift. This phenomenon is depicted schematically in Figure 14 b. In addition, aging of the sensor may lead to long-term changes in the sensor response, i.e. the response of a certain sensor to an identical stimulus changes with the shelf time of the sensor. Typically, sensors are optimised to yield the identical response to stimulus pulses over the whole lifetime.

In addition to the aforementioned four main criteria commonly associated to the development of sensors on the basis of metal oxide structures, for a practical application of such sensors further aspects have to be considered. This includes, amongst others, the signal-to-noise ratio of a sensor structure, which in turn relates to the lower limit of detection. While in the idealized sensor response as shown in Figure 14 a no noise is present, in typical sensor devices the response undergoes certain fluctuations, limiting the detectability of response towards low stimulus strengths.

In this section, gas sensing and photon sensing as two examples for sensing stimuli will be discussed and typical metal-oxide-based devices as well as the underlying sensing mechanism will be explained. Nanostructures are commonly regarded as especially promising sensor devices, because the surface to volume ratio increases drastically the smaller the characteristic length scale of the nanostructure gets. A good summary of metal oxide nanostructures applied in the field of photon-sensing and gas sensing is given in the work of Tian et al. and A. Dey and G. Korotchenkov respectively.[18,19,109]

2.4.1 Photon Sensing

Sensing of photons, especially in the ultra-violet (UV) range, is motivated by a broad range of applications, including fire monitoring, environmental monitoring and biological analysis.[19] Nanostructures of binary or ternary metal oxides, such as ZnO, SnO_2, Nb_2O_5, TiO_2 or Zn_2SnO_4, are widely investigated as promising sensors for UV photons. Typically,

these materials are used in a metal-semiconductor-metal structure. Another development is the use of Schottky barrier modulated photosensors, which will not be discussed here.[19] The metal oxide semiconductor materials are commonly wide band gap semiconductors with band gaps around 3 eV (e.g. TiO_2 with a band gap between 3.0 eV and 3.2 eV for rutile and anatase respectively or ZnO with a band gap of 3.3 eV). The stimulus in case of UV sensors is the presence of photons with a wavelength in the UV range. Without stimulus, the sensor device is in its high resistance state with only the dark current going through the device. As soon as the sensor is irradiated by UV photons of sufficient energy to overcome the band gap, electron hole pairs are generated and the free charge carriers lead to a drastic increase in conductivity. Accordingly, the overall resistance of the sensor is decreased; the device is in its low resistance state.

Two additional criteria for the performance of UV photon sensors are commonly considered, which are the spectral responsivity R_λ and external quantum efficiency *EQE*. The external quantum efficiency is given by Eq.2.32 and essentially describes the number of electrons that are detected per incident photon. Here, *h* is the Planck's constant, *c* the velocity of light, *e* the elementary charge and λ the wavelength of the incident photons. The spectral responsivity R_λ is defined as the ratio of the photon induced current (I_{light}-I_{dark}) and the product of the light intensity *P* and the irradiated area *A*.[19]

$$EQE = \frac{h \cdot c}{e \cdot \lambda} \cdot R_\lambda \qquad \text{with } R_\lambda = \frac{I_{light} - I_{dark}}{P \cdot A} = \frac{V \cdot \frac{R_{HRS} - R_{LRS}}{R_{LRS} \cdot R_{HRS}}}{P \cdot A} \tag{2.32}$$

The application of nanostructures (e.g. nanowires) in the context of photon sensors yields many advantages: The high surface to volume ratio of the nanostructures leads to an increased number of surface trap states and prolonged charge carrier lifetimes. In combination with the small effective area *A* in such nanostructures, this results in short transit times and an overall increases responsivity. In terms of low power operation, the nanoscopic dimensions limit the dark current.

2.4.2 Gas Sensing

The investigation of gas sensors is motivated by their applicability in the field of environmental monitoring of toxic, flammable or hazardous gases. Semiconducting metal oxide (SMO) gas sensors are considered as very promising materials for gas sensing applications. Especially transition metal oxides such as ZnO, CuO, TiO_2 and FeO_x exhibit a high research interest and are widely investigated.[18,109–113] In this section, the underlying gas sensing mechanisms for typical SMO gas sensor devices will be discussed. A detailed and comprehensive introduction into the underlying mechanisms of gas sensing as well as a rational material choice for SMO gas sensors is given in the work of G. Korotchenkov.[109] In addition to gas sensing by SMOs, also a variety of sensors, relying on different of sensing mechanisms has been reported. These include gas sensors based on changes in infrared

absorption, thermal conductivity or catalytic combustion and will not be topic of this section.

As indicated by the name, the active material in a SMO gas sensor is a metal oxide semiconductor. The band gap of typical SMO materials is in the order of 3 eV (cf. section 2.4.1). The presence of adsorbed gas species at the surface of the semiconductor alters the electrical properties of the sensor material. Accordingly, nanostructures are also highly favourable here, as they provide a high surface to volume ratio. In contrast to photon sensing, which allows for operation of the sensor at room temperature, typical SMO gas sensors are commonly operated at elevated temperatures. The respective operating temperature is given by the underlying surface or bulk conductance effects, with surface conduction being possible at lower temperatures than bulk conduction.[18] However, even for typical surface conducting materials such as SnO_2 or ZnO, operation temperatures commonly range from 300-500 °C. Accordingly, another goal in sensor design is lowering the operation temperature in order to allow for a broader application window of the sensor.

The gas sensing mechanisms in SMO gas sensors are diverse and strongly depend on the specific material and respective gas molecules. In general, the SMO is a wide band gap semiconductor with a high resistance in its pristine state. At the surface of the metal oxide, chemisorbed oxygen extracts electrons from the conduction band of the metal oxide and forms a space charge layer. When a gas atom or molecule approaches the surface, it alters the surface chemistry of the sensor e.g. by replacing chemisorbed oxygen. The width of the space charge region is consequently changed, which impacts the resistance of the overall device depending on the adsorbed gas species. Typically, oxidizing and reducing gases are distinguished. The sensitivity of the sensor is measured with respect to its initial resistance in a standard gas atmosphere (typically air). In case of a n-type semiconductor, the resistance of the sensor decreases when subjected to a reducing gas and increases when subjected to an oxidizing gas (vice versa in case of a p-type SMO).[18]

The importance of surface reactions reveals to be a strong difference to photon sensing as described in section 2.4.1. While the photons can penetrate rather deep into the “bulk” of the nanostructures, the gas molecules undergo surface reactions. The surface acts as a receptor for the gas molecules while the whole microstructure of the metal oxide sensor acts as a transducer for the resistance change.

A further criterion in case of gas sensors in addition to stability, speed, sensitivity and selectivity is the lower limit of detection, which describes the lowest concentration of gas molecules to which the sensor responds. For the detection of hazardous gases, the lower detection limit is an important criterion and sensors are optimised in order to detect even trace amounts of the respective gas (down to the ppb regime).

2.4.3 Nanoparticle-decorated Metal Oxide Sensor Devices for Enhanced Sensing

A further route of optimizing metal oxide photon and gas sensors for enhanced sensing is their decoration by nanoparticles. In this approach, nanoparticles are deposited onto the metal oxide thin film or nanostructure (e.g. nanowire). Typically, the nanoparticle film is well below the percolation threshold in order to maintain undisturbed access of the stimulus to the metal oxide thin film. Among others, nanoparticles of other SMO materials and in particular noble metal nanoparticles are applied to enhance the sensing properties of SMOs.[114–119] In Figure 15 common materials for metal nanoparticles (green colour) as well as metal oxide photon sensors (orange colour) and gas sensors (yellow colour) are summarised.

In case of photon sensors, two general approaches are pursued to enhance the sensing properties. On the one hand, the plasmonic properties of the noble metal nanoparticles (typically Ag or Au) are employed to extend the usability of the sensor structure (such as TiO_2 which is typically limited to the detection of UV photons) towards the wavelength of the localised surface plasmon peak associated to the respective nanoparticle (e.g. in the visible spectrum in case of Au NP). In this approach, upon plasmonic excitation of the nanoparticles, hot electrons can be injected into the SMO thin film.[120–122] On the other hand, a localised Schottky-junction is formed at the contact of noble metal nanoparticles (which exhibit a high work function) with the nanowire (e.g. ZnO). This creates charge depletion at the interface and hence reduces the dark current (which translates to an increase in R_{HRS}). This in turn increases the sensitivity of the sensor, as demonstrated by Liu et al. at the example of Au nanoparticle decorated ZnO.[123]

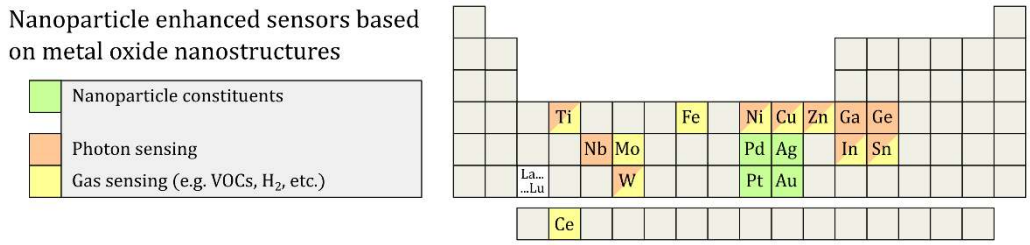

Figure 15: Schematic overview over common metal oxide micro- and nanostructures for (UV) photon sensing (orange colour) and gas molecule sensing (yellow colour).[18,19,109,112,113,124] **Typical metals for enhanced sensing due to metallic nanoparticle decoration are shown by green colour.**[19,114,123,125]

In case of gas sensors, noble metal nanoparticles are mainly used due to their catalytic properties, which in turn influence the surface reactions of the respective gas species with the SMO sensor. The resistance of a SMO gas sensor is strongly influenced by the space charge region which is formed in the vicinity of the sensor surface. This space charge region forms mainly due to the adsorption of atomic oxygen species and is altered as soon as other gas species adsorb at the surface. The catalytic properties of the nanoparticles alter the kinetics of these reactions and thus impact also the operational speed of the sensor.[126] In addition, also an increase in sensitivity of the respective sensor as well as its selectivity towards a specific gas species are commonly reported.[114,126] In their work on Pt-nanoparticle decorated In_2O_3 nanorods, Choi et al. reported on three general ways, how the

addition of the noble metal nanoparticles impact the gas sensing performance.[114] On the one hand, the effect of electrical sensitization due to the large work function (6.35 eV in case of Pt) in comparison to the SMO (5.0 eV in case of In_2O_3) leads to a transfer of electrons from the SMO to the nanoparticle. Accordingly, an additional electron depletion layer is formed at the interface between SMO and metal nanoparticle. On the other hand, the effect of chemical sensitization results in an enhanced adsorption of gas molecules (NO_2 for the example of In_2O_3 with Pt nanoparticles). This enhanced adsorption leads to a further expansion of the electron depletion region upon reactions of the adsorbed NO_2 gas species. Finally, the application of nanoparticles increases the surface to volume ratio of the SMO structure, which typically benefits the gas sensing performance.

2.4.4 The Junction of Memristive Switching and Sensing

The majority of the sensor devices discussed in the previous part of this section are optimised for high sensitivity, high selectivity and fast response and recovery times. Drift and other time dependent resistance changes are typically undesired in classical sensor design. However, many materials under investigation for a potential application as UV photon sensors or gas sensors, such as TiO_2, Nb_2O_5 or ZnO, are also investigated in the context of memristive switching, where time dependent resistance changes are explicitly desired. Considering the use of certain materials in both application scenarios, the combination of the characteristic features of memristive devices (i.e. a pinched IV hysteresis) and sensors (i.e. stimulus dependent resistance) into a single device appears to be possible. Throughout this thesis, such a device that at the same time acts as a sensor as well as a memristive device will be termed “memsensor”.

Among the first experimental realizations of the combination of memristive switching and sensing properties was a light sensitive Si/Al_2O_3 stack[20] as well as single Si nanowires with bio-sensing capabilities[21]. A variety of memsensor devices has been reported since, including mechanically stimulated CuO nanowires, crossbar memristive devices with nanostructured top electrodes for oxygen sensing and light- and magnetic-field-sensitive memristive devices based on Ag cation switching with a FeMn spacer layer.[22,23,127]

Commonly, such devices are manufactured either in horizontal geometry or vertical geometry, as schematically depicted in Figure 16. The main concern in the design of a memsensor is the accessibility of the active layer to the respective stimulus. A variety of stimulus signals for the sensitive part has been reported, including photons, gases, biomolecules, pH, mechanical response, magnetic field and temperature. In general, the horizontal design offers good accessibility towards the stimulus. Depending on the stimulus type, the accessibility in case of a vertical design can be achieved by using a transparent top electrode (i.e. photons as stimulus) or by nanostructuring.

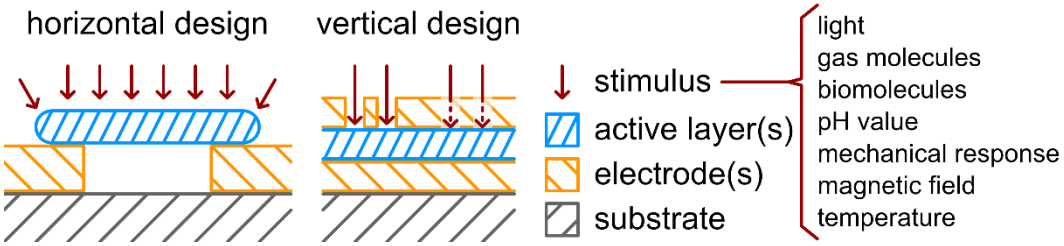

Figure 16: Schematic cross section through a typical memsensor with horizontal and vertical design. A variety of stimulus signals has been reported for use in memsensors (e.g. light, etc.). In case of a horizontal design, the active layer (e.g. nanowire) is open to any stimulus. In case of a vertical design, the stimulus must not be blocked from reaching the active layer, which can be accomplished by structuring of the top electrode (e.g. for gas molecules) or the choice of a transparent top electrode (e.g. ITO for light). Image taken from Ref. [128]

The combination of memristive switching and sensing properties allows for a broad application potential for memsensor devices. For example, Zhu et al. used a crossbar array of stacked sensitive and memristive elements to resemble features of an electronic skin and Chen et al. used an array of In_2O_3 nanowires and $Ni/Al_2O_3/Au$ memristive switches to design a visual memory system.[129,130] In a recent approach, the junction of sensitivity towards external stimuli (e.g. light) and memristive switching was studied in order to achieve optical memristive switching or an optical synapse.[24,25]

A memsensor device may show further properties in addition to its inherited properties, which are the stimulus dependent resistance and pinched IV hysteresis. The advanced functionalities include adaptation to the stimulus, that may arise from the junction of sensitive and memristive devices.[128]

2.5 Deposition of Thin Films and Nanoparticles

Sensors and memristive devices typically rely on nanostructures or single or multiple thin films (e.g. metal-insulator-metal structures for memristive devices). In this context, the term thin film is defined as a distinct layer of a certain material, and this layer is nanoscopic in one dimension (i.e. height). This distinguishes a thin film from a nanoparticle, which is nanoscopic in all three dimensions (e.g. a sphere with a diameter in the nanometer range) and a nanowire, which is nanoscopic in two dimensions.

The devices and samples fabricated in the framework of this thesis were commonly realised by a number of subsequent physical vapour deposition (PVD) steps. Based on the experience of the Chair for Multicomponent Materials in the field of magnetron sputter deposition, this method was applied within the framework of this thesis for the preparation of thin films and nanoparticles from the gas phase. Accordingly, this section focusses on sputter related deposition of nanoparticles as well as thin films. A broader overview over a variety of typical deposition methods in the context of thin films and nanostructures for memristive and sensitive devices as well as the basic principle of the sputtering technique is given in Appendix B.

In a physical vapour deposition process such as sputter deposition, atoms of the chosen solid-state source (target) are brought into the gas phase and are transported to the substrate, where a thin film is formed. Prior to the deposition process the deposition chamber is evacuated in order to increase the mean free path of the respective species in the gas phase and to ensure the formation of reproducible working conditions with a low level of contaminations. Essentially, in sputter deposition a plasma (typically from an inert gas like argon) is ignited in the vicinity of the target and positively charged argon ions are accelerated towards the target due to the applied potential. The high energy impact of ions leads to a collision cascade, due to which atoms from the target are ejected towards the substrate. The magnetic circuit below the target in a typical magnetron results in a magnetic field, inducing a circular trajectory of plasma electrons due to Lorentz force, which results in a higher ionisation rate of the plasma. The majority of thin films and nanoparticles discussed in this work were prepared on the basis of the method of magnetron sputtering.

2.5.1 Thin Film Deposition by Magnetron Sputtering

In this section, the applicability of magnetron sputter technique for the deposition of metal and metal oxide thin films will be discussed. Especially for sensing applications, the morphology of the deposited thin film influences the sensing properties. Consequently, an additional focus of this section lies on the influence of typical deposition parameters on the morphology of the deposited thin films.

In conventional DC sputter deposition, the electrical conductivity of the target material is a critical parameter. Materials with a high conductivity are typically good candidates for usage in a DC sputter deposition setup, while insulating materials (such as SiO_2) require additional efforts. The low conductivity of such materials prevents the necessary current flow and any

charge accumulated at the surface layers of the target (e.g. by the impinging positively charged ions) would result in a repulsion of further gas ions. As a result, metallic thin films can be readily deposited by DC magnetron sputter deposition, while sputtering of oxide compounds such as SiO_2 is more complex.

One way to deposit thin films from highly insulating targets is radio frequency (RF) sputter deposition. Instead of using a DC voltage, with this method an AC signal with a typical frequency of 13.56 MHz is applied to the electrodes. This allows overcoming the problem of low conductivity, because the impedance of a capacitor is inversely proportional to the AC frequency. Further details on the method of RF sputter deposition can be found in the introductory textbook by M. Ohring.[131] Common concerns about the RF approach are, apart from the costly equipment, the low deposition rates and the tendency to deposit thin films with an oxygen deficient stoichiometry. As especially the stoichiometry is crucial in memristive devices (cf. VCM switching in section 2.2.1), this limits the usability of RF sputter deposition from metal oxide targets in the context of this thesis.

Another approach to prepare compound thin films (e.g. SiO_2 or CuO) is reactive sputtering from metallic targets (e.g. Cu). This approach was applied within this thesis to deposit oxide thin films, such as TiO_2, CuO or SiO_2. In this case, in addition to the inert process gas (Ar), also a reactive gas (e.g. O_2) is supplied. The reactive gas can undergo reactions with target atoms and form compounds with tuneable stoichiometry. The flow rate of the reactive gas strongly impacts the processes involved in reactive sputter deposition. Without any reactive gas, the target remains metallic and the deposition rate is high. Increasing the flow rate of the reactive gas, the deposition rate is not strongly affected, until the adsorption rate of the reactive gas at the target surface exceeds the sputtering rate. In this case, the target surface has completely reacted with the reactive gas, which results in an insulating surface layer on the target. This state is commonly termed as “target poisoning”, because the insulation layer charges up due to the impingement of positive ions and the voltage necessary to sustain the sputter process increases. In this state, the deposition rate is drastically decreased. A thorough discussion of the method of reactive sputter deposition is given in the book of D. Depla.[132]

In order to maintain suitable sputtering conditions, the DC signal at the electrodes can be pulsed. The pulse frequency is typically in the kHz range and each pulse consists of a ON and an OFF section. During the ON section, the target is at negative potential and the target material is sputtered by impinging gas ions. Similar to target poisoning, positive charges can accumulate in an insulating surface layer on the target during the ON section of the pulse. This charging is subsequently compensated in the OFF section of the pulse. In case of bipolar pulses, the target is put on a positive potential and electrons are drawn towards the target and neutralise the accumulated charges. In case of unipolar pulses, in the OFF section there is no potential applied to the target. The positively charged surface however attracts mobile electrons, which equilibrate the surface charges.

The morphology of thin films deposited by sputter deposition depends on the reduced temperature and the kinetic energy of the deposited atoms (which in turn relates to the

pressure). The different morphologies, which are typically occurring in sputtered thin films are summarised and described by the so called Structure Zone Model (SZM).[131,133,134] In its initial form, the idea for a SZM was proposed by Movchan and Demchishin in 1969 and refined by Thornton in 1977 for sputter deposited thin films. The morphology of thin films deposited by sputter deposition ranges from fibrous grains with a high number of voids over columnar grains with dense grain boundaries to large equiaxed grains. In 2010, A. Anders revised the SZM and expanded it by the possibility to describe ion etching processes (which can be regarded as negative thin film growth rates) and by abstracting the axes from primary parameters (such as pressure) to film growth process related parameters (such as kinetic energy of the deposited atoms).[133] In this work, the availability of oxygen in the reactive gas atmosphere will be discussed as an additional degree of freedom which impacts the morphology of oxide thin films deposited by reactive pulsed unipolar DC magnetron sputtering.

2.5.2 Nanoparticle Deposition

The methods for the synthesis and deposition of nanoparticles are as diverse as the unique properties of the nanoparticles themselves. Besides a broad variety of solution based approaches, including the sol-gel based Stöber process for SiO_2 nano- and microparticles[135], microfluidic assisted deposition of metal and polymer nanoparticles in various shapes[136–138], metallic nanoparticles like Ag NP by synthesis with diethyleneglycol [139] and the synthesis of metal nanoparticles on photocatalytic surfaces by photoreduction[140], also PVD-based methods are widely applied. Conventional PVD techniques as discussed in section 2.5.1 can be applied to deposit nanoparticles on thin film surfaces by self-organization. This approach was also demonstrated for alloy nanoparticles in nanocomposites by co-sputtering [141,142] and co-evaporation[143,144] with two distinct sources. Instead of using a solid substrate, nanoparticles can also be introduced into a gel-like substrate by so called “sputtering into liquids” [141].

In this section, the deposition of nanoparticles by using a gas aggregation source (GAS) and magnetron sputtering will be discussed in more detail. This type of deposition method was developed by H. Haberland et al. in 1992.[145] Essentially, a GAS nanoparticle deposition setup consists of a conventional vacuum chambers with two distinct subchambers, which are separated by a small orifice. In magnetron-based GAS systems, atoms of the target material are brought into the gas phase by magnetron sputtering. The gas inlet for the process gas for the sputter process is attached to one subchamber (high pressure subchamber), while the pumping equipment is connected to the other (low pressure subchamber). Accordingly, the gas flow and the small orifice size result in a pressure gradient between both parts. This pressure gradient acts on the nanoparticles, which are generated in the subchamber with the magnetron attached. Consequently, a beam of nanoparticles leaves the high pressure subchamber through the orifice and enters the low pressure subchamber, where the nanoparticles are deposited onto the respective substrate. This basic setup is schematically depicted in Figure 17. In order to allow for a higher control over the respective pressures in each subchamber, the basic concept can be expanded by differential

pumping, i.e. adding an additional connection between the high pressure subchamber and the pumping system.

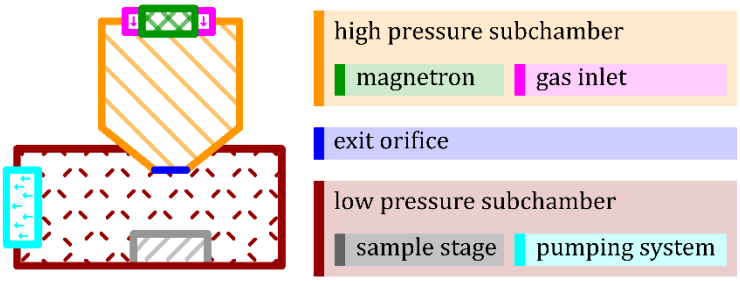

Figure 17: Schematic cross section through a typical gas aggregation source (GAS) deposition setup. The gas inlet is applied to the high pressure subchamber, which is separated by the exit orifice (typically with a radius in the range of some 100 µm) from the low pressure subchamber.

Applying this physical vapour deposition method, nanoparticles are generated from individual atoms (typically metal atoms), which were brought into the gas phase for example by sputtering. The formation of nanoparticles in such gas phase synthesis involves three important processes, which are sketched schematically in Figure 18.

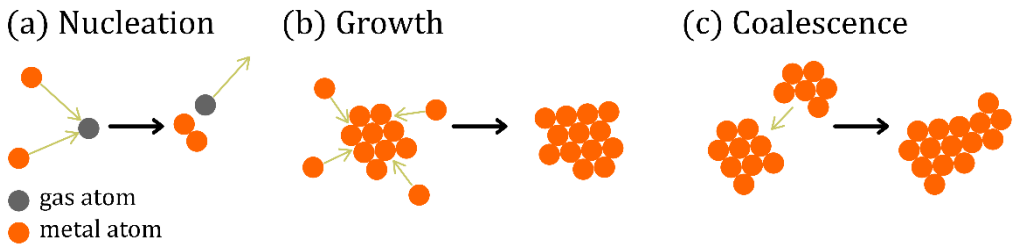

Figure 18: The nanoparticle growth mechanism inside the GAS involves a three-body collision process (a) for the formation of stable nuclei as well as consecutive nuclei growth (b) and coalescence (c).

In a first step (a), nuclei are formed in a three-body collision process, involving two sputtered atoms. The third collision partner is a gas atom that allows for transfer of excess energy to prevent the nucleus from disintegrating. As the likelihood of this three-body collision process depends on the concentration of sputtered atoms as well as gas atoms, the process is typically run at rather high pressures (pressures around 100 Pa are reported repeatedly). In addition to this homogenous nucleation process, also the impact of reactive species, such as traces of oxygen gas or water vapour, are reported to strongly affect the nanoparticle formation process.[146,147] In this context, the additional oxygen is commonly thought to facilitate the formation of stable nuclei.[146]

The stable nuclei undergo subsequent collisions with further metal atoms (b, growth) or other nuclei (c, coagulation and coalescence), which leads to further growth of the nanoparticles up to their final size. A full coverage of the basic principles of the growth mechanism of nanoparticles by GAS is given in the book of Y. Huttel.[148]

Since its initial proposal, the concept of the gas aggregation cluster source was readily adopted and expanded. The application of additional magnetrons in the high pressure subchamber allows for the deposition of nanoparticles with more than one constituent in deliberate compositions. In the framework of this thesis, a novel approach for the deposition of alloy nanoparticles from a single target has been developed.[149] This deposition technique is discussed in detail in section 4.1.1. In addition to alloy nanoparticles, further geometries like core-shell nanoparticles have been reported.[147,148]

A variety of preparation routes for nanocomposites based on GAS nanoparticles has been applied, e.g. by co-sputtering or co-evaporation with another source in the low pressure subchamber or by implanting into soft thin films (e.g. polymers).[141,149–151] In order to achieve size selectivity for the deposition of nanoparticles with a narrow size distribution, time-of-flight mass filter and electrostatic quadrupole mass selection has been demonstrated. [150,152–155] In order to focus the nanoparticle beam and at the same time achieve certain size selectivity, the single orifice can be replaced by a series of orifices arranged at certain distances. In such aerodynamic lens system, larger particles cannot follow the gas flow through the subsequent orifices due to their high inertia. Accordingly, only nanoparticles below a certain size are concentrated around the centre axis through the orifices and form a focussed nanoparticle beam.[156,157]

Although the theoretical and experimental framework of the nanoparticle growth mechanisms is continually expanded, the underlying processes in nanoparticle formation inside the GAS are not fully understood as by now. In contrast to the common belief of nanoparticles growing throughout the whole transport from the point of nucleation towards the orifice, recent studies found indications of trapping of nanoparticles inside the GAS and fully grown nanoparticles were observed very close to the target.[158]

3. Methods: Deposition and Characterisation

In the context of the development of memsensors, the fabrication and characterization of thin film devices for sensing and memristive switching is a substantial part of this thesis. Due to its versatility, high purity and good process control, the physical vapour deposition process of magnetron sputtering was applied for the preparation of thin films and nanocomposites. This section serves to give a comprehensive overview over the methods commonly applied in the context of this work.

3.1 Deposition of Nanocomposites for Memristive Switching and Sensing Applications

The fabrication of nanoparticle-based memristive devices as well as metal oxide thin film sensors was realised by physical vapour deposition (PVD) processes in a custom-build high vacuum (HV) deposition system. A schematic cross section of the deposition system with its most important components is depicted in Figure 19. In order to allow for the deposition of nanocomposites with multiple components without breaking the vacuum, the deposition system was equipped with four individual planar DC magnetron sources (Thin Film Consulting, two inch, ION'X-2UHV) under normal incidence to a rotatable sample holder. While three magnetron sources were connected directly to the main recipient, one source was mounted inside a custom-built Haberland type gas aggregation source (GAS). Rotation of the sample holder as well as the shutter in front of the GAS was controlled by a programmable microcontroller (Arduino Due) and a wide-angle servo (DF Robot, DSS-M15S).

Two DC power sources (Advanced Energy, MDX 500) were used to allow for simultaneous operation of two magnetron sources. For reactive sputtering from metallic targets, the DC power was pulsed using a high power MOSFET (Behlke Power Electronics, HTS 31 CF I), which was triggered by a frequency generator (PeakTech, DDS Function Generator 4025, rectangular 0-5 V signal).

High vacuum conditions were generated by using a turbo molecular pump (Pfeiffer Vacuum, TMU 262) combined with a dry scroll pump (Agilent Technologies, SH-110). In order to achieve a controlled gas atmosphere during sputter deposition, a flow of Ar (purity 99.999%) as process gas was subjected to the vacuum system over the magnetron inside the GAS using a gas regulating valve (Pfeiffer, EVR116 with attached hot ion cathode IMR 285). For reactive sputtering, O_2 (purity 99.999%) as a reactive gas was introduced by a mass flow controller (Alicat, H-MC-100SCCM-D / 5M) through the respective magnetron source attached at main recipient. Prior to every deposition process, the main recipient was evacuated to 10^{-4} Pa and target cleaning and the conditioning of the deposition process were performed for sufficient time to reach stable deposition conditions (at least for 30 s). Subsequently the sample stage was rotated in order to face the respective source, the shutter was opened and the deposition process performed.

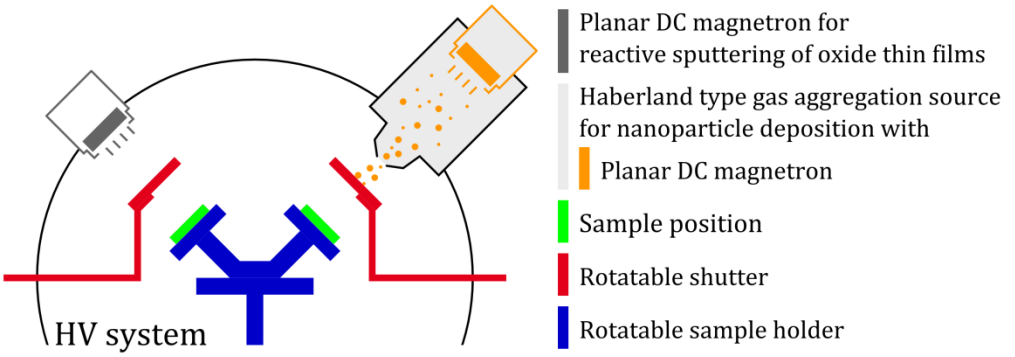

Figure 19: Schematic depiction of a cross sectional cut through the high vacuum magnetron sputtering deposition system for the fabrication of memristive and sensitive nanocomposites. The system involves three planar magnetrons mounted directly to the main recipient as well as an in-house Haberland type GAS. Deposition is performed under normal incidence to the sample surface. The deliberate rotation of sample holder allows for well-defined sequential deposition from each source.

In the following sections, the general procedure for the deposition of nanoparticles as well as dielectric SiO_2 matrix and semiconducting metal oxide thin films is described.

3.1.1 Nanoparticle Deposition

The deposition of noble metal nanoparticles was realised by a gas phase synthesis approach using unipolar DC magnetron sputtering and an in-house GAS. The GAS was separated from the main recipient by an orifice of 2 mm diameter at a distance of 90 mm from sample position. During a typical deposition at an argon flow of 48 SCCM, the pressure inside the GAS was around 190 Pa while the pressure inside the main recipient was around 1 Pa. In the framework of this thesis, pure metal and binary metal alloy nanoparticles consisting of Ag, Au and Pt have been prepared. For the deposition of pure Ag or Au nanoparticles, a planar two-inch Ag (Kurt J. Lesker, 99.99 %, 5 cm diameter) or Au target (Alfa Aesar, 99.99 %, 50.8 mm diameter) was used respectively. For the deposition of noble metal alloy nanoparticles from the system AgAu and AgPt, a single target deposition process was developed in this work, which relies on segmented targets on the basis of Ag targets (Kurt J. Lesker, 99.99 %, 5 cm diameter) with Au (Alfa Aesar, 1.0 mm dia, 99.95%) or Pt (Alfa Aesar, 1.0 mm dia, 99.95%) wires embedded concentrically in the racetrack.[149]

3.1.2 SiO_2 Matrix Deposition

For the preparation of memristive stacks, the dielectric SiO_2 matrix was deposited by pulsed DC reactive magnetron sputtering, either directly onto the conductive Pt or Au surface of the substrate or onto an intermediate Cr wetting layer. For the deposition of SiO_2, a Si target (Goodfellow GmbH, 99.999 %, 50.8 mm diameter) was mounted to the magnetron source at a distance of 70 mm from the sample position and sputtering was performed in a reactive O_2/Ar atmosphere in a pulsed DC mode (typically 80 W, 80 kHz, 35 % duty cycle).

3.1.3 Metal Oxide Nanostructure Deposition

Similar to the deposition of the dielectric SiO_2 matrix for the memristive nanocomposites, CuO and TiO_2 thin films were deposited by pulsed DC reactive magnetron sputtering in a reactive O_2/Ar gas atmosphere. The respective target (Ti: Goodfellow GmbH, 99.99 %, 50 mm diameter, Cu: Kurt J Lesker, 99.999 %, 50 mm diameter) was mounted at a distance of 110 mm from the sample position. Typical power pulsing parameters were 90 W, 50 kHz, 55 % duty cycle in case of TiO_2 and 80 W, 80 kHz, 35 % duty cycle in case of CuO.

The deposition of TiO_2 nanostructured thin films was partially performed in a second, similar deposition system with comparable geometry.[159] The distance between the target and the substrate was modified to 50 mm. For the post deposition heat treatment of the TiO_2 thin films a furnace (Nabertherm, LE 4/11/R6) with ambient air was used.

3.2 Characterisation

The analysis of thin films with respect to their optical, electrical, mechanical, structural, chemical and morphological properties requires the application of a broad variety of characterisation techniques. In this section, the main characterisation techniques applied in the context of this thesis are introduced and their applicability for studies on memristive and sensitive devices will be motivated. Details of the underlying theory for the respective characterisation technique and the corresponding instrumental setup are not discussed here. Instead, references to relevant and comprehensive literature covering further details on each characterisation method will be given in the respective section.

3.2.1 Probing with Photon Beams

The thin films were characterised regarding the identification of fingerprints of TiO_2 and CuO polymorphs using a Raman spectrometer (WITec Wissenschaftliche Instrumente und Technologie GmbH, alpha300RA). For this purpose, the samples were examined by a Nd:YAG laser (λ_{ex}= 532.2 nm) and each spectrum was recorded with 10 accumulations at an integration time of 0.5 s.

X-ray photoelectron spectroscopy (XPS) was applied as a versatile technique for the surface sensitive investigation of the composition of a material as well as its chemical state (e.g. oxidation state). In a typical XPS analysis, the sample is introduced into an ultra high vacuum (UHV) system and subjected to a beam of x-ray photons (typically Al Kα with 1486 eV). In this thesis, XPS (Omicron Nano-Technology GmbH, Al-anode, 240W) studies on the chemical composition of alloy nanoparticles as well as the oxidation state of oxide thin films have been performed. During XPS analysis, the base pressure in the main chamber was in the range of 10^{-7} Pa. The C-1s line of advantageous carbon at 285.0 eV was applied as a reference to correct the charging in all recorded spectra respectively by using the software "CasaXPS" (version 2.3.16).

3.2.2 Probing with Electron Beams

Electron beam related techniques such as scanning electron microscopy (SEM) and transmission electron microscopy (TEM) allow for a detailed investigation of thin films with respect to their structural and morphological features down to the nanoscale. These electron microscopy techniques were frequently applied to characterise the metal and metal alloy nanoparticles, the memristive nanoparticle-based devices as well as the thin film sensors prepared in this thesis.

SEM (Zeiss, Supra 55VP) was applied to study the morphology of semiconducting metal oxide nanostructures (deposited onto silicon wafer pieces, 1 x 1 cm^2, (100) oriented, SiMat) in cross-section and top view. For cross-sectional configuration, the samples were manually broken in half. Alongside SEM analysis on nanoparticle-based memristive devices, chemical information on the long-term stability measurements of memristive devices with additional Cr wetting layer were recorded by energy dispersive X-ray analysis (Oxford Instruments, x-act).

Transmission electron microscopy (TEM) analysis was conducted using a FEI Tecnai F30 STwin microscope (300 kV, field emission gun (FEG) cathode, spherical aberration coefficient Cs = 1.2 mm). Micrographs of AgAu and AgPt nanoparticles on carbon film copper TEM grids (Plano, S160-4) were recorded in bright field mode. Scanning TEM (STEM) tomography measurements were performed using a JEOL microscope (JEM2100). All TEM related studies were performed by Julian Strobel at the chair for Synthesis and Real Structure of Prof. L. Kienle (CAU Kiel, Faculty of Engineering).

For a general introduction into the matter of electron beam related techniques such as SEM, TEM and EDX the reader is referred to the textbook of Fuchs, Oppholzer & Rehme. [160] A detailed treatment of TEM analysis is given in the book of Barry and Carter.[161]

3.2.3 Electrical Characterisation

The electrical characterization of the memristive devices as well as sensors was a substantial part of this thesis. Especially in the context of the developed nanoparticle-based memristive devices, the nanoscopic size of the individual nanoparticles (roughly 10 nm diameter) as well as the nanoscopic layer thickness of the dielectric SiO_2 matrix (in the range of a few nm) imposed strong experimental challenges on a reliable electrical characterisation.

Two main approaches were pursued with respect to the electrical characterisation of nanoparticle-based memristive switching. On the one hand, atomic force microscopy (AFM, Bruker, Dimension 5000) using a conductive tip (Bruker, Si_3N_4 with 20 nm Pt coating) was performed for the selective contacting of individual nanoparticles in a single memristive stack. In order to avoid damaging of the tip, the overall current was limited by a serial resistor (typically 1 GΩ). While the tip acted as the top electrode, a continuous conductive layer was used as back electrode. This setup is schematically shown in Figure 20 a. The memristive switching effect in individual nanoparticles was characterised by recording hysteresis loops via applying voltage ramps and recording the respective current (source meter Keithley 2643

or built-in c-AFM preamp). In addition to the determination of the electrical behaviour, the method of AFM was also applied to record topographical information from the nanoparticle layers. All AFM related studies were performed by Dr. Abdou Hassanien at the Department of Condensed Matter at Jozef Stefan Institute, Ljubljana, Slovenia.

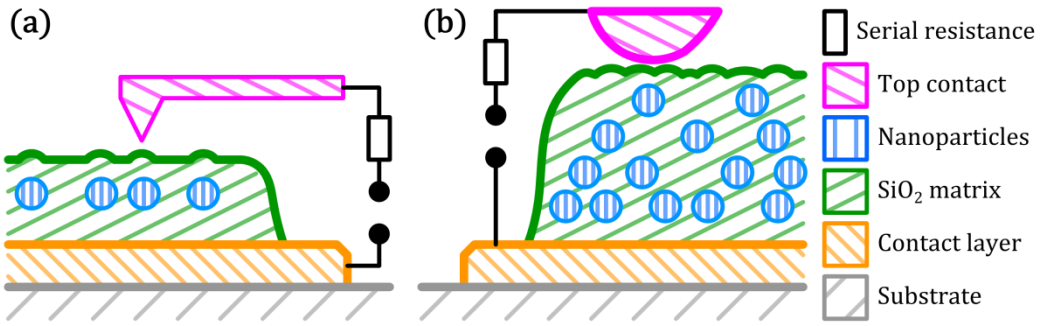

Figure 20: Schematic depiction of electrical characterization of a single SiO_2/NP/SiO_2 stack via c-AFM (a) and multistack nanoparticle-based memristive devices (b) by two point probe station. In case of the c-AFM studies, a serial resistance (typically 1 GΩ) is applied to limit the overall current in order to prevent damage from the conductive tip. For congruency, a similar serial resistance (typically 1 MΩ) is also applied in the measurement of multistack devices.

In addition to the electrical characterization on the nanoscale by contacting individual nanoparticles, the approach was transferred to conventional two point measurement on a four point probe station (Signatone, H150W). For a reliable electrical characterization, the single nanoparticle stack investigated by AFM was replaced by a multistack, prepared by sequential deposition of layers of nanoparticles and SiO_2 matrix. The cross section of an exemplary multistack nanoparticle-based memristive device is schematically depicted in Figure 20 b. The transition towards multiple stacks greatly reduced the probability of short circuiting the memristive stack by defects or pin holes in the nanoscopic layer, which was a common problem evolving from the transition of a nanoscale to a microscale top contact.

The electrical characterization of the multistack memristive devices was performed using a source meter (Keithley, 2400 Source Measure Unit) and a four point probe station. The common contact layer was contacted with a conventional tungsten tip (Signatone, SE-T) as a back electrode. For the top contact to the nanoparticle stack, such rigid tip is not appropriate due to the potential damaging of the nanoscopic stack upon mechanical contact. In order to avoid damaging of the multistack device, a soft contact to the top of the memristive stack was established by using a flexible PtRh wire (Alfa Aesar, 13 wt% Rh, 127 µm diameter) as a top contact. In analogy to the AFM setup, involving a serial resistance for all measurements, the PtRh wire was connected to a serial resistance in order to achieve comparable measurement conditions. The characterization by PtRh wire instead of conducting AFM tip allowed for higher currents, so that the series resistance was chosen to be 1 MΩ. To measure the switching characteristics, DC voltage sweeps were applied with the top contact biased and the common back electrode grounded. No current compliance was set by the source measure unit, as the serial resistance provides current limitation and suppresses overshoot effects.

Alongside the development of deposition processes for nanostructured thin films of semiconducting metal oxides, the applicability of these thin films in the context of sensing was studied by UV- and gas sensing measurements.

For the measurement of the UV-illumination dependent resistance of ZnO microrods, the measurement stage applied for the electrical characterisation of the multistack memristive devices was modified by adding a pulsing unit for UV light. The ZnO microrods were contacted to two planar gold contacts using Acheson 1415 silver and placed under a UV LED (369.7 nm peak) inside metal case providing full shielding of ambient light. Pulsing of the UV illumination was realised over a programmable microcontroller (Arduino Uno) and PWM control of the LED constant power source (Meanwell LDD500).

Further measurements on the sensing response of ZnO, TiO_2 and CuO nanostructured thin films towards UV-light and gases such as H_2 or volatile organic compounds (VOCs) were performed in close collaboration with Dr. Oleg Lupan by the group of Prof. Ion Tiginyanu and Dr. Oleg Lupan at Technical University of Moldova. Details on the measurement procedure are explained in the respective publications.[125,159]

4. Results and Discussion

Within this thesis, the following fundamental questions concerning the design, fabrication and application of memsensors will be addressed:

1. Which memristive and sensitive devices are suitable as building blocks for the design of memsensor devices?
2. How can memristive switching and sensing be combined in memsensors in order to achieve emerging properties?
3. How do these properties relate to properties observed in biological neuron assemblies?

For an adequate answer to these questions, memristive devices and sensor devices were prepared and investigated in the framework of this work and the concept of memsensors combining the fundamental properties is explored by modelling of memsensor devices:

In the context of memristive switching, the main concept of field-driven metal cation migration was pursued and expanded by fabricating and characterizing a memristive device relying on noble metal alloy nanoparticles embedded in an insulating SiO_2 matrix, which is described in detail in section 4.1.

The aspect of sensing of UV-light and gas molecules is covered in section 4.2. Nanostructured thin films of semiconducting metal oxides have been prepared and characterised regarding their sensing performance. Furthermore, the effect of surface decoration of the thin films by metallic nanoparticles on the sensing properties is studied.

In order to elucidate the questions regarding memsensor properties, memsensors are modelled and fingerprints of emerging properties with their relation to neuromorphic engineering are discussed in section 4.3. For this purpose, on the one hand a memsensor model involving the electrical characteristics of the previously described memristive and sensor devices is established. On the other hand, a general memsensor model for the realization of amplitude adaptation is discussed.

Before going into details on the respective topics, the reasoning behind the choice of materials for the development of memristive and sensitive thin film devices will be motivated. Among the variety of concepts and materials proposed for the realization of memristive switching and sensing, any combination of materials involves particular advantages and challenges. First, the reasoning behind the nanoparticle-based memristive devices as well as the potential prospects of such devices are discussed. In order to provide an overview on how the nanoparticle-based memristive device relates to the multitude of memristive devices reported in literature, in Figure 21 the individual features of this device are categorised.

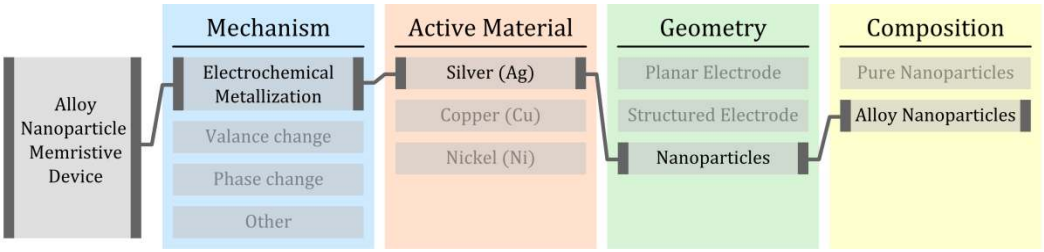

Figure 21: Schematic depiction of the reasoning and categorization of the nanoparticle based memristive device as developed in the framework of this thesis.

The memristive devices investigated in this work are based on the switching mechanism of electrochemical metallization, namely the reversible oxidation, migration and reduction of metallic cations in an electrical field. This mechanism was chosen as a basis for the fabrication of memristive devices, as it exhibits several benefits over other mechanisms for memristive switching:

- In addition to a high number of experimental reports of working memristive devices based on metal cation movement, a consistent theoretical framework on the underlying processes is already established.
- The high resistive state is mainly determined by the resistivity of the dielectric layer. An adequate choice of the device geometry and the dielectric allows tailoring the resistance, which is particularly interesting in the context of low power operation.
- Alongside a multitude of reports on binary filamentary switching, also diffusive switching characteristics[162] and multilevel analog switching characteristics have been reported[7] for metal cation based memristive devices, indicating the high versatility of this approach.

In the context of ECM devices, commonly Ag and Cu (and very occasionally also Ni) are applied as mobile metal cations. In the framework of this thesis, Ag was chosen as active element for the development of memristive devices, because Ag is more noble than Cu, which results in a lower tendency to oxidize. In addition, Ag exhibits one common oxidation state (Ag^{+}) instead of different possible oxidation states in case of copper (namely Cu^{+} and Cu^{2+}).

The majority of experimentally realised ECM memristive devices rely on an arrangement of planar electrodes. In this case, the bulk of the Ag electrode acts as an (almost) infinite source of mobile cations. The transition from planar electrode to metallic NPs as origin of the mobile silver cations offers additional advantages:

- Memristive devices with nanostructured bulk electrodes (nanocones) are reported to exhibit enhanced stability and repeatability of the memristive switching with a well-defined hysteresis loop. This is allocated to the enhancement of the electrical field due the low radius of curvature (tip) of the cones, which is in line with the effect expected for the application of NPs.
- One commonly reported drawback in ECM memristive devices is the necessity of an electroforming step. In this electroforming step, initial filaments are formed,

effectively reducing the distance between the electrodes and enabling reliable memristive switching for subsequent cycles. However, this initial step involves the application of higher voltages, which imposes an additional challenge for large scale integration. For the development of devices without the necessity of electroforming, the application of NPs offers the potential advantage, that the distance between the NPs and the electrodes can be adjusted by deliberate choice of deposition parameters, e.g. to form a gradient of NPs inside the matrix, making a later electroforming step obsolete.

In conventional ECM memristive devices, the active electrode typically comprises of pure Ag. When it comes to the composition, especially in the context of the incorporation of NPs in the dielectric matrix, the application of alloys instead of pure Ag appears very promising, as it offers many benefits:

- For bulk electrodes in memristive devices relying on a Ag(Au)/SiO_2/TiN thin film stack a significant enhancement in the electrical characteristics was reported: Upon the transition from a pure Ag to an alloy AgAu active electrode, the necessary electroforming voltages were reduced by a factor of 2.8, accompanied by faster switching operation and more well-defined resistance states.[72] In their original explanation, the modifications in the electrical properties of the Ag(Au)/SiO_2/TiN memristive devices are attributed to the galvanic effect, i.e. the presence of a more noble metal (Au) favours the oxidation of less noble metal (Ag), leading to easier ionisation and transport of silver cations. However, in a continuous alloy electrode the chemical potential of both elements is expected to align, which renders a galvanic effect unlikely, and for entropic reasons (entropy of mixing) the release of the less noble component may be additionally impeded. On the background of these considerations, an alternative explanation for the enhancement in memristive switching properties appears more likely: As the active electrode is in contact with an oxide thin film (e.g. SiO_2), the presence of oxygen may lead to the formation of a passivation layer on the active electrode. Upon alloying with Au, the AgAu electrode becomes more noble and the tendency to form the passivation layer and consequently its influence is decreased, which would yield an easier ionisation and transport of silver cations and is in line with the observations from Kuo et al., who reported a stronger enhancement for $Ag_{30}Au_{70}$ compared to $Ag_{70}Au_{30}$ active electrode.[72]
  Irrespective of the underlying mechanism, judging from the experimental results on Ag(Au)/SiO_2/TiN memristive devices, the incorporation of noble metal alloys with defined compositions exhibits a stunning potential to tailor the switching characteristics of a nanoparticle-based memristive device even without any changes in the geometry.

- As the NPs act as source for the release and transport of mobile silver cations, in case of alloy NPs with a more noble metal, the latter component is thought to retain its position inside the dielectric matrix. Thus, the NP would release Ag and enrich in the more noble component, while remaining as a stable anchor, which indicates a potentially beneficial effect on the reproducibility of memristive switching. To the best of my knowledge, this approach has never been pursued in the context of memristive switching.
- In addition, a deliberate tailoring of the composition of the NPs will allow controlling the amount of mobile species that can be released from the NPs. By this approach the formation of filaments could efficiently be suppressed in order to influence the low resistance state of the memristive device.

In a close cooperation, the concept of nanoparticle-based memristive devices was incorporated into a KMC simulation by Dr. Sven Dirkmann (Group of Prof. T. Mussenbrock, Ruhr Universität Bochum, Germany), who already successfully studied ECM devices relying on silver cation migration and planar electrodes by a similar simulation approach.[51,163] The results from the simulation of NP gradients in a 2D environment are shown in Figure 22. For pure Ag NPs (Figure 22 a), after memristive switching the initial NPs have changed their shape and position and are merged together. In case of adding immobile atoms to the NPs (Figure 22 b), the initial morphology of the stack is preserved to a greater extent after the memristive switching. In the first case, the benefits from using NPs could easily vanish after multiple cycles, as the initially defined geometry is not retained. This implies a certain limitation on the usability of pure Ag NPs (e.g. as described by Jo et al.[7]) in the context of nanoparticle-based memristive devices with respect to the long-term stability. Thus, for a precise tailoring of switching properties, the usage of noble metal alloy NPs with a stable, more noble component, seems highly beneficial.

The decision to use alloy NPs with silver cations as mobile component imposes certain limitations on the choice of materials for the stable, more noble component. More precisely, Au and Pt remain as the only viable elements for preparation of alloy NPs considering the abovementioned restrictions. In order to visualise the selection of materials investigated in the framework of this thesis, the respective elements are summarised in Figure 23. Accordingly, silver as the mobile component is depicted with green background and Au and Pt, serving as stable component of the alloy NPs, are highlighted with blue background.

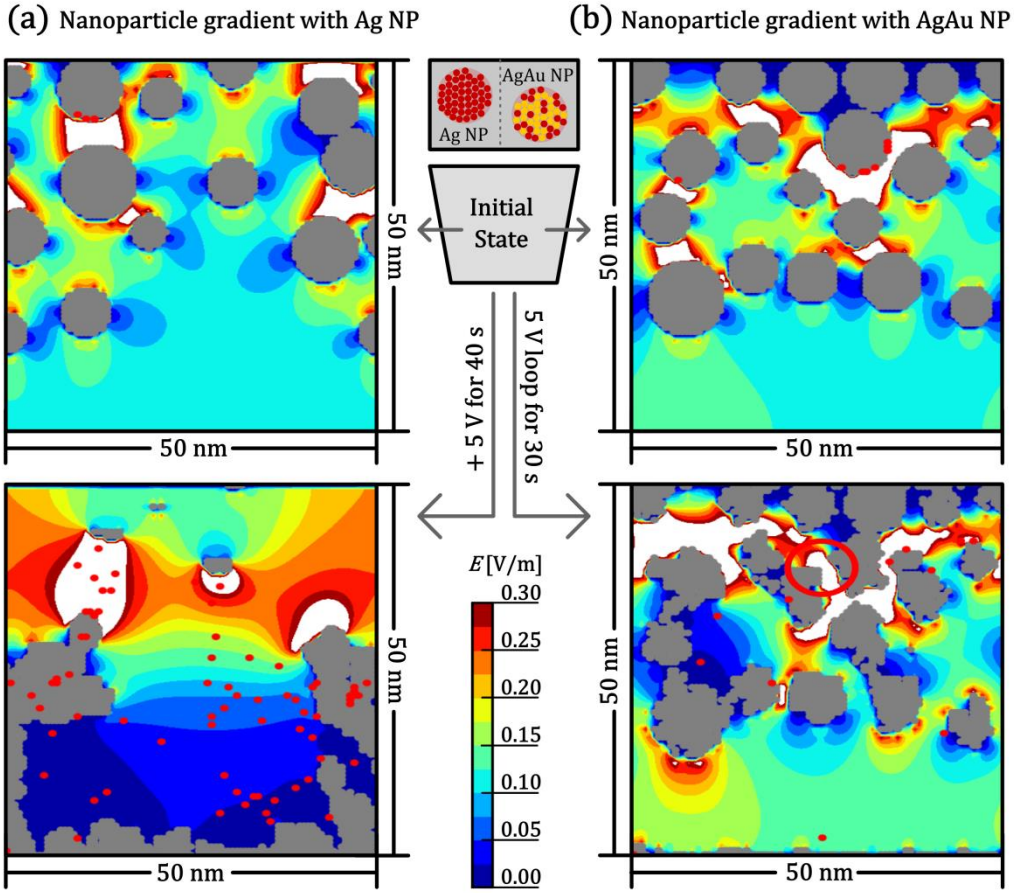

Figure 22: Kinetic Monte-Carlo simulations of silver cation migration in nanoparticle-based memristive devices relying on Ag NPs (a) and AgAu NPs (b). For both cases, the 2D simulation box was chosen to be 50 nm x 50 nm. The local electrical field is displayed using a colour code. In the initial state (top row), the NPs (grey circles) are randomly distributed in the dielectric matrix with a density gradient from the bottom to top. Due to the nanoscopic distance between the NPs and their small radius of curvature, the local electrical field is considerably increased (white areas correspond to E > 0.3 V/nm). Due to the migration of mobile silver cations (red dots) during the simulation, the shape and arrangement of the NPs changes (bottom row). While in case of AgAu NPs the original configuration is roughly retained after a hysteresis loop, in case of pure Ag NPs the initial distribution has largely vanished. The KMC simulations were performed by Dr. Sven Dirkmann, who also provided the displayed 2D simulation images.[51]

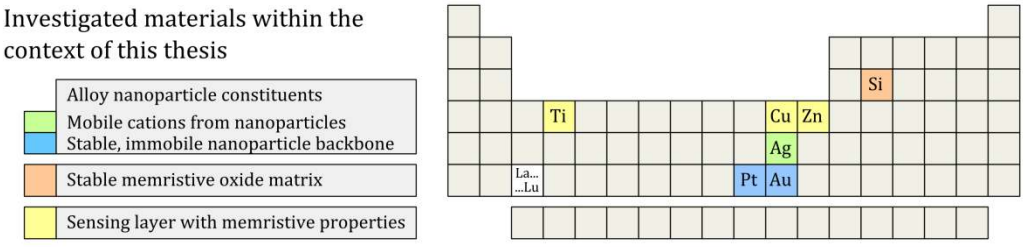

Figure 23: Representation of the chosen materials for closer investigation in the context of a possible memsensor realisation. Alloy nanoparticles featuring silver (Ag, green) as a mobile component and gold or platinum (Au/Pt, blue) as a stable component. For the preparation of memristive devices, the nanoparticles are embedded in SiO_2 (orange) as a dielectric matrix. For the realization of the sensitive part, semiconducting oxides from transition metals (Ti/Cu/Zn, yellow) are investigated.

Having decided on the application of alloy NPs of the system AgAu or AgPt, the second component necessary to design a memristive device is an appropriate dielectric matrix. Among the variety of matrix materials commonly reported for ECM memristive devices, oxide materials are most frequently applied and will also be used in the framework of this thesis. However, in oxide materials, the distinction between metal cation and oxygen vacancy mediated memristive switching may turn out to be difficult. This is illustrated by the example of TiO_2, which is applied in the context of memristive devices relying on VCM (migration of oxygen vacancies) as well as ECM (migration of metal cation) mechanism. Due to the nanoscopic dimensions of typical devices and the resulting challenges regarding direct observations of the underlying mechanism, predictions on the dominating mechanism in a particular device render challenging. In order to avoid such ambiguities, the selection of potential oxide matrix materials is limited to stable oxide materials with a large band gap. On the background of these requirements, SiO_2 and Al_2O_3 appear as promising oxide materials. For the development of nanoparticle-based memristive devices, in this thesis the focus lies on SiO_2 as dielectric matrix (Figure 23, orange background).

For the preparation of a sensing layer in the context of a memsensor, semiconducting metal oxides are especially interesting, as common materials such as TiO_2 are used for sensing as well as for memristive switching based on the migration of oxygen vacancies. Therefore, these materials offer the potential of combining memristive as well as sensitive properties in a single device. Thus, in this work the investigation on sensing is limited to oxide thin films of the broadly available semiconducting metal oxides ZnO, TiO_2 and CuO (Figure 23, yellow background). For a tailoring of the sensitive properties, semiconducting metal oxide materials are commonly applied as micro- or nanostructures, enhancing the overall surface area. Furthermore, the application of metallic NPs to the sensor surface is an additional pathway to adjust the sensing properties. As NPs are also an essential part of the memristive devices studied in the framework of this thesis, the route of surface decoration of the sensor devices appears to be a promising synergy.

In terms of the fabrication of the memristive devices and sensors for an application in the field of memsensors, ideally the whole manufacturing process can be integrated into a single process with high reproducibility, purity and control over the stoichiometry of the thin films. Following this idea and building on the experience in physical vapour deposition (PVD) methods at the Chair of Multicomponent Materials, the devices in the context of this thesis are prepared by magnetron sputtering, as this method is applicable for the deposition of metal contacts as well as nanostructured oxide thin films (in terms of pulsed DC reactive magnetron sputtering) and nanoparticles (in terms of gas phase synthesis in a Haberland type gas aggregation source).

4.1 Memristive Switching based on Individual Noble Metal Nanoparticles

This section is devoted to the fabrication of nanoparticle-based memristive devices as well as the detailed description and thorough characterization of the related memristive switching phenomena. The devices typically consist of noble metal NPs, which are embedded in a dielectric SiO_2 matrix. In Figure 24, the cross section of nanoparticle-based memristive devices (in this example consisting of 3 layers of NPs) is schematically depicted. For a better readability, rough estimates of common layer thicknesses are included in the schematic drawing.

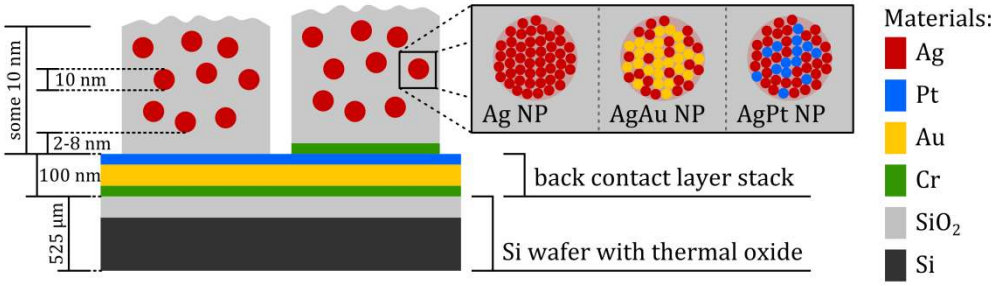

Figure 24: Schematic depiction of a cross section through nanoparticle-based memristive devices as fabricated and characterised in the framework of this thesis. As the schematic drawing of the individual layers is not to scale, the approximate dimensions of the characteristic features are indicated in the drawing.

The NP/SiO_2 layer is deposited onto a common back electrode layer. For this purpose, silicon wafer pieces with 500 nm thermal oxide were choses as substrates, onto which a Cr-Au-Pt stack is applied as a metallic conducting base layer. Choosing these substrates granted a low roughness for the subsequent deposition of the NP/SiO_2 layers. In the framework of this thesis, memristive devices relying on single layers as well as multiple stacks of NPs were investigated:

- The memristive switching properties of individual noble metal alloy NPs in a single SiO_2/NP/SiO_2 stack with and without Cr as wetting layer are studied via AFM measurements involving a conductive tip (section 4.1.3).
- The insights from these investigations on single NPs are related to the development of memristive devices relying on multiple stacks (section 4.1.4). For this purpose, multistack devices with five layers of AgAu NPs and AgPt NPs were fabricated and analysed by two-point electrical measurements using macroscopic tips.

However, prior to the discussion of the electrical properties of the nanoparticle-based memristive devices, the focus will be put on the characterization and fabrication of its components, namely the dielectric SiO_2 matrix and the alloy NPs. Thus section 4.1.2 covers TEM related studies on the electrical stability of common dielectrics (with a focus on SiO_2) and in section 4.1.1 a novel approach to the Haberland type GAS as a PVD based method for the deposition of alloy NPs with narrow size distribution and controllable alloy composition is described.

4.1.1 Facile Gas Phase Synthesis of Alloy Nanoparticles

Amongst the PVD-based methods for the deposition of NPs, self-organised alloy NP formation by cosputtering[141,142] and coevaporation[143,144] is broadly applied and typically allows for good control over NP composition. However, the NP size and the filling factor are not independent, which limits the use in nanocomposite deposition. To overcome this limitation, particle beam sources such as the magnetron-sputtering-based gas aggregation source (GAS) as initially designed by Haberland[145] can be used. While this approach in combination with multiple magnetrons is typically well suited for alloy NP deposition, single magnetron sources are commonly not applicable for the deposition of alloy NPs with variable composition.[148,164] In order to reduce the experimental effort of using multiple magnetron sources in a single GAS simultaneously, in this thesis a GAS with a single magnetron was chosen.

The common limitation of fixed composition of the deposited alloy NPs using a single magnetron was overcome by introducing a novel segmented target geometry. Instead of a plain monometallic target, a segmented two component target was used, which consists of a commercial 2-inch target in which concentric rings of the more precious materials (Au, Pt) are embossed. The target geometry is depicted schematically as well as in terms of top view photographic images in Figure 25 at the example of an AgAu and AgPt target. This novel approach allows for deposition of binary alloy nanoparticles with variable composition by a variation of the pressure inside the GAS during operation.

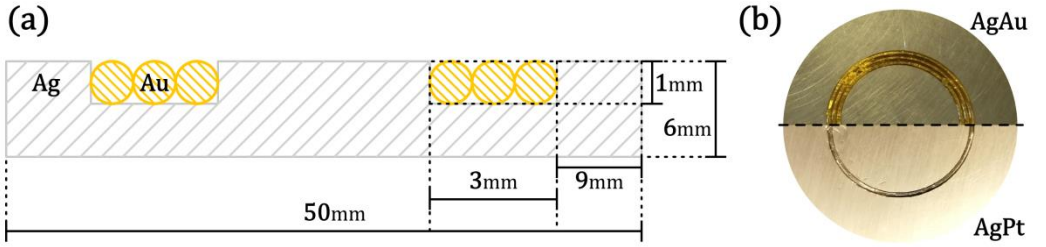

Figure 25: (a) Schematic cross section drawing of the custom-built target; (b) Photographic images of a AgAu (top) and AgPt (bottom) target.

A detailed description of this novel approach on NP deposition from gas phase synthesis at the example of AgAu alloy NPs with adjustable composition is published in the following work:

> **A. Vahl**, J. Strobel, W. Reichstein, O. Polonskyi, T. Strunskus, L. Kienle, F. Faupel, *Single target sputter deposition of alloy nanoparticles with adjustable composition via a gas aggregation cluster source*, Nanotechnology. 28 (2017) 175703. doi:10.1088/1361-6528/aa66ef.

The segmented target approach with concentric rings of Au or Pt in a Ag target was implemented successfully for the fabrication of alloy NPs of the systems AgAu and AgPt. TEM bright field micrographs of the respective AgAu and AgPt NPs are depicted in Figure 26 a. In both cases, the NPs exhibit a narrow size distribution with the mean diameter of

AgAu NPs being roughly 12 nm. In comparison, the AgPt NPs are smaller with a mean diameter of roughly 7 nm. However, in case of AgPt NPs also a second population of NPs with a diameter of roughly 2 nm is observed, which typically makes up a fraction below 15 % of the total number of observed NPs. Although the general operational parameters during deposition were identical for the AgAu NP and AgPt NP deposition, the observation of different mean diameters of the deposited NPs is not unexpected. The processes inside the GAS are highly complex and even slight changes to the GAS deposition process (such as the installation of a new target) can impact the nucleation, growth and coagulation process, resulting in deviations in the NP diameter. In case of the applied segmented target for AgAu and AgPt, the geometry of the targets is different (with the AgPt target using a single concentric Pt wire embedded in the target instead of three wires in case of AgAu). Furthermore, the sputter yields differ for Ag, Au and Pt, which results in a different number of sputtered atoms in the gas atmosphere, yielding a possible explanation for the observed difference in mean particle diameter for AgAu NPs and AgPt NPs.

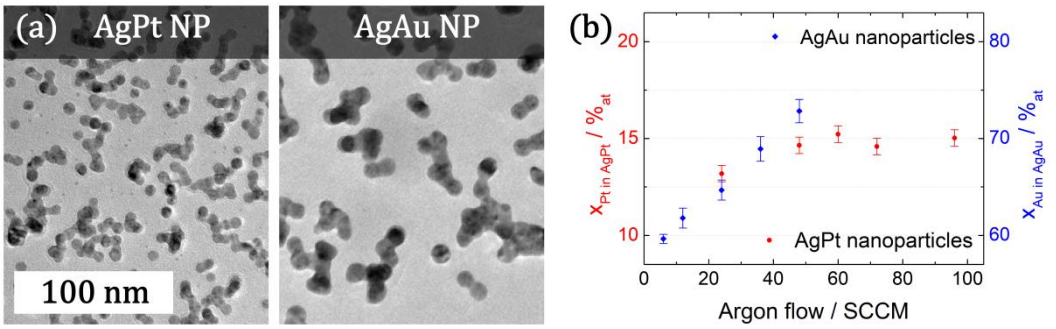

Figure 26: (a) TEM bright field micrographs of AgPt and AgAu nanoparticles (recorded by Julian Strobel); (b) The nanoparticle composition changes with the argon flow applied to the GAS.

Despite these minor deviations in diameter, both, the AgAu NPs as well as the AgPt NPs, render very useful for an application in nanoparticle-based memristive devices, as their mean diameter is reasonable large to allow easy identification of the NP position in case of contacting by AFM. In addition, the nanoscopic mean diameter of the NPs relates to some ten thousand atoms in an individual NP (as a rough estimate: a pure Ag NP with 10 nm diameter contains roughly 20000 atoms), which in reasonable in the context of limiting the amount of mobile silver atoms that can be released from the alloy NPs.

The main benefit of using a segmented target with concentric Au or Pt wires over conventional planar alloy targets is the following: By varying the operational pressure inside the GAS due to a deliberate choice of the argon flow, the composition of alloy NPs can be varied within a considerable range while simultaneously keeping the NP mean diameter almost constant. The NP composition was investigated by XPS as well as TEM EDX, which also confirmed the alloy nature of the NPs. In Figure 26 b, the mole fraction of the noble component in the deposited NPs as studied by XPS is shown. In case of the AgAu target, the composition of the NPs can be tailored over a broad range from an atomic concentration of Au between 60 % and 75 %. Here, a lower argon flow applied to the GAS results in a lower mole fraction of Au in the AgAu NPs. This trend is attributed to a pressure related change in the sputter trench width. At higher pressure (due to higher Ar flow), the trench is focussed

narrower on the centre of the racetrack, where the Au wires are embedded, leading to a higher concentration of the more noble component. For lower pressures, the trench widens, which allows a higher fraction of silver atoms to be integrated into the growing NPs. In case of the AgPt target the change in composition is not as prominent, which is in line with this explanation. The AgPt target involves a single concentric Pt wire attached at the centre of the racetrack. Accordingly, the overall area of potential Ag sputtering is wider, leading to a lower Pt content in the deposited NPs. As the Pt wire is placed close to the centre position of the trench, the change in composition is not as strong as in the case of the AgAu target with three Au wires.

Having successfully established this robust approach on the deposition of alloy NPs, the next step towards the fabrication of a nanoparticle-based memristive device is the incorporation of such NPs into a dielectric matrix in a controlled manner. Due to the nanoscopic dimensions of the individual NPs as well as the SiO_2/NP/SiO_2 stacks with overall thicknesses of some ten nm, conventional imaging techniques such as cross-sectional SEM are not well suited to study the distribution of the incorporated NPs. To overcome this limitation, in a close collaboration with Julian Strobel, a sample comprising a NP gradient inside a SiO_2 matrix was prepared by applying multiple subsequent controlled depositions of NP layers and SiO_2 layers. The NP gradient was designed to show the lowest number of NPs close to the interface to the substrate material and gradually increasing the NP concentration towards the sample surface. Applying STEM tomography as depicted in Figure 27, it was possible to capture the lateral distribution of the NPs (yellow) inside the dielectric matrix.

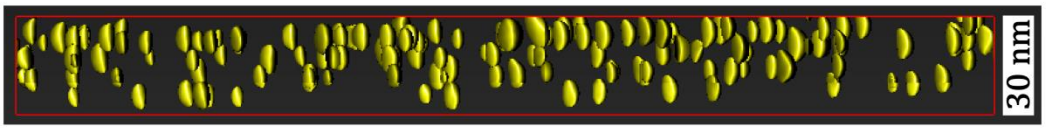

Figure 27: STEM tomography reconstruction of a cross section through a nanoparticle (yellow dots) gradient in a dielectric SiO_2 matrix (transparent). The sample was designed such that the nanoparticle concentration at the bottom of the sample is lowest and gradually increases towards the top. This gradient is well observed in the tomography cross section. The respective STEM data were recorded and analysed for tomographic reconstruction by Julian Strobel.

The targeted geometry of the NP gradient inside the matrix is readily observed in the STEM tomography cross section. The number of NPs at the bottom is least while it steadily increases towards the top. These results from STEM tomography indicate that the applied deposition method of consecutive depositions of SiO_2 and NP layers is capable of preparing thin film nanocomposites with well-defined arrangements of NPs in the dielectric matrix. Before SiO_2/NP/SiO_2 stacks prepared by this method will be discussed in terms of their memristive properties, a brief comment on the stability of SiO_2 as matrix material will be given in the following section.

4.1.2 SiO_2 as Matrix Material for Nanoparticle-based Memristive Switching

As the position and shape of NPs embedded in the dielectric matrix are well observed by TEM, *in situ* studies on the memristive switching and potential filament formation is tempting because it promises the junction of direct imaging and electrical characterisation. Especially in the context of filament formation in ECM memristive devices relying on Ag cation migration, a variety of reports on *in situ* TEM studies is present.[165][65] However, the interpretation of such direct observations asks for special care regarding the following aspects:

- Unlike typical bulk memristive devices, the prerequisite for TEM analysis is the accessibility of the memristive layer with a low thickness in a typical range of some 10 nm. Thus, in addition to the migration of mobile silver cations through the dielectric matrix, the migration at the surface may open up as an additional pathway, making direct correlations with the electrical behaviour observed in bulk memristive devices very challenging.
- In addition, the electron beam itself may impose an impact on the electric properties of the dielectric matrix.

In order to address the latter aspect, different oxide matrix materials (namely TiO_2, Nb_2O_5, SiO_2) have been investigated by TEM with respect to their electrical properties and the impact of different electron doses. These TEM related studies were performed by Krishna Kanth Neelisetty at Karlsruhe Institute of Technology (KIT, Karlsruhe, Germany). The full details on the study on electron beam effects on the electrical and structural properties of oxide thin films are published in the following paper:

> K. K. Neelisetty, X. Mu, S. Gutsch, **A. Vahl**, A. Molinari, F. v. Seggern, M. Hansen, T. Scherer, M. Zacharias, L. Kienle, V. S. K. Chakravadhanula, C. Kübel, *Electron beam effects on oxide thin films – Structure and electrical properties*, Microscopy and Microanalysis. (2019) 1-9. doi:10.1017/S1431927619000175

In short, while the transition metal oxides showed severe changes in their conductivity due to the formation of suboxides even at very conservative electron doses, in SiO_2 the formation of percolating pathways of silicon-rich NPs in the oxide matrix results in a conductivity change at relatively higher electron doses. Apart from the impact of the observed structural and electrical changes on the interpretation of *in situ* TEM studies on memristive switching, these results also indicate that SiO_2 exhibits the highest stability amongst the investigated materials. This underlines the particular eligibility of SiO_2 as a matrix material for development of nanoparticle-based memristive devices. Although SiO_x has recently been reported in the context of memristive switching without mobile metallic cations, it is expected that in the presence of NPs containing Ag species, the ionisation and migration of silver cations will be dominating due to the lower expected activation energy.[166]

4.1.3 Diffusive Memristive Switching based on Individual Noble Metal Nanoparticles

The fundamental building blocks of the nanoparticle-based memristive devices are the individual noble metal alloy NPs. As such, the electrical properties of the individual NP embedded in a single SiO_2/NP/SiO_2 stack are of particular interest. In order to understand the memristive switching mechanism fundamentally on the scale of individual NPs, c-AFM has been used to contact SiO_2/NP/SiO_2 stacks on a common back electrode, because the application of AFM allows for the precise selection and contacting of the location of an individual NP. The data acquisition for the AFM related studies was performed by Dr. Abdou Hassanien.

In the framework of this thesis, a variety of nanoparticle-based memristive stacks with the general sequence SiO_2/NP/SiO_2, featuring different alloy NPs and different SiO_2 thicknesses, has been characterised. A common feature among these devices was the observation of diffusive memristive switching. In this section, the memristive switching properties of AgPt NPs in a SiO_2/AgPt NP/SiO_2 stack are discussed in detail in order to illustrate the diffusive memristive switching behaviour observed in alloy NPs. The underlying device nominally consists of a bottom layer of 8 nm SiO_2, followed by AgPt NPs with a mole fraction of Ag of roughly 0.85 and a diameter of roughly 7 nm and finished by a layer of 2 nm SiO_2 on top. A representative hysteresis loop of a full switching cycle is depicted in Figure 28 a. In the context of the c-AFM measurements, the hysteresis loop was recorded at a low integration time for the measurement of the current. Alongside the low current level (in the range of nA), this results to considerable noise especially in case the device is in its HRS. Accordingly, the raw data were reduced by averaging over adjacent data points with a binning factor of 16.

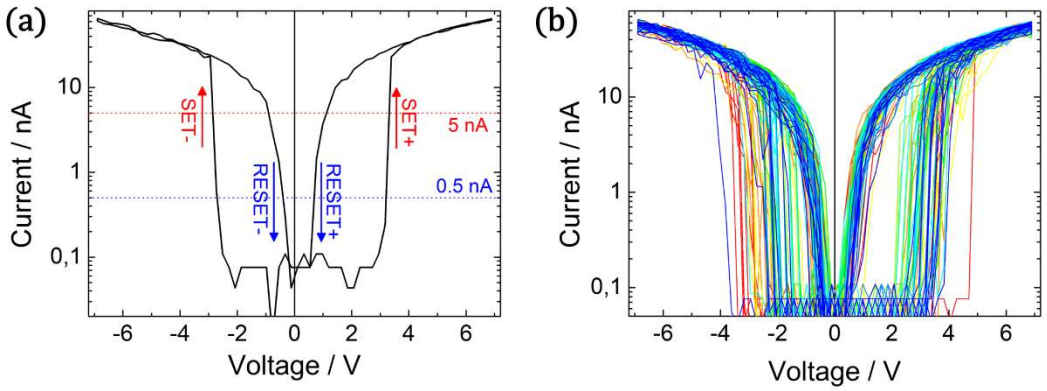

Figure 28: Diffusive memristive switching observed by AFM measurements on an individual AgPt nanoparticle using a conductive tip. In a single hysteresis loop (a) the device shows a SET (switching towards LRS) and RESET (switching towards HRS) event for both, positive and negative polarity. For the reliable determination of the respective switching voltages, the current threshold of 5 nA is selected for a SET and 0.5 nA for a RESET. The comparison of 70 consecutive hysteresis loops (b) implies a certain distribution of the respective switching voltages.

Initially, at zero volts, the NP device is in its HRS, resulting in a current in the order of 100 pA. Upon increasing the voltage to a certain threshold, the device switches to its LRS and the IV curve is mainly dominated by the serial resistance of 101 MΩ (applied in order to limit

the current through the c-AFM tip). The SET voltage in the exemplary hysteresis loop is roughly 3 V. In the nanoparticle-based memristive device, the SET process is expected to be related to the ionization of silver atoms from the alloy NPs and the consecutive migration of silver cations through the SiO_2 matrix. Due to the nanoscopic dimension of the layer thickness of the SiO_2 matrix, even the limited amount of mobile silver species from a single NP allows for the formation of a metallic connection through the dielectric layer, which leads to the switching to the LRS. Upon reducing of the applied voltage, the device remains in the LRS, until a certain threshold voltage is reached and the device switches back into its HRS. In case of the exemplary hysteresis loop, this RESET voltage is located around 1 V. The origin of this RESET step is the following: Due to the serial resistance, in case the memristive device is in its LRS, the potential drop is mainly over the serial resistance. The current flow through the metallic nanoparticle-based connection results in Joule heating and electromigration, resulting in a rupture of the metallic filament. This process is facilitated by the limited amount of mobile silver species, which impacts the formation of the filament. In contrast to a planar silver electrode with an (almost) unlimited supply of mobile silver species, in case of individual NPs as a source for silver cations, the filament cannot grow to the full extent. Such a frustrated filament is expected to dissolve easier than a fully formed filament in case of conventional ECM memristive devices, resulting in the observed diffusive memristive switching. Upon reversing the polarity, the fundamental switching behaviour is preserved and a similar diffusive switching cycle with SET and RESET voltages shifted slightly towards lower voltages is observed. In the following discussion of the statistical evaluation of the switching parameters, the switching voltages at positive polarity are referred to as “SET+” and “RESET+”, while at negative polarity the terms “SET-“ and “RESET-“ are applied.

The IV characteristics for 70 consecutive hysteresis loops are shown in Figure 28 b. Although the general nature of diffusive memristive switching as described above is observed for all 70 cycles, the switching voltages are not identical for every individual switching event but distributed over a certain range. In order to characterise the diffusive memristive switching on the level of an individual NP in a SiO_2/AgPt NP/SiO_2 stack, these 70 cycles are considered for a statistical evaluation of the characteristic switching voltages. For this purpose, the switching voltages were extracted from each hysteresis loop by manual evaluation. The following criteria were applied for the detection of SET and RESET voltages:

- The SET voltage is the voltage at which the current raises above 5 nA.
- The RESET voltage is the voltage at which the current falls below 0.5 nA.

The current threshold values were defined to be separated by 1 order of magnitude to allow for a robust detection of the respective switching event and to minimise any impact of noise. Based on the detected switching voltages, the characteristic features of diffusive memristive switching of the investigated SiO_2/AgPt NP/SiO_2 stack are illustrated as probability plot and histogram in Figure 29. Applying a statistical evaluation, the reduced data including the mean value, standard deviation, median as well as minimum and maximum values for the SET and RESET voltages respectively are compared in Table 1.

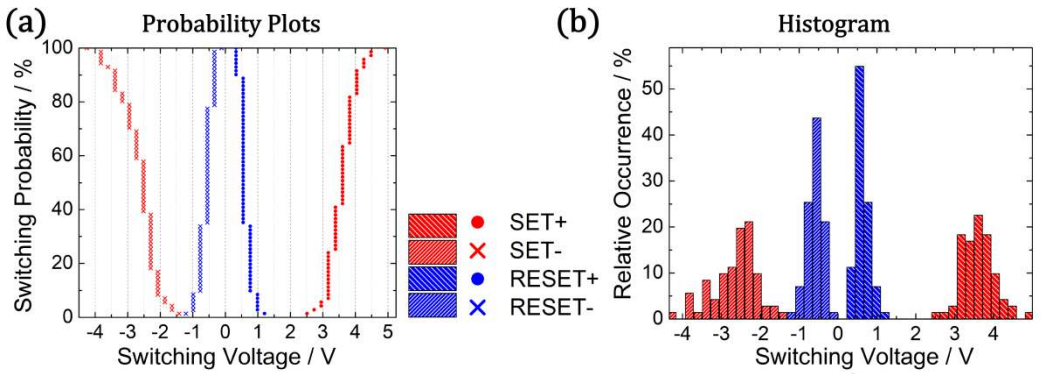

Figure 29: Statistical evaluation of the switching voltages obtained from 70 consecutive hysteresis loops measured for a SiO_2/AgPt NP/SiO_2 stack. The probability plot (a) and histogram (b) shows a general trend of higher SET voltages for positive polarity.

Table 1: Overview over the SET and RESET voltages extracted from 70 consecutive hysteresis loops for a SiO_2/AgPt NP/SiO_2 stack. Mean (average) voltage: V_{mean}; standard deviation: σ; voltage median: V_{med}; minimum and maximum: V_{min} and V_{max}.

	Process	V_{mean}	σ	V_{med}	V_{max}	V_{min}
Positive Polarity	SET+ / V	3.60	0.42	3.61	4.92	2.51
	RESET+ / V	0.62	0.18	0.55	1.21	0.33
Negative Polarity	SET- / V	-2.65	0.57	-2.51	-4.26	-1.42
	RESET- / V	-0.59	0.21	-0.55	-1.21	-0.11

Upon comparing the results from the statistical evaluation, three main conclusions can be extracted:

- As a general trend, the SET+ voltage with its mean value of 3.60 V is shifted to higher voltages compared to the corresponding SET- process at negative polarity with its mean value of -2.65 V. In addition, the distribution of SET+ voltages is narrower with a standard deviation of 0.42 V instead of 0.57 V. The observation of a higher switching voltage for SET+ is in line with the expectation based on the layer thicknesses of the investigated SiO_2/AgPt NP/SiO_2 stack. Nominally, the bottom SiO_2 thin film thickness is 8 nm while the top layer thickness is only 2 nm. Upon applying a positive potential to the conductive AFM tip, the silver cations are brought from the NP through the thicker layer, which correlates with the higher voltage necessary to perform the SET+ process.

- In contrast, the switching voltages for the RESET step at positive and negative polarity are almost symmetrical and exhibit in general a more narrow distribution than the SET voltages. Thus, the RESET occurs at comparable mean voltages of 0.62 V or -0.59 V in the positive and negative branch respectively.

- Especially at positive polarity, there is a clear separation between the SET and RESET voltages. Considering the smallest observed SET+ and the largest observed RESET+ voltage, no switching event is occurring within a window of 1.30 V. In this operation window, the LRS and HRS are stable depending on the history of applied voltage. Taking into account the mean values of 3.60 V for SET+ and 0.62 V for RESET+ and an interval of three standard deviations (3σ = 1.26 V and 0.54 V respectively), the operation window spans from 1.16 V to 2.34 V (width: 1.18 V) with 99.7 % confidence (under the assumption of Gaussian distribution). Alongside the narrower distribution of SET+ voltages compared to SET-, the positive branch of the hysteresis loop renders very promising for an application of noble metal alloy NPs as a diffusive memristive device.

So far, the description of diffusive memristive switching was limited to 70 consecutive hysteresis loops. Essentially, the nanoparticle-based memristive devices are very stable and show comparable switching behaviour for a high number of cycles. In order to illustrate the stability and reproducibility of diffusive memristive switching, the SET and RESET voltages corresponding to the first 2100 cycles of a representative measurement on a AgPt NP in the SiO_2/AgPt NP/SiO_2 stack are depicted in Figure 30. In contrast to the manual evaluation of the dataset with 70 switching cycles, this high number of hysteresis loops called for an automated evaluation (relying on the detection of extrema in the slope as well as current threshold values) of switching voltages. Apart from a statistical distribution of the switching voltages in agreement with the general trend observed for the dataset of 70 cycles, certain regions with a sudden drop in switching voltage are observed (e.g. around cycle 1100). A closer evaluation of the respective cycles reveals that these areas are artefacts due to imperfect detection by the applied algorithm. In fact, in the respective cycles there was no memristive switching observed. These fluctuations are attributed to limitations of the c-AFM measurement, in particular the AFM was operated at ambient air at room temperature, resulting in time dependent nanoscale deviations in positioning of the conductive tip. Accordingly, upon any change in position, the frustrated filament has to be reformed around the new location, resulting in imperfect memristive switching for some cycles. Notably, no systematic drift of the switching voltages over time has been observed, indicating the high stability of alloy NPs in the context of memristive switching.

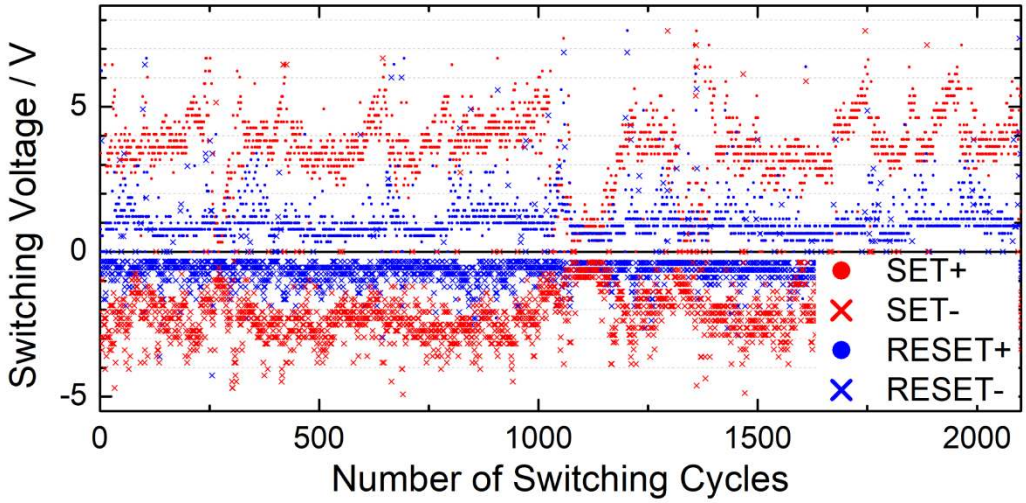

Figure 30: Switching voltages for the SET and RESET processes obtained from long-term measurements on an individual nanoparticle for the first 2100 switching cycles. Despite occasional fluctuations in the switching voltages due to limitations of the AFM setup (room temperature, ambient air), no systematic drift in the switching voltages is observed.

Despite these limitations related to the measurement by conductive AFM tip, the alloy NPs appear very promising for an application in memristive devices with diffusive switching characteristics. For the preparation of such devices, two main routes for an enhancement of the memristive properties are pursued: The transition from individual NPs to multiple stacks is studied in the context of allowing for additional control over the switching parameters, as the distances between the NPs can be tailored. In addition, the incorporation of a Cr wetting layer for a better conformity of the SiO_2 thin film separation layer deposited on noble metal contacts such as Au or Pt is investigated.

Effect of the addition of a Chromium (Cr) wetting layer

A thin film of Cr as a wetting layer between SiO_2 and noble metals (like Au or Pt) is routinely applied in order to enhance the adhesion between the individual components and achieve a better homogeneity of the deposited layer. The SiO_2/AgPt NP/SiO_2 stack investigated in the previous section was modified by inserting a thin film of Cr to the stack in between the Pt surface of the substrate layer and the bottom SiO_2 layer (cf. Figure 24). This Cr/SiO_2/AgPt NP/SiO_2 thin film stack was deposited by a sequence of deposition processes without breaking the vacuum. The nominal thickness of both dielectric SiO_2 layers was chosen to be 2 nm in order to rule out any effect of varying layer thickness on the SET and RESET voltages for different polarities.

The long-term stability of this Cr/SiO_2/AgPt NP/SiO_2 thin film stack was investigated by applying the conductive AFM tip to the position of an individual AgPt NP and recording IV hysteresis loops continuously over a measurement period of two days. Prior to this measurement, the surface of the thin film exhibited no significant irregularities regarding roughness and topography. After the two-day measurement, a severe structural change of the morphology of the memristive stack has been observed. In Figure 31 a, an AFM topography map of the respective region on the sample is shown. During the long-term measurement, a hill-like feature has formed under the tip, which extends with a circular base and a diameter of roughly 40 µm with its centre at the position of the AFM tip. This area shows two dominating features: A strong, dome-like elevation in the centre (red area) as well as radial stripes of fluctuating height around the dome. Such long-range morphological modification of the nanoscopic thin film stack is particularly surprising, especially under consideration of the radius of curvature of the conductive AFM tip in the low nm range.

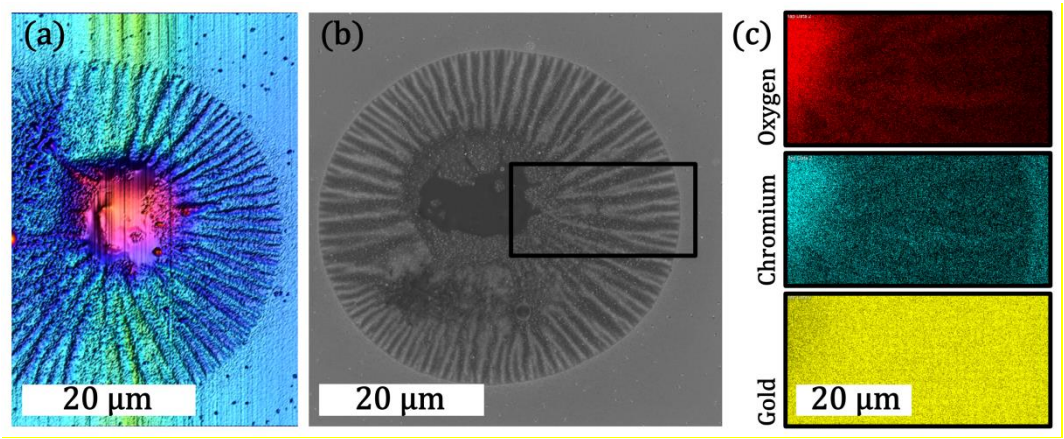

Figure 31: Long-term measurement induced migration of chromium on the micrometre scale: The AFM topography map (a, recorded and provided by Dr. Abdou Hassanien) and the corresponding SEM top view micrograph reveal structural changes on a circular area (diameter: roughly 40 µm) induced upon a two day continuous IV hysteresis measurement with c-AFM tip at the centre of the circular area. SEM EDX spectroscopy (c) of a selected area (black rectangle) indicates the migration and oxidation of Cr as the origin of the structural changes.

In order to understand the origin of these structural changes, the respective modified area was studied by SEM. The corresponding top view micrograph is shown in Figure 31 b and correlates well with the AFM topography map of the hill-like area in terms of diameter and general features. Applying SEM energy dispersive x-ray spectroscopy (EDX) on a selected rectangular region, the presence of the elements oxygen, chromium and gold was examined (depicted as elemental map in Figure 31 c, high colour saturation corresponds to high signal). The region was selected in such way, that the dome-like structure (left) as well as the radial fluctuations (middle) and an undisturbed region (right) are covered.

Gold (Au): The origin of the signal corresponding to Au is attributed to the conductive Au thin film related to the substrate. Over the whole investigated region, the signal corresponding to Au is almost constant. However, at the location of the dome-like feature the strength of the Au signal is reduced. This implies that the dome-like structure does not contain a significant concentration of Au and is covering the surface and thus reducing signal from the underlying substrate.

Silver (Ag): No signal corresponding to Ag from the alloy NPs could be investigated as the size and concentration of respective NPs is too low to be detected in SEM EDX.

Chromium (Cr): The presence of Cr strongly correlates with the observation of the three distinct features. In the undisturbed region on the right corner of the investigated region the signal correlating to Cr is homogenous and exhibits medium intensity. In contrast, in the region of the dome-like feature, the intensity of Cr is strongly enhanced. Simultaneously, in the centre region of the investigated rectangle, Cr is depleted. The radial contrast fluctuations in SEM micrograph and the topography fluctuations observed by AFM correlate well with Cr intensity fluctuations in this region.

Oxygen (O): While there is almost no oxygen observed in the undisturbed region, the presence of oxygen in the dome-like region and the radial fluctuations in the matches the intensity distribution of Cr very well.

On the background of these general observations for the elemental distributions and their relation to the topography, the following implications on the origin of the long-term changes can be concluded:

1. In the dome-like region, chromium oxide has aggregated and covered the surface of the thin film device. Thus the high intensity of signal corresponding to Cr and O overlap in this region and the signal of Au from the substrate is slightly reduced.

2. The region with the radial stripes of height and contrast fluctuations is caused by the depletion of Cr from the wetting layer. The signal of Cr and O overlaps in this region. There are stripes, in which there both elements exhibit low signal, while in different stripes both elements show high signal. Thus, the topographical fluctuations are caused by the presence or absence of chromium oxide in the

respective region. The radial arrangement of the stripes is caused by inhomogeneity in the electrical field, which ranges radially from the c-AFM tip. This implies that Cr is depleted, transported and oxidized from some paths more easy than from other paths.

3. In the undisturbed region, there is a considerable signal corresponding to Cr but simultaneously no O is observed. This indicates that in this region the Cr is not significantly oxidised. This observation correlates well with the expectation for a stable Cr wetting layer below the SiO_2/AgPt NP/SiO_2 thin film stack.

Over the course of the two-day measurement, the IV hysteresis loops were recorded to study the electrical properties of nanoparticle-based memristive stacks with Cr wetting layer. Representative hysteresis loops for Cr/SiO_2/AgAu NP/SiO_2 and Cr/SiO_2/AgAu NP/SiO_2 memristive devices are depicted in Figure 32. In contrast to similar stacks without Cr wetting layer, in these devices no diffusive memristive switching is observed in the investigated voltage range. The respective hysteresis loops exhibit a non-zero crossing (no pinched hysteresis) and several peaks, reminding of typical cyclic voltammetry data involving oxidation and reduction processes. Comparable curves are readily reported for ECM memristive devices relying on, e.g. Ag/Ta_2O_5/Pt or Cu/SiO_2/Pt stacks.[58,70,167,168] However, due to the limitations of the chosen measurement technique (e.g. the incorporation of a serial resistor for current limitation), the respective voltage values at the peak position do not directly relate to a specific process. In addition, unlike in typical cyclic voltammetry measurements, the current is recorded instead of the current density (due to the geometry of the tip).

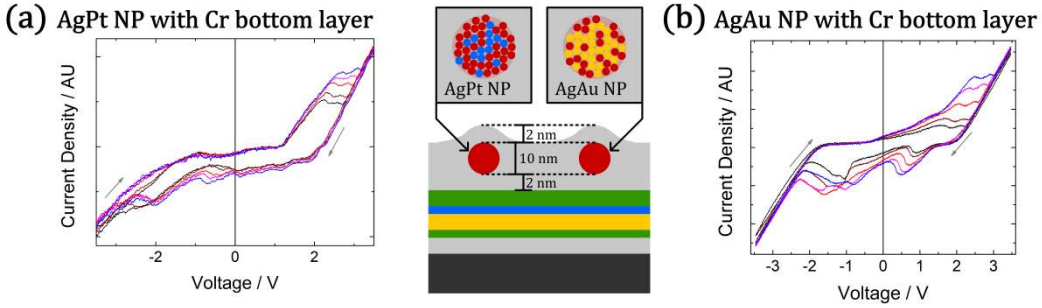

Figure 32: Hysteresis measurements of nanoparticle-based memristive devices relying on AgPt NPs (a) and AgAu NPs (b) and an additional Cr wetting layer. In contrast to the reproducible diffusive memristive switching observed for similar devices without Cr wetting layer, the hysteresis loops for Cr/SiO_2/NP/SiO_2 stacks show peaks of varying position and height. The colour scheme of the schematic thin film stack corresponds to Figure 24.

Nevertheless, the recorded IV characteristics for both stacks yield important indications in the context of the long-term stability of the memristive devices with additional Cr layer. Comparing the respective peaks in the IV hysteresis loops for subsequent cycles, changes in peak position and height of the individual peaks are observed. Such deviations typically indicate an unstable, time varying process, which is in general unfavourable for the design

of a stable memristive device. Two main explanations for the origin of the variation in peak position appear to be possible:

- The structural changes observed by AFM topography and SEM studies can be related to constant changes in the local chemical environment and local electrical field. Although the applied voltage in each cycle is always the same, due to local structural changes, the voltage drop over the sample can change, resulting in a change in the electrical field.

- The second explanation is related to the influence of oxygen or water vapour from the surrounding gas phase. The nanoparticle-based stack is open to ambient atmosphere and the Cr oxidizes as shown by EDX. Time dependent local changes in the availability of oxygen have already been reported to result in shifts of the respective peak positions related to the oxidation and reduction processes.[58,167]

Due to these long-term stability issues involved with the addition of a Cr wetting layer, this approach is disregarded for the development of further nanoparticle-based memristive devices.

4.1.4 Memristive Devices Relying on Multiple Stacks of Nanoparticles

Based on the results on diffusive memristive switching observed by c-AFM on individual NPs, in this section memristive devices relying on multiple stacks of noble metal alloy AgAu or AgPt NPs embedded in a dielectric SiO_2 matrix (multistack devices) are discussed. Using macroscopic contacts, the nanoscopic dimension of the individual SiO_2/NP/SiO_2 layers with a layer thickness of the dielectric of only a few nanometres makes reliable contacting very challenging. Thus, the transition from individual NP layers to multiple stacks allowed increasing the overall thickness and consequently reducing the risk of short circuiting by pin holes or due to mechanical impingement of contacts on the layer.

In this context, two different multistack devices have been prepared, involving either AgAu NPs or AgPt NPs. Each multistack device consists of five sequentially deposited layers of noble metal alloy NPs and SiO_2 as a separation layer. Following the nomenclature of the individual nanoparticle layers embedded in SiO_2, the multistack devices can be described as "SiO_2/NP/SiO_2/NP/SiO_2/NP/SiO_2/NP/SiO_2/NP/SiO_2". While in case of the AgAu NP multistack device the nominal layer thickness of the separating SiO_2 layers was selected to be 2 nm, the AgPt NPs were nominally separated by 4 nm of SiO_2. The IV characteristics of the devices are depicted in Figure 33 for 20 cycles in case of AgAu NP device and 60 cycles in case of the AgPt NP device, alongside a schematic cross section through the nanoparticle-based multistack devices.

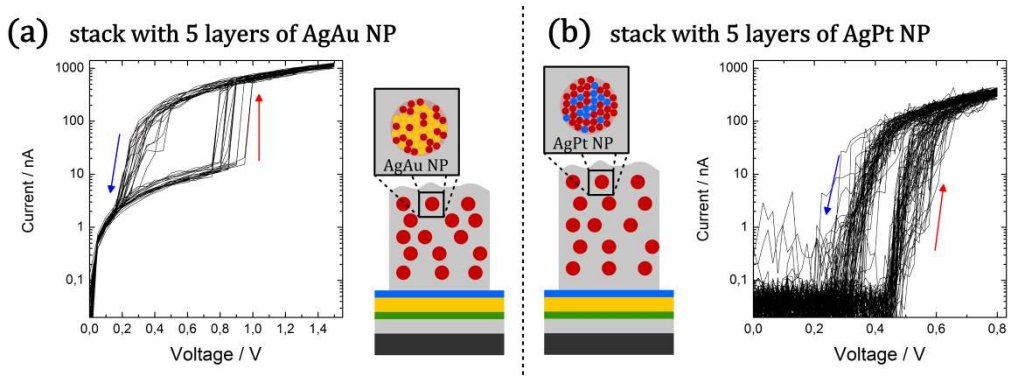

Figure 33: Diffusive memristive switching in nanoparticle based memristive devices: (a) Schematic cross section and 20 subsequent switching cycles shown for a AgAu NP device relying on five layers of NPs embedded in SiO_2; (b) Schematic cross section and 60 subsequent switching cycles shown for a AgPt NP device relying on five layers of NPs embedded in SiO_2. The colour scheme of the schematic thin film stack corresponds to Figure 24.

The AgAu NP and AgPt NP multistack devices show diffusive memristive switching for each of the observed hysteresis loops. In each case, the SET (red arrow) and RESET (blue arrow) occurs with a certain distribution around distinct voltages, yielding a clear operational window in between. This behaviour is in good agreement with the diffusive memristive switching observed in the c-AFM measurements of individual NPs. The LRS is mainly determined by the serial resistance of 1 MΩ, which was applied in order to be consistent with the c-AFM investigations. Upon a closer look on the IV characteristics of both devices, certain differences in the electrical behaviour can be observed:

In case of the AgAu NP device as depicted in Figure 33 a, the HRS correlated to a resistance of roughly 70 MΩ. In contrast, the AgPt NP device as depicted in Figure 33 b, exhibits a higher resistance in its HRS, which limits the current in HRS to be below the limit of reliable detection. The origin of this difference in HRS is attributed to the different layer thickness of the SiO_2 separation layers in between the individual NP layers. For the preparation of the AgPt NP device, the nominal thickness of each SiO_2 layer was doubled in comparison to the AgAu NP device (roughly 4 nm instead of 2 nm). Accordingly, the higher overall thickness of the AgPt NP device impacts the HRS. This indicates a key aspect of the versatility of the approach of a nanoparticle-based memristive device, namely the possibility of using the thickness of the dielectric layer to tailor the high resistance state, which is highly interesting in the context of low power operation.

As a general impression from the IV hysteresis loops as shown in Figure 33, for both multistack memristive devices, the switching voltages related to the respective SET and RESET process are distributed over a reasonably narrow range. In order to investigate the statistics of the switching processes in more detail, the switching voltages are evaluated for each subsequent cycle and the respective histograms as well as probability plots for the SET and RESET process are plotted. For the AgAu NP device, the evaluation of individual switching events is depicted in Figure 34 and for the AgPt NP device in Figure 35.

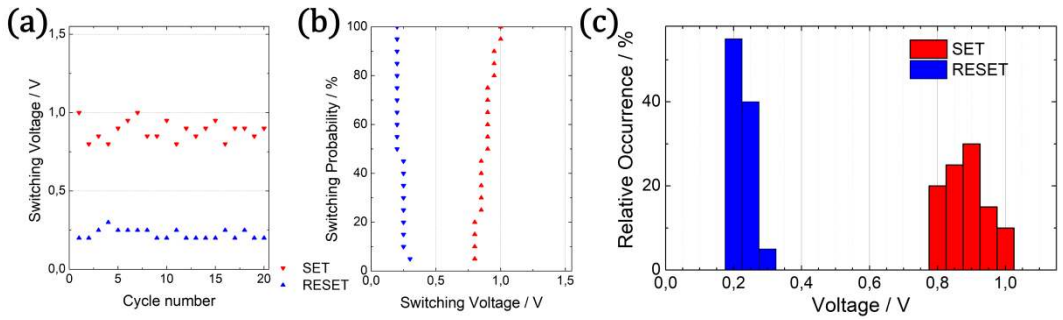

Figure 34: Evaluation of switching voltages for 20 consecutive switching cycles (a) in a AgAu NP multistack device. The probability plot (b) and the histogram (c) show a narrow distribution of the respective SET and RESET voltages.

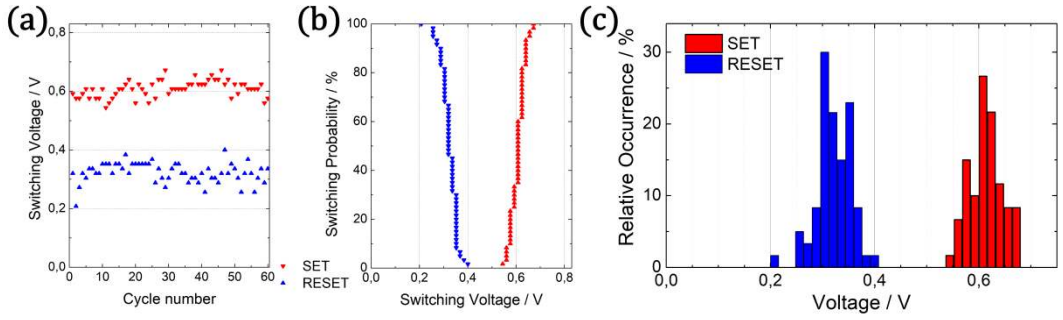

Figure 35: Evaluation of switching voltages for 60 consecutive switching cycles (a) in a AgPt NP multistack device. The probability plot (b) and the histogram (c) show a narrow distribution of the respective SET and RESET voltages.

The evaluation of the cycle dependency of the voltages attributed to the individual switching events shows that there is no significant drift, thus the respective voltages are distributed evenly for the whole range of investigated switching cycles. This observation is an important prerequisite for the statistical evaluation. In the following, a Gaussian distribution is assumed and the respective mean values, standard deviations, median values and minimum and maximum of the switching voltages are compared for the AgAu and AgPt NP multistack device in Table 2.

Table 2: Overview over the SET and RESET voltages extracted from multiple cycles (AgAu: 20 cycles; AgPt: 60 cycles) of diffusive memristive switching. Mean (average) voltage: V_{mean}; standard deviation: σ; voltage median: V_{med}; minimum and maximum: V_{min} and V_{max}.

	Process	V_{mean}	σ	V_{med}	V_{max}	V_{min}
AgAu NP multistack device	SET / V	0.89	0.06	0.90	1.00	0.80
	RESET / V	0.23	0.03	0.20	0.30	0.20
AgPt NP multistack device	SET / V	0.61	0.03	0.61	0.67	0.54
	RESET / V	0.32	0.03	0.32	0.4	0.21

Comparing the SET and RESET voltages for both multistack devices, a general trend can be observed:

- The mean SET voltage observed for the AgPt NP device is 0.61 V while the AgAu NP based device exhibits a higher mean SET voltage of 0.89 V. Thus the multistack device with AgPt NPs is switching from its HRS to LRS state at lower voltages. Considering the higher separation width of the NP layer in the AgPt NP device, this observation seems rather counterintuitive, because the higher thickness of the SiO_2 separation layer in the AgPt NP multistack device is expected to result in a lower electrical field in between the NPs (at identical applied voltage). However, the Ag content in the AgPt NPs is much higher than in the AgAu NPs. The quantification of similarly prepared NPs yielded a mole fraction of Ag in the respective NPs of roughly 0.8 (AgPt NP) and 0.3 (AgAu NP). Considering the shift towards lower SET voltages for the AgPt NP based device, the higher Ag content seems to facilitate the ionisation and release of silver cations from the AgPt NPs.

- For both devices the SET and RESET voltages are clearly separated, which is illustrated by the probability plots and histograms. There is no overlap between SET and RESET events for any of the investigated cycles. Considering the smallest observed SET and the largest observed RESET voltage, no switching event is occurring within an operation window of 0.50 V or 0.14 V for the AgAu or AgPt NP device respectively. Taking into account the mean values and an interval of three standard deviations (for 99.7 % confidence), the operation window for the AgAu device ranges from 0.32 V to 0.71 V (width: 0.39 V) and for the AgPt device from 0.41 V to 0.49 V (width: 0.08 V). Accordingly, both multistack nanoparticle-based devices allow for reproducible operation as diffusive memristive devices.

Recently, Wang et al. reported in Nature Materials comparable diffusive memristive switching in MgO_x:Ag, SiO_xN_y:Ag and HfO_x:Ag thin films with a thickness of roughly 15 nm, which were deposited by cosputtering in reactive atmosphere. These devices show interesting similarities to the devices investigated in the framework of this thesis, namely the similar choice of materials, layer thickness and the overall shape of the IV curves. Although no detailed statistical evaluation of the IV hysteresis loops was described in their work, a general comparison of the IV hysteresis loops indicates that the multistack devices presented here are very competitive. Typical SET voltages range from roughly 0.2 V (HfO_x:Ag) to 0.4 V (SiO_xN_y:Ag) and exhibit a similar distribution as observed for the multistack memristive devices. Interestingly, Wang et al. observed the local formation of chains of Ag NPs inside the matrix by *in situ* TEM investigations, which is related to the SET process. Simultaneously the RESET process is attributed, in addition to the processes described here, to the coalescence of individual NPs due to a minimization in surface energy. However, on the background of the electron beam induced effects observed in pure SiO_2 thin films (section 4.1.2) these conclusions from *in situ* TEM studies have to be treated with caution.

In contrast to the nanoparticle-based memristive devices, the diffusive memristive devices prepared by Wang et al. incorporate Ag as mobile species by sputtering from a planar Ag target. Thus there are no preformed NPs embedded into the matrix, but individual atoms are arriving at the surface and may form NPs due to self-organization and minimization of surface energy. Applying the concept of nanoparticle-based memristive devices described in this thesis, the NPs are already preformed with a well-defined composition and size in the gas phase synthesis and are embedded into the dielectric with tailored separation distances.

This illustrates the high potential of the concept and general set-up of multistack memristive devices, which opens two general routes to be applied as degrees of freedom in the design of memristive devices with well-defined memristive switching properties:

- A variation of the separation width (layer thickness of the SiO_2 intermediate layers) can be applied to tailor the HRS of the multistack memristive device.

- The composition of the alloy NPs can be varied in order to influence the switching voltages for the SET and RESET step.

Indications on the underlying conductivity mechanisms

In order to determine the dominating conduction mechanisms in the multistack nanoparticle-based memristive devices, an alternative plot (power exponent plot) of the hysteresis loop as proposed by C. Acha [30] is applied to averaged IV hysteresis data for the AgAu NP and AgPt NP devices in Figure 36. The measured IV hysteresis data (grey lines) are averaged in order to extract the essential information for the LRS (blue line, error bars correspond to standard deviation) and the HRS (red line, error bars correspond to standard deviation). In case of the AgPt NP device, due to the detection limit of the source meter, the current in the HRS is within the detection limit and no averaged data for HRS were obtained.

These reduced data were used to prepare a power exponent plot for each sample. The plot for the AgAu NP device (Figure 36 a) reveals the HRS (red plus signs) to have an almost constant power exponent of 1, which relates to ohmic conductivity as dominating conductivity mechanism. For the LRS, the power exponent varies between 2 for lower voltages and 1 for higher voltages. This behaviour implies a deviation from pure ohmic conductivity and corresponds well with the behaviour expected for two resistive elements in series: one ohmic and one space charge limited resistive element. The existence of the ohmic serial resistance is well explained by the measurement setup (cf. Figure 20). The occurrence of a space charge limited resistive element indicates that in the low resistive state the nanoparticle-based memristive device is dominated by space charge limited conductivity.

However, the diffusive switching behaviour observed in the nanoparticle-based memristive devices imposes an additional limitation on the application of the power exponent plots: At low voltages, the device switches from its LRS to its HRS and thus the voltage dependency of the LRS cannot be measured at voltages below the RESET switching threshold. In case of the AgPt NP device (Figure 36 b), the power exponent deviates strongly from ohmic behaviour. While at high voltages, the power exponent approaches 1, at lower voltages higher power exponents up to 3.5 are observed. Such behaviour implies that in the low resistive state, the AgPt NP device exhibits additional conductivity mechanisms. Comparable power exponents with an asymptotic decrease towards 1 (for ohmic behaviour at high voltages) were reported by C. Acha for an ohmic resistor in series to a parallel circuit of another ohmic resistor and a resistive element dominated by Poole-Frenkel emission. In this case, the power exponent exhibits a peak, which can be higher than 2. As 2 is the expected value for space charge limited conduction, the power exponent data indicate that space charge limited conductivity is not the dominating mechanism in the LRS. The recorded behaviour of the power exponent for the LRS of the AgPt NP device may be seen as indication for Poole-Frenkel emission as dominating conductivity mechanism in the LRS. However, the inaccessibility of the LRS at low voltages does not allow for a measurement of the power exponent over the whole voltage range. Thus, although indications for the dominating conductivity in the AgAu and AgPt NP devices could be obtained, no definitive statement on the basis of the experimental data can be given.

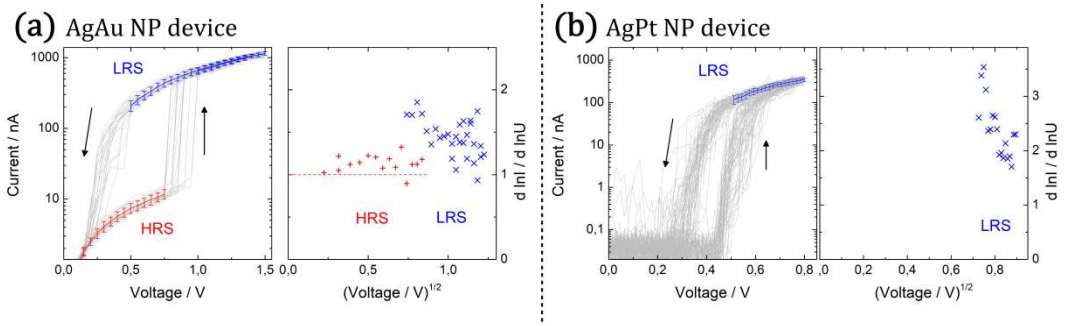

Figure 36: The hysteresis loops of a multistack AgAu NP (a) and AgPt NP (b) device are evaluated in order to extract averaged data for the HRS (red plus signs) and LRS (blue crosses). Based on the averaged data, a power exponent plot according to C. Acha is created (right graphs). The HRS of the AgAu NP device correlates well with a straight line around 1, which indicates ohmic conductivity as dominating conduction mechanism.

4.2 Sensing of UV-light and Gas Molecules with Semiconducting Metal Oxide Nanostructures

Semiconducting metal oxides are routinely used for sensing of UV-light and gas molecules and a broad variety of sensors relying on different oxide materials has been reported so far. In this section, two main concepts for the enhancement of key sensing properties (such as sensitivity and selectivity) will be explored. First of all, in section 4.2.1, the impact of surface functionalization by noble metal NPs will be shown. Subsequently, section 4.2.2 focusses on the description of nanostructured TiO_2 and CuO thin films with tailored morphologies obtained by reactive magnetron sputtering.

4.2.1 Alloy Nanoparticles for Enhanced Sensing

In order to study the impact of noble metal NP decoration on the sensing properties of semiconducting metal oxides, the approach of deposition of metallic NPs from gas phase synthesis was combined with existing fabrication routines for sensor materials, which have been prepared by the group of Prof. Ion Tiginyanu in close collaboration with Dr. Oleg Lupan. In this context, silver and iron doped columnar ZnO thin films (ZnO:Ag and ZnO:Fe respectively) obtained by synthesis from chemical solutions were used as base layers for the surface decoration with metallic NPs.

Based on the concept of a single segmented target for the deposition of metal alloy NPs as well as conventional metallic targets, particles ranging from Ag over AgAu and AgPt have been prepared. The characteristics of the gas phase synthesis in a Haberland type GAS offer certain advantages over conventional solution-based NP synthesis:

1. Well-defined coverage of the thin film surface is easily realised by tailoring the deposition time.
2. The surface of the metal oxide thin film is not subjected to any solvent, which limits the risk of chemical changes to the thin film.
3. After successful deposition of NPs from the gas phase, the sensor is ready to use and no further heat treatment step has to be performed, e.g. to remove the remaining solvent.
4. The deposition of alloy NPs with well-defined composition is feasible and the composition of the NPs can be tailored easily during the deposition (e.g. using the segmented target approach developed in this work).

In the context of an enhancement of the sensing properties by surface decoration with metallic NPs, the respective coverage is crucial. As the sensor surface should be still accessible to the gas molecules or the UV light stimulus, the NP layer should be well below the percolation threshold and agglomeration of NPs should be avoided. These criteria are readily fulfilled by NPs deposited from gas phase synthesis, which is demonstrated by SEM micrographs of AgPt NPs and AgAu NPs on silicon wafer pieces as well as ZnO:Ag thin films. Independent of the substrates, the NPs deposited by gas phase synthesis via sputtering are well distributed over the surface and show no significant agglomeration, making this

approach an ideal candidate for the application in surface decoration of sensor thin film structures.

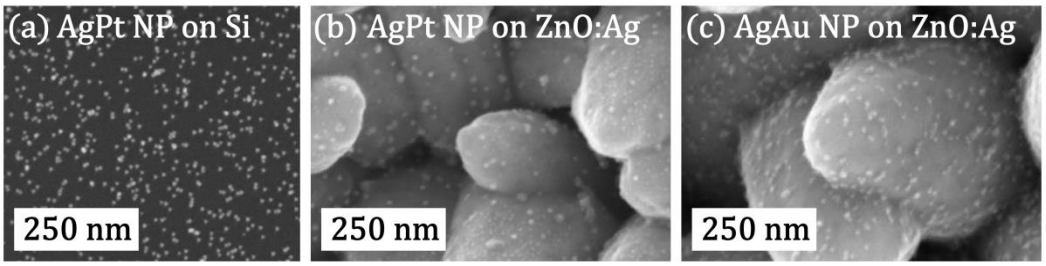

Figure 37: Nanoparticles deposited from GAS exhibit narrow size distribution and are well dispersed on the surface without showing significant agglomeration. SEM micrographs were recorded in top view configuration for AgPt NPs on a silicon wafer piece (a) as well as ZnO:Ag sensor structures decorated with AgPt NPs (b) and AgAu NPs (c).

As a first approach to tailor the sensing properties by surface decoration with NPs, columnar ZnO:Fe thin films obtained from synthesis from chemical solutions have been investigated with respect to their gas sensing properties. In this context, hydrogen (H_2) as well as methane (CH_4) and ethanol (C_2H_5OH) have been considered as gas species for the evaluation of the sensor response. Comparing a ZnO:Fe thin film in its pristine state as well as after surface functionalization by Ag NPs at a typical operation temperature of 300 °C, the sensitivity towards 20 ppm of ethanol vapour was increased from roughly 15 (in case of the pristine thin film) to about 63 (after surface decoration). The gas sensing results underline that the Ag NP decorated ZnO:Fe columnar thin film is highly selective towards ethanol vapours, which is underlined by the low response (sensitivity below 5) towards H_2 and CH_4 even at 1000 ppm.

Different types of noble metal particles, namely Ag, AgAu and AgPt NPs, have been deposited onto ZnO:Ag nanostructures in order to enhance the sensing properties towards UV light. The UV response of ZnO:Ag thin film sensors without surface functionalization results in a change in resistivity by a factor of 17. Upon surface functionalization with Ag NPs, the UV response was enhanced to a factor of 46. Applying alloy NPs to the surface of the ZnO:Ag nanostructured thin films, the UV response is raised further to a factor 60 and 68 for AgPt and AgAu NPs respectively. Alongside this strong enhancement in the UV induced change in resistivity, the corresponding response and recovery times are simultaneously reduced from roughly 14.5 s for undecorated thin films to roughly 1.0 s in case of thin films with AgAu NPs. The origin behind this significant enhancement in sensing properties is related to the formation of ZnO:Ag/NP Schottky barriers due to the high work function of the noble metal NP constituents (e.g. 5.9 eV in case of platinum). Upon the formation of this Schottky barrier, the electron depletion region in the vicinity of the nanoparticles is widened, resulting in a higher UV performance.

The full details on the work related to the enhancement of sensing properties by surface decoration with metallic NPs are presented in the following publications:

V. Postica, **A. Vahl**, N. Magariu, M.-I. Terasa, M. Hoppe, B. Viana, P. Aschehoug, T. Pauporté, I. Tiginyanu, O. Polonskyi, V. Sontea, L. Chow, L. Kienle, R. Adelung, F. Faupel, O. Lupan, *Enhancement in UV Sensing Properties of ZnO:Ag Nanostructured Films by Surface Functionalization with Noble Metallic and Bimetallic Nanoparticles*, Journal of Engineering Science. 3 (2019) 41-51. doi:10.5281/zenodo.2557280.

V. Postica, **A. Vahl**, J. Strobel, D. Santos-Carballal, O. Lupan, A. Cadi-Essadek, N.H. de Leeuw, F. Schütt, O. Polonskyi, T. Strunskus, M. Baum, L. Kienle, R. Adelung, F. Faupel, *Tuning doping and surface functionalization of columnar oxide films for volatile organic compound sensing: experiments and theory*, J. Mater. Chem. A. (2018) 21–27. doi:10.1039/C8TA08985J.

4.2.2 Deposition of Nanocolumnar Metal Oxide Thin Films with Tailored Morphologies

In contrast to the columnar ZnO thin films deposited by chemical solution synthesis described in the previous chapter, this section will focus on the PVD-based deposition of metal oxide thin films. In this context, the method of pulsed DC reactive magnetron sputtering (as already applied to deposit the dielectric SiO_2 matrix in connection with the nanoparticle-based memristive devices) will be explored for the deposition of nanocolumnar semiconducting metal oxide thin films with adjustable morphologies. In the design of thin films for UV-light and gas sensing applications, a higher surface is commonly attributed to higher sensing performance. Consequently, columnar thin films with well-separated columns with nanoscopic diameters appear as an ideal candidate for an application in the field of sensing. In this section, two pathways for the deposition of TiO_2 and CuO thin films with such nanocolumnar morphology will be discussed. First, the formation of nanocrack networks in TiO_2 thin films upon post deposition heat treatment is presented as an efficient approach to obtain crystalline anatase thin films with defined cracks. Subsequently, the impact of the composition of the reactive atmosphere during sputter deposition of CuO and TiO_2 is discussed in terms of the impact on the thin film morphology.

For further details, the reader is referred to the following publications:

B. Henkel, **A. Vahl**, O.C. Aktas, T. Strunskus, F. Faupel, *Self-organised nanocrack networks: A pathway to enlarge catalytic surface area in sputtered ceramic thin films, showcased for photocatalytic TiO_2*, Nanotechnology. 29 (2018) 035703. doi:10.1088/1361-6528/aa9d35.

A. Vahl, J. Dittmann, J. Jetter, S. Veziroglu, S. Shree, N. Ababii, O. Lupan, O. C. Aktas, T. Strunskus, E. Quandt, R. Adelung, S. K. Sharma, F. Faupel, *Reactive sputtering of metal oxide thin films: The impact of O_2/Ar ratio on thin film morphology*, Nanotechnology. 30 (2019) 235603. doi:10.1088/1361-6528/ab0837.

For the deposition of TiO_2 thin films, typically a reactive gas atmosphere with an oxygen flow of 10 SCCM and an argon flow of 250 SCCM was chosen. The high availability of oxygen from the reactive atmosphere and the strong tendency of metallic titanium to oxidize in the

presence of oxygen are crucial to understand the morphology of the as grown thin film (Figure 38 a).

At the interface between the TiO_2 thin film and the silicon substrate, irregular and narrow columns (indicated by red lines) are the dominating structural features, reminding of a typical transition zone morphology that is attributed to the low surface diffusion of deposited material. From a distance of roughly 200 nm from the substrate onwards, broader columnar structures (indicated by blue lines) are observed. As the deposition is initialised, the surface of the substrate offers a high number of available nucleation sites. The high availability of reactive oxygen species leads to the growth of a stoichiometric TiO_2 thin film as the deposited Ti species are readily saturated by oxygen. These saturated bonds as well as the low surface diffusion prevent significant coalescence of columns or seeds. Due to the limited thermal conductivity, the temperature at the deposition front increases gradually during deposition and anatase crystallites start to grow, forming conical shaped grains.

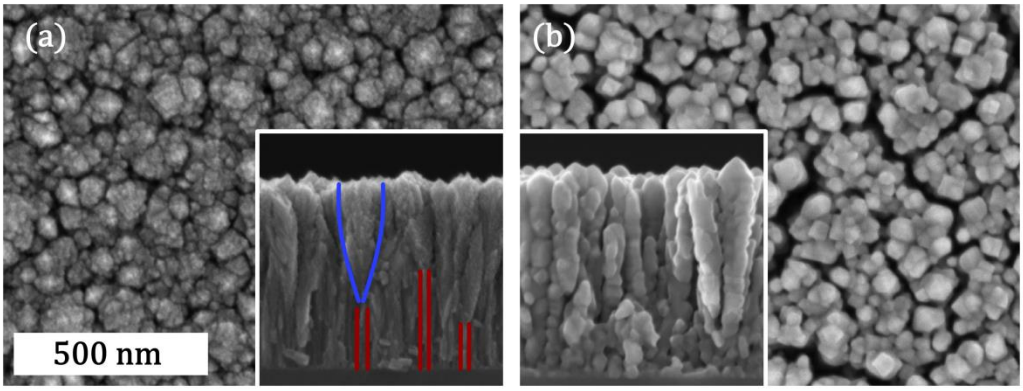

Figure 38: SEM micrographs in top view and cross section (inset) of TiO_2 thin films before (a) and after (b) post deposition heat treatment. The morphologically dominating features before heat treatment are marked with red and blue lines.

The morphology of such TiO_2 thin films is strongly affected by the post deposition heat treatment step (typically 1 h at 650 °C). Although in cross sectional view (Figure 38 b) the thin films before and after heat treatment show certain similarities, the top view micrograph reveals a striking difference: A network of nanoscopic cracks in between bundles of individual TiO_2 columns with high aspect ratio is observed. A closer view on the cross-sectional micrographs also reveals that the rough features on the individual columns are smoothed after the heat treatment step, resulting in a more homogenous surface of the respective TiO_2 nanocolumns. In addition, Raman studies indicate a strengthening of peaks related to the crystalline anatase polymorph of TiO_2 after the heat treatment step. Based on these observations, the mechanism of nanocrack formation (schematically depicted in Figure 39) in TiO_2 thin films deposited by pulsed DC reactive sputtering can be explained as follows:

(a) The as deposited TiO_2 thin film contains two distinct morphological features: A highly defective layer in vicinity to the substrate and a columnar, partially crystalline anatase layer.

(b) Upon heating, the difference in thermal expansion coefficients of the substrate and the thin film results in the TiO_2 thin film being subjected to compressive stress. The initially present columns crystallise and densify, reducing the total compressive stress on the thin film. Due to the saturation by oxygen, individual columns do not coalesce.

(c) After cooling to room temperature, the compressive stress in the thin film is relaxed. Due to the densification of the individual columns, the thin film is subjected to tensile stress, resulting in preferential crack formation along the flanks of individual columns.

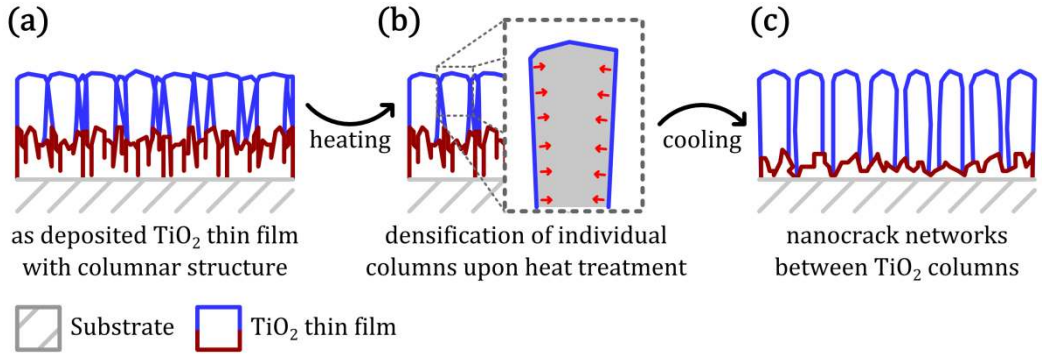

Figure 39: Schematic model of nanocrack formation in TiO_2 thin films upon thermal treatment: (a) The as deposited thin film exhibits a columnar structure, (b) the individual columns densify upon heat treatment due to the successive crystallisation from partially amorphous TiO_2 to the anatase phase, (c) after cooling a network of nanoscopic cracks between the columns remains.

In conclusion, decisive for the development of a network of nanoscopic cracks upon post deposition heat treatment is the morphology of the thin film in the as deposited state as well as its crystallinity.

A characteristic feature of reactive sputtering is the presence of a reactive gas atmosphere. In the case of the deposition of TiO_2 and CuO this is achieved by a mixture of Ar and O_2 gas inside the vacuum chamber. The deliberate variation of the ratio of gas flows of Ar and O_2 influences the composition of the reactive gas atmosphere and consequently the availability of oxygen species during the deposition process. A precise control over the O_2/Ar ratio offers an additional degree of freedom to tailor the characteristics of the deposition process and consequently impacts the morphology of the deposited thin film. The following section will describe how a variation of the gas atmosphere can be applied in order to deposit TiO_2 and CuO thin films with well-defined nanocolumnar morphology.

TiO_2 thin films were prepared at different O_2/Ar ratios. Top view SEM micrographs of these thin films after post deposition heat treatment are depicted in Figure 40. An oxygen content of 4% corresponds to the deposition described already in the context of nanocrack formation upon post deposition heat treatment (as depicted in Figure 38). In case the O_2/Ar ratio is doubled, the nanocrack network is more pronounced and the separation between the bundles of individual columns is increasing. This effect is attributed to the following reason: The deposition rate goes down with increasing oxygen content in the reactive gas atmosphere, resulting in a longer deposition time for the same layer thickness. Alongside the

lower deposition rate, the deposited Ti species experience a longer time on the surface of the deposit before they are buried by subsequently deposited atoms. Accordingly, the slower deposition results in a higher content of crystalline anatase seeds in the as deposited thin film. This allows for a more efficient densification upon crystallization during the post deposition heat treatment. For a lower oxygen content of only 2%, the morphology of the TiO_2 thin film shows no nanocrack network, but a more regular and closed layer, which is in line with an explanation based on a higher deposition rate at lower oxygen ratio.

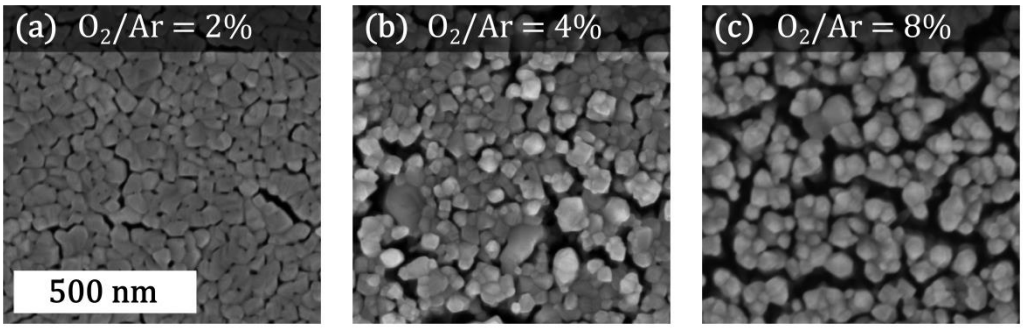

Figure 40: Top view SEM micrographs of TiO_2 thin films after post deposition heat treatment at 650 °C for 1 h. The thin films were prepared by reactive sputtering in different reactive atmospheres. While the thin film surface at an O_2/Ar ratio of 2% (a) exhibits occasionally thin cracks, with increasing oxygen ratio the width and number of cracks increases and in case of an O_2/Ar ratio of 8% (c) a fully connected network of nanoscopic cracks is obtained.

The nanocrack network morphology with its nanoscopic columns and deep trenches in between the TiO_2 nanocolumn bundles appears well suited for the application in context of sensing.

Semiconducting metal oxide sensors based on the concept of depositing nanocolumnar thin films by reactive sputtering can also be combined with the approach of noble metal nanoparticle surface decoration. However, the nanocrack network formation necessarily involves a post deposition heat treatment step (typically at 650 °C for 1 h). Such post deposition heat treatment may impose limitations on the applicability of TiO_2 nanocrack thin films alongside surface decoration with noble metal NPs. In order to prevent agglomeration or Ostwald-ripening of NPs, the NPs would ideally be deposited onto the TiO_2 thin film in a second deposition step after the heat treatment was performed.

In order to prepare sensor thin films that combine the nanocolumnar morphology and incorporate noble metal NPs in a single vacuum-based deposition step, another semiconducting metal oxide, which exhibits nanocolumnar morphology in the as deposited state, has to be found. For this purpose, CuO with its relatively lower melting temperature was investigated with respect to the thin film morphology and its dependency on the O_2/Ar ratio during the deposition. The respective top view SEM micrographs of CuO thin films deposited at O_2/Ar ratios of 2 %, 4 % and 8 % are depicted in Figure 41. Regarding the thin film morphology, the CuO thin film prepared at the lowest O_2/Ar ratio shows strong similarities to the nanocrack network TiO_2 thin film, although the CuO thin films are in their as deposited state and the TiO_2 thin film have been subjected to a post deposition heat treatment. Independent of the reactive gas atmosphere during sputtering, all thin films in

the as deposited state comprised of crystalline CuO, as investigated by Raman spectroscopy (Figure 42 a). For higher oxygen contents, the CuO thin film shows well-separated, high aspect columnar structures with a column diameter in the range of 20 nm for the highest O_2/Ar ratio. Comparable to the observations in case of TiO_2, a higher oxygen content in the reactive gas atmosphere during deposition relates to nanocolumnar structures with a smaller feature size, which seem well suited for an application in sensing.

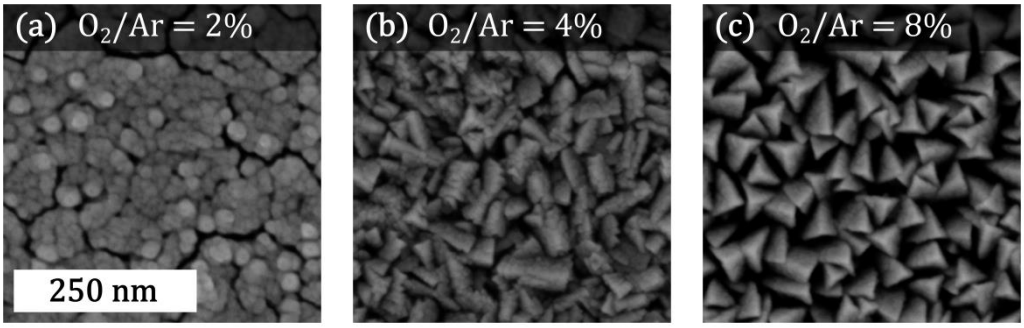

Figure 41: Top view SEM micrographs of CuO thin films deposited by reactive sputtering in different reactive atmospheres. While the thin film surface at an O_2/Ar ratio of 2% (a) exhibits occasionally thin cracks, with increasing oxygen ratio separation of individual columns increases while the diameter of individual columns decreases. In case of an O_2/Ar ratio of 8% (c), well-separated CuO columns with a high aspect ratio and a diameter in the range of 20 nm are obtained.

In order to demonstrate the application potential of nanocolumnar semiconducting metal oxide thin films in the field of gas sensing, sensors based on CuO thin films prepared at high oxygen contents have been subjected to H_2, n-butanol and 2-propanol. The time dependent gas response (change in resistivity upon introduction of the respective gas species) is shown in Figure 42 b for a pristine CuO sensor as well as a CuO sensor decorated with AgAu NPs (Figure 42 c). The optimal operating temperature for the pristine sensor was 325 °C while the NP decorated sensor was operated at 350 °C. The nanocolumnar CuO thin film sensor shows fast response with similar sensitivity towards all of the three investigated gas species. Especially the fast response and recovery times (in the order of seconds) turn these thin films into promising candidates for sensor applications. However, the low selectivity limits the field of usage.

Upon surface functionalization of the CuO nanocolumns with AgAu NPs, the sensitivity towards 2-propanol was increased (roughly by a factor of 1.6), while the sensitivity towards H_2 and n-butanol remained rather unchanged. Accordingly, such sensor nanocomposite shows a higher selectivity towards 2-propanol. Although, at first glance, the sensing performance of these nanocomposite CuO/NP thin film sensors may appear poor in comparison to the well-optimised doped ZnO thin film sensors discussed in section 4.2.1, the application potential of merging nanocolumnar thin films and noble metal NP surface decoration is well demonstrated. On top of the feasibility of tuning the sensor selectivity by surface decoration with NPs, the whole CuO/NP sensor nanocomposite was manufactured in a single PVD-based deposition step without the necessity of any additional heat treatment step. As such, the concept of nanocolumnar thin film sensors appears very promising for integration (e.g. as sensor component in memsensors) and further research is expected to

significantly increase the sensing properties of the showcased CuO/NP thin film sensor prototype.

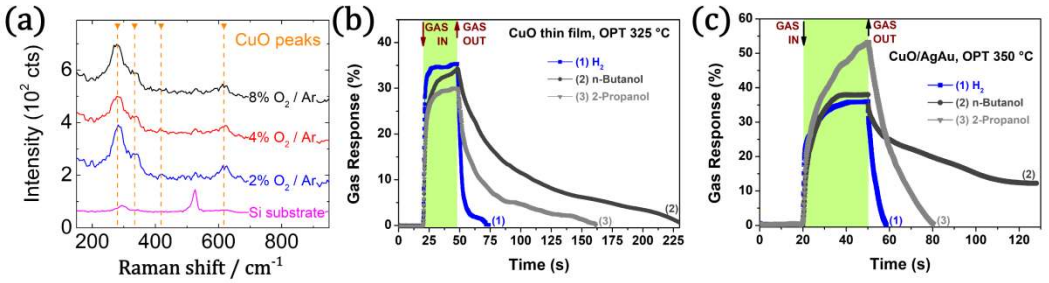

Figure 42: (a) Raman spectroscopy of the deposited CuO thin films without any post deposition heat treatment reveals the presence of CuO for all investigated reactive gas atmospheres. For the determination of the response of a nanocolumnar CuO sensor in its pristine form (b) as well as after surface decoration with AgAu NPs (c), H_2, n-butanol and 2-propanol are applied to the sensor (green bar). While the pristine sensor exhibits comparable sensitivity to these three gases, the selectivity is shifted towards 2-propanol for the AgAu NP decorated sensor.

4.3 Memsensors: Combining Sensing and Memristive Switching for Emerging Properties

Having thoroughly discussed memristive devices and sensors in the previous part of this thesis, this section is devoted to the junction of the individual properties of both device classes in the form of memsensors. In this context, memsensors merge the properties of their individual components, namely stimulus dependent resistance and memristive switching with distinct resistance states, which allows for novel, emerging features. Therefore, memsensors are highly interesting with respect to the realization of biologically motivated functionalities in the context of neuromorphic engineering.

One key aspect in neural networks is the close connection between the detection of signals (sensing) and the consecutive data processing (e.g. in terms of synaptic plasticity). To illustrate this, consider the following, simplified picture:

> The human body is covered with a plethora of sensing structures, ranging from an array of hair follicles over the olfactory system to the visual system, and each sensing structure is connected to a variety of neurons and neuron assemblies. With this highly parallel setup our body is capable of simultaneously detecting and processing sensory information in real time and only the most important stimuli are brought to our consciousness. Without the highly mandatory local data pre-processing, the constant stream of sensory excitations would literally blow our minds.

In contrast to conventional electronics, in which data detection and data processing are typically performed separately, memsensors show the potential to close this particular gap. The most basic junction of data detection and processing is to be found in adaptation, which is commonly regarded as a core feature of neural systems. In the simplified macroscopic picture, adaptation can be understood as follows:

> Imagine a crowded lecture hall. As you enter, the windows are open and the room is filled with fresh air. The presentation starts and the windows are closed. With every breath the quality of air decreases – gradually, no sudden change, you don't recognise it. The lecture is almost over as a colleague hurries over the bright, well-ventilated hallway and reaches the lecture hall. He opens the door and enters the room. Suddenly he recognises that the air in the room is nowhere close to be called fresh. Although the two of you breathe the same air, the two responses are very different. While the gradual changes you experienced were blanked out, the sudden changes that your colleague experienced were transmitted to his consciousness.

In the context of neurons, adaptation is typically discussed with respect to spike frequency adaptation, i.e. the frequency of pulses is proportional to the external stimulus acting on a neuron and the frequency asymptotically decreases over time (depicted schematically in Figure 43 a). Although in classical electronics, any sensor with a time dependent response to a constant stimulus is typically regarded as a device with inferior performance, in neuromorphic engineering such adaptation to a constant stimulus is a highly sought-after feature, which would allow for new, brain inspired circuits. In neural networks such as the

human brain, the spiking of individual neurons as well as the interaction with the highly interconnected neuron assemblies leads to a strong time dependence of voltage pulses.

For a technical realisation in neuromorphic circuits, an operation with constant applied voltage instead of a pulsed operation is commonly regarded as more simple. As a closely related approach, adaptation can also be realised in the amplitude of the response instead of the frequency of spikes. In Figure 43 b amplitude adaptation is presented as an analogue to spike frequency adaptation, which roughly relates to an integration over the individual spikes.

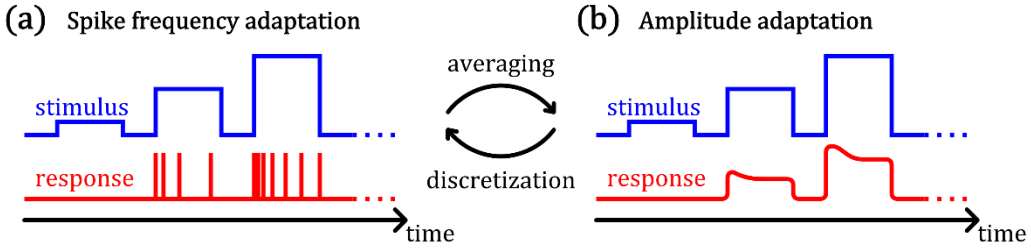

Figure 43: Adaptation to an external stimulus: The relation between spike frequency adaptation (a) and amplitude adaptation (b) for memsensor devices. In spike frequency adaptation, the frequency of spikes is proportional to the strength of the stimulus and decreases asymptotically over time. In amplitude adaptation, the amplitude of the response is proportional to the strength of the stimulus and decreases asymptotically over time.

In the framework of this thesis, the concept of memsensors was investigated with a particular focus on the following questions:

Which memsensor properties can be realised on the basis of memristive devices and sensor structures fabricated within this thesis?
In order to give a thorough answer, a memsensor model relying on multistack nanoparticle-based memristive devices with diffusive switching characteristics is described in section 4.3.1.

How can further properties be realised by extending the choice of materials?
For this purpose, a more general memsensor model relying on idealised memristive devices with analog, multilevel switching is investigated in section 4.3.2.

Which general layout could be chosen for the preparation of a thin film stack memsensor?
In the context of this question, a simple thin film layout with a high prospect for a memsensor realization is proposed in section 4.3.3.

4.3.1 Modelling of Memsensors Relying on Nanoparticle-based Memristive Devices

In this section, the junction of nanoparticle-based memristive devices (with their diffusive memristive switching characteristics as depicted in Figure 44 a+b) and typical sensors (with an exponential response to a stimulus change as depicted in Figure 44 c) is explored in the framework of memsensors. For this purpose, first the IV characteristics of the individual components are modelled and subsequently the electrical properties of simple memsensor circuits are investigated on the basis of the developed models.

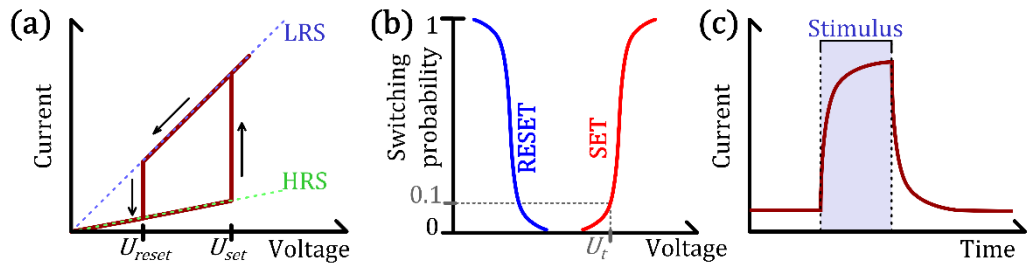

Figure 44: The characteristic feature of nanoparticle-based memristive devices is their diffusive memristive switching (a) with defined HRS and LRS and a stable operation window in between the SET and RESET voltages. These voltages are statistically distributed (b), which is described by the cumulative switching probability plot. In this section, the junction of such multistack memristive devices and typical sensor devices with an exponential current response (c) will be modelled in order to explore their applicability in the context of memsensors.

Modelling of nanoparticle-based memristive devices with diffusive switching characteristics

The characteristic feature of the nanoparticle-based memristive device is its diffusive memristive switching (as depicted in Figure 44 a) with the two distinct resistance states (HRS and LRS) and a stable operation window between the SET voltage (U_{set}) and the RESET voltage (U_{reset}). For consecutive switching cycles, the corresponding switching voltages are distributed statistically, as depicted in Figure 44 b.

In order to model the electrical characteristics of such nanoparticle-based memristive device, a numeric model applying the following assumptions was chosen:

> The memristive device exhibits two distinct resistance states, namely a state with high resistance $R_{m,HRS}$ and a state with low resistance $R_{m,LRS}$. This binary condition is expressed in terms of an internal state variable ω by Eq.4.1:
>
> (4.1) $$R_m(\omega) = R_{m,HRS} - \omega \cdot \left(R_{m,HRS} - R_{m,LRS}\right) \qquad \text{with} \qquad \omega \in \{0,1\}$$
>
> The switching between the respective resistance state is mediated by the voltage, which is applied to the memristive device. The probability of switching is a function of the applied voltage and the respective probability values are extracted from the probability plots, which were recorded based on the evaluation of multiple switching cycles for the multistack AgAu NP and AgPt NP devices.

In the numerical simulation, in each time step the internal state variable of the memristive device is updated by generating a random number (e.g. between 0 and 1) and comparing it to the respective switching probability at the applied voltage. This is illustrated by the following example: The memristive element is in its HRS and subjected to a voltage U_t. Following the switching probability plot in Figure 44 b, the switching probability at U_t is 0.1. Accordingly, the memristive element is SET to its LRS if the random number is below or equal to 0.1, otherwise it remains in its HRS. Accordingly, the switching between HRS and LRS is modelled to occur immediately in a single simulation step.

A single time step is related to 200 ms, which corresponds to a typical acquisition time for a single data point during the electrical measurement of the multistack devices.

In order to validate the model, the experimentally obtained resistance values and switching voltage distributions for the multistack AgAu NP device as well as for the AgPt NP device were incorporated into the model and multiple consecutive hysteresis loops were simulated. In Figure 45, the IV characteristics of the nanoparticle-based devices are depicted in terms of a comparison of experimentally measured hysteresis loops (grey lines) and simulated curves (red lines).

In case of the multistack AgAu NP device, the switching behaviour for the SET process is matched very accurately by the probabilistic model and also the RESET process is qualitatively well matched. The main deviation between the experimentally obtained and the simulated curves is found shortly before the RESET occurs. In the model, all switching processes are assumed to occur immediately in a single time step. In case of the SET step in the AgAu NP device, this assumption is well met, the RESET however occurs more gradual. Nevertheless, the simple model fits reasonably well to the experimental data.

The comparison of the experimentally obtained and the modelled IV hysteresis curves for the AgPt NP device is depicted in Figure 45 b. For the multistack AgPt NP device, the main switching characteristics are in general qualitatively captured by the model. However, the experimentally recorded IV hysteresis curves exhibit a more gradual switching, i.e. in addition to the HRS and LRS also further intermediate resistance states are occasionally observed. As the probabilistic model explicitly relies on a binary transition between $\omega=0$ and $\omega=1$, such gradual switching is not reproduced by the chosen model. In addition, the modelled IV hysteresis loops show a strong deviation from the experimentally obtained data in case the multistack AgPt NP device is in its HRS. More precisely, the experimentally determined current in the HRS lies in the range of 10 pA, while for the modelled data much smaller currents are observed. The main reason for these deviations is that the limit of detection of the applied measurement unit (Source meter, Keithley 2400) in connection with the probe station lies in the range of 10 pA. Another deviation between the simulated and experimentally recorded curves is to be found in the low resistance state of the diffusive memristive device. While the model assumes a constant ohmic resistance of the device (with two distinct resistance states), the experimental measurements of the nanoparticle-based

devices have shown deviations from ohmic conductivity in the LRS. As already discussed in the context of power exponent plots in section 4.1.4, the dominating conductivity mechanism in the LRS is not purely ohmic conduction, but indications for additional influences of space-charge limited conduction (in case of the AgAu NP device) and Poole-Frenkel emission (in case of the AgPt NP device) have been observed.

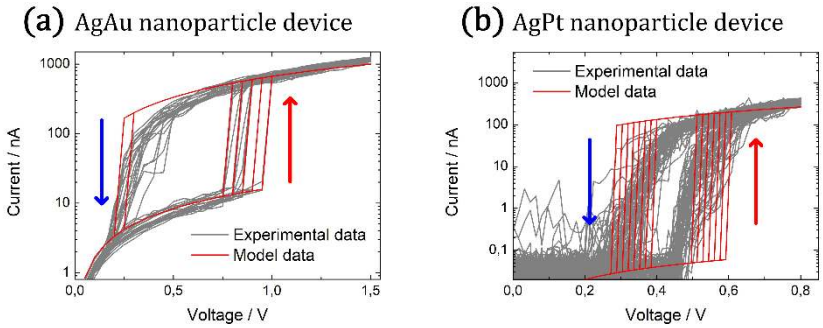

Figure 45: Comparison of the IV characteristics for multistack nanoparticle-based memristive devices obtained experimentally (grey lines) and from the probabilistic model (red lines). Especially in case of the AgAu NP multistack device (a), the SET and RESET processes are represented very well by the chosen model. The general switching behaviour of the AgPt NP device (b) is also reproduced by the model, but deviations especially in the HRS are observed.

However, despite the discussed built-in limitations of the chosen probabilistic model, the experimentally obtained hysteresis loops are qualitatively described reasonably well by the model, which allows to incorporate this model to the discussion of simple memsensor circuits.

Modelling of sensor devices

Representative for a variety of sensors investigated in the framework of this thesis, the response of a ZnO microrod sensor towards UV stimuli was selected to be modelled. This type of sensor relies on a ZnO microrod with a diameter of roughly 13 µm and a length of several mm. In Figure 46 a the general dimensions of the sensor are shown in terms of a top view SEM micrograph.

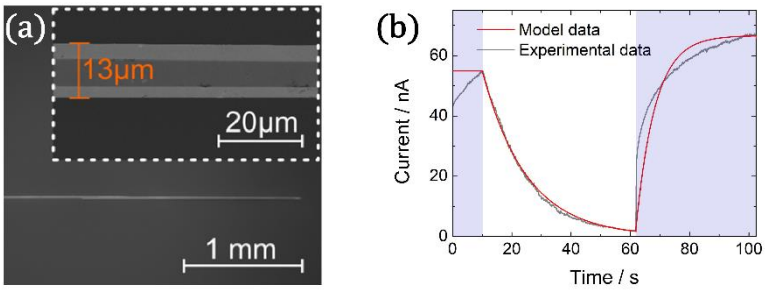

Figure 46: (a) SEM micrographs of a ZnO microrod sensor for detection of UV light. The inset shows that the microrod has a diameter of roughly 13 µm. Figure taken from [128]. (b) The current response of the ZnO sensor to a UV stimulus pulse (blue background represents the presence of UV illumination) is depicted as experimentally obtained (grey line) and as modelled (red line). Modelling started at the time of UV stimulus withdrawal (roughly at 10 s).

Full details on the fabrication and electrical properties of a ZnO microrod sensor are published in the following work:

> **A. Vahl**, J. Carstensen, S. Kaps, O. Lupan, T. Strunskus, R. Adelung, F. Faupel, *Concept and modelling of memsensors as two terminal devices with enhanced capabilities in neuromorphic engineering*, Scientific Reports. 9 (2019) 4361. doi: 10.1038/s41598-019-39008-5.

The typical behaviour of a sensor towards a stimulus pulse is the sharp increase of the current through the sensor, followed by an asymptotic saturation towards a maximum current I_{max}. Upon withdrawal of the stimulus, the sensor current sharply decreases until it asymptotically saturates at a minimum current I_{min}. In close relation to the terminology applied for memristive devices, the minimum and maximum current can be described as the sensor being in its HRS and LRS respectively.

In the numeric model, the sensor current is calculated for each time step (i+1) based on the previous step (i). In Eq.4.2, the sensor current I_s is expressed for the transition from HRS to LRS and vice versa. Here, the transition HRS to LRS corresponds to the presence of a UV stimulus and consequently an increase in sensor current (with response time τ_{res}), while LRS to HRS corresponds to the absence of a UV stimulus and a decrease in sensor current (with recovery time τ_{rec}).

$$I_{s,i+1} = \begin{cases} I_{s,max} - \left(I_{s,max} - I_{s,i}\right) \cdot \exp\left(\dfrac{-t}{\tau_{res}}\right) & \text{for HRS} \rightarrow \text{LRS} \\ \left(I_{s,i} - I_{s,min}\right) \cdot \exp\left(\dfrac{-t}{\tau_{rec}}\right) + I_{s,min} & \text{for LRS} \rightarrow \text{HRS} \end{cases} \tag{4.2}$$

In analogy to the resistance state of the memristive device, the resistance state of the sensitive device can be expressed in terms of a state variable α by Eq.4.3:

$$R_s(\alpha) = R_{s,HRS} - \alpha \cdot \left(R_{s,HRS} - R_{s,LRS}\right) \qquad \text{with} \qquad \alpha = \frac{R_{s,HRS} - \dfrac{U_{in}}{I_s}}{R_{s,HRS} - R_{s,LRS}} \tag{4.3}$$

The time constants for response and recovery as well as the values for the high and low resistance states are extracted from experimental data obtained for the ZnO microrod sensor. In Figure 46 b the measured response (grey curve) is compared to the simulated response to a stimulus pulse (red curve). In the latter case, the simulation starts with a constant current (first 10 s), followed by the withdrawal of UV light (white background) and the application of UV stimulus (blue background). In general, the qualitative features of the sensor response and recovery are well represented by the simulated curve. Especially for the recovery in the absence of the UV stimulus the model captures the experimental data very well. In case of the response of the sensor in the presence of a UV stimulus, the modelled curve deviates from the experimental data, especially with respect to the slope of the curve. In a more

refined model, the incorporation of a second time constant for the response would fit the experimental data more precisely.

Nevertheless, the sensor model even with a single time constant is very well suited to describe qualitatively the sensor behaviour and as such can be used for being integrated into the simulation of the equivalent circuit.

Exploring memsensor functionalities

Having validated the model for the sensor and for the nanoparticle-based diffusive memristive device, the next paragraph will focus on the description of memsensor circuits relying on these components.

First of all, the current response of a single sensor element, which is operated at constant applied voltage U_m, is investigated. In Figure 47 a, the simulated response of a sensor towards an external stimulus with low, medium and high stimulus strength are compared. Essentially, the variation in stimulus strength is realised by an alteration of the LRS of the sensor and reflects in a higher current response for increasing stimulus strength. These response and recovery characteristics are common for a sensor being subjected to stimuli of different strengths.

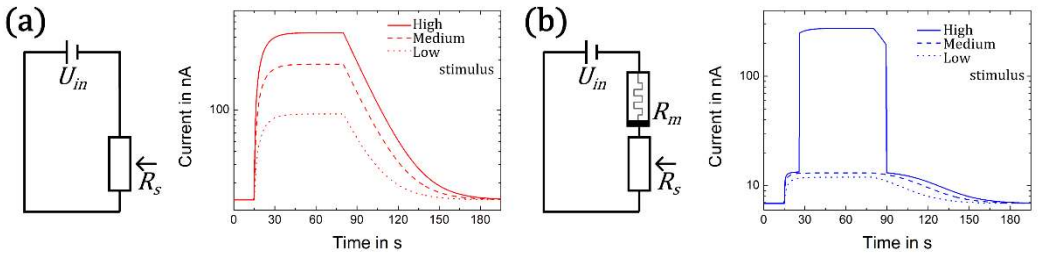

Figure 47: (a) Current response of a modelled sensor subjected to a single stimulus pulse of various strengths. (b) Current response of a serial connection of a sensor and a modelled memristive device with diffusive switching characteristics. In contrast to the response of the individual sensor, the latter memsensor circuit shows relay-like response to sufficiently high stimuli, while the response to subthreshold stimuli is effectively damped.

In the next step, the modelled circuit is expanded by an additional diffusive memristive element in series to the aforementioned sensor. The respective current response of such memsensor circuit to a stimulus pulse is depicted in Figure 47 b. In comparison to the behaviour of the individual sensor, the current response of the memsensor circuit is significantly altered and can be described as follows:

- For subthreshold stimuli (low and medium stimulus in Figure 47 b), the addition of the memristive element effectively leads to a damping of the overall current response, because the memristive device remains in its HRS and greatly increases the overall resistance of the memsensor circuit.

- For the high stimulus case, the resistance of the sensor element is lowest. In a serial connection with constant applied voltage, the potential drop over the respective

element is given by the fraction of its resistance with respect to the total resistance. Thus, in case the resistance of the sensor is sufficiently low, the potential drop over the memristive element reaches its SET voltage. Consequently, the memristive device switches to its LRS, which significantly reduced the overall resistance of the memsensor circuit. This sudden memristive switching is the origin of the abrupt increase in current response as observed for high stimulus strength in Figure 47 b.

In other words, the two-component circuit acts like a sensor with built-in threshold and the response to subthreshold signals is effectively reduced. This feature is particularly interesting in the context of neuromorphic engineering, because it closely resembles the suppression of response towards subthreshold stimuli in neuron assemblies. Based on the modelled memsensor behaviour, a combination of sensors and nanoparticle-based memristive devices as fabricated in this thesis appears very promising to obtain a memsensor with tailorable stimulus threshold.

In order to explore further memsensor properties, the two component memsensor circuit is extended by addition of a second sensor element (with identical characteristics compared to the first one) in parallel to the memristive element. The corresponding equivalent circuit is depicted in Figure 48 a. Assuming a constant applied voltage U_{in}, the potential drop over the memristive element U_m in such memsensor circuit is given by:

$$U_m = U_{in} \cdot \frac{\frac{R_m \cdot R_s}{R_m + R_s}}{R_s + \frac{R_m \cdot R_s}{R_m + R_s}} \tag{4.4}$$

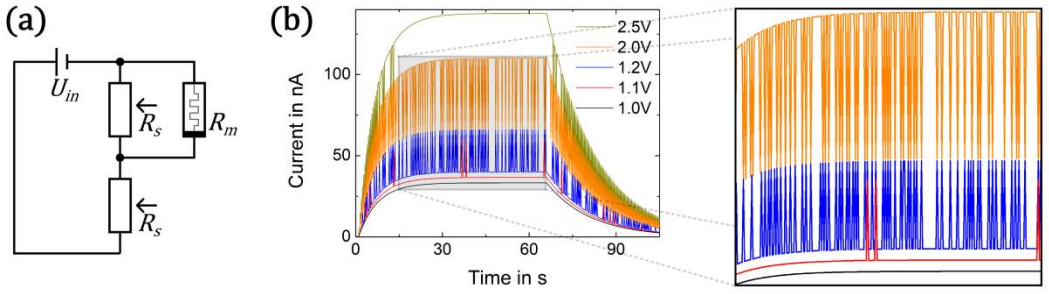

Figure 48: (a) Equivalent circuit of a memsensor with two identical sensor elements (with R_s) and a memristive element with diffusive memristive switching characteristics. Assuming an immediate binary switching between the memristive device's HRS and LRS, a transition region with continuous switching between both states can be observed for different applied voltages (b). The inset represents a magnified view on the most interesting area (grey rectangle) of the graph.

The main idea behind the incorporation of an additional sensor element is the following: In general, the memristive element exhibits binary diffusive switching with a stable operation windows between SET and RESET voltages. Within the described memsensor circuit, the memristive element can be brought into a condition where neither the LRS nor HRS are stable. Under the assumption of immediate switching, the individual switching events would

result in sharp, spike-like transitions in the current response. Considering the width of the distribution of switching voltages, the frequency of the spikes could be tailored by the applied voltage or stimulus. Similar to the two-component memsensor discussed previously, the three-component memsensor is modelled with respect to its response towards a single stimulus pulse. In the numeric simulation, the applied stimulus pulse started at 1 s and lasts 65 s.

First, the behaviour of such memsensor circuit to a single stimulus pulse at different applied voltages U_{in} is discussed. In this case, the model for the multistack AgPt NP memristive device and the ZnO microrod sensor were incorporated into the numerical simulation. The resulting simulated curves for five different input voltages (ranging from 1.0 V to 2.5 V) are depicted in Figure 48 b.

1.0 V: At low input voltages, the potential drop over the memristive element is well below the threshold for switching towards the LRS, independent of the resistance of the sensor elements. Accordingly, the memristive device remains in its HRS. The overall memsensor response resembles the behaviour observed for the ZnO microrod sensor.

1.1 V: The threshold voltage for switching from HRS to LRS is overcome as soon as the resistance of the sensor is lowered due to the stimulus. Following the probability for switching from HRS to LRS, the memristive device occasionally switches to its LRS. As soon as the memristive element is in its LRS, the overall resistance of the parallel sub-circuit is dominated by the low resistance of the memristive device. Accordingly, the potential drop over the memristive element is greatly reduced. In case of the diffusive memristive device, the LRS is only stable for sufficiently large voltages. Consequently, after the SET the device would immediately switch back to the HRS. This instability in the LRS of the memristive device is observed as "spike" in the current response of the memsensor.

1.2 V: The number of spikes (and accordingly switching events) increases. This is explained by the higher voltage at the memristive element in the HRS, which increases the switching probability. The LRS of the memristive device however is still unstable and after each switching event, the device switches back to its HRS.

2.0 V: The potential drop over the memristive element in its LRS is close to the RESET voltage. Accordingly, the memristive device may remain in the LRS for multiple simulation steps, which elongates the width of the individual spikes.

2.5 V: For sufficiently high voltages, the memristive device is stable in its LRS as long as the resistance of the sensor elements is low. Accordingly, between 20 s and 70 s no switching event is observed in the simulation of the memsensor response.

In general, the observed dependency of the memsensor current response can be summarised into three different regimes, which are schematically depicted with respect to the switching probability plot for the memristive element in Figure 49.

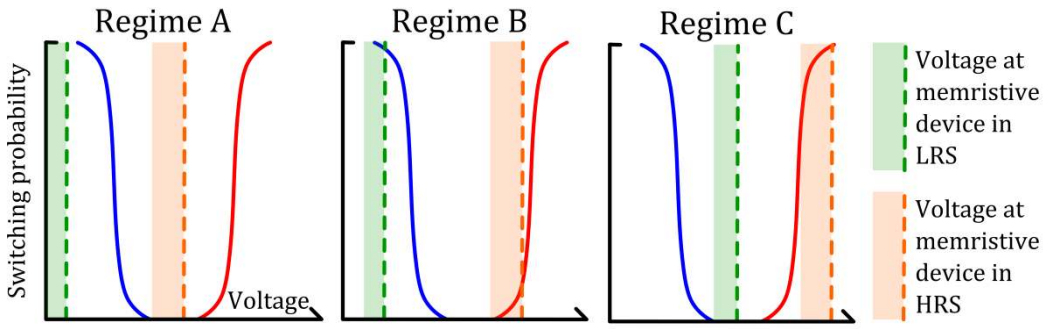

Figure 49: Schematic depiction of the three relevant memsensor regimes in terms of the voltage at the memristive device and its relation to the probability plot for SET (red curve) and RESET (blue curve). The voltage at the memristive device in its LRS and HRS are indicated by green and orange colour respectively.

Regime A: There is a regime, where the simulated three component memsensor circuit behaves like a typical sensor. Upon applying or removing the stimulus, the current asymptotically settles to its LRS or HRS. This condition is fulfilled, as long as the voltage at the memristive device is below the threshold voltage for SET switching, thus the memristive device remains in its HRS.

Regime B: This regime is characterised by the instability of the resistance states of the memristive element. In case the memristive element is in its HRS, the potential drop over the memristive element (orange area) lies within the range of SET voltages, which results in a switching of the memristive element to its LRS. As a result, after any switching event the current level rises due to the lower overall resistance of the memsensor circuit. In case the memristive element is in its LRS, the potential drop over the memristive element (green area) is below the RESET threshold, resulting in a RESET to the HRS. Accordingly, the overall resistance of the memsensor circuit is increased, which results in a drop in the current response. Under the assumption of immediate binary switching, such cycle of HRS-LRS-HRS transitions of the memristive element results in a single spike in the current response. The rate of these spiking events is essentially given by the potential drop over the memristive element with respect to the distribution of switching voltages.

Regime C: The third regime is characterised by a stable switching of the memristive element to its LRS. In this regime, the potential drop over the memristive element is sufficiently high so that in case the memristive element is in its LRS (green area), the resistance state is stable and no RESET occurs.

The three regimes are not only accessible by a variation of the applied voltage U_{in}, but also by a variation of the strength of the stimulus, which is shown in Figure 50 b. In this example, the simulation is based on the model for the multistack AgAu NP device as memristive element and the ZnO microrod sensor as sensor element. The applied voltage was kept constant at 1.8 V. In order to represent different stimulus strengths, the LRS of the sensor was set to 5 MΩ (high stimulus), 10 MΩ (medium stimulus) or 20 MΩ (low stimulus) respectively. In case of the lowest stimulus (corresponding to 20 MΩ), memsensor is operated in Regime A. By increasing the stimulus (corresponding to 10 MΩ), the memsensor

is transitioning to Regime B, resulting in the observation of spikes in the current response. For even higher stimuli (corresponding to 5 MΩ), the memsensor is operated in Regime C. Accordingly, in such three-component memsensor circuit there is a connection between the applied stimulus and the occurrence of spikes in the current response and their respective frequency.

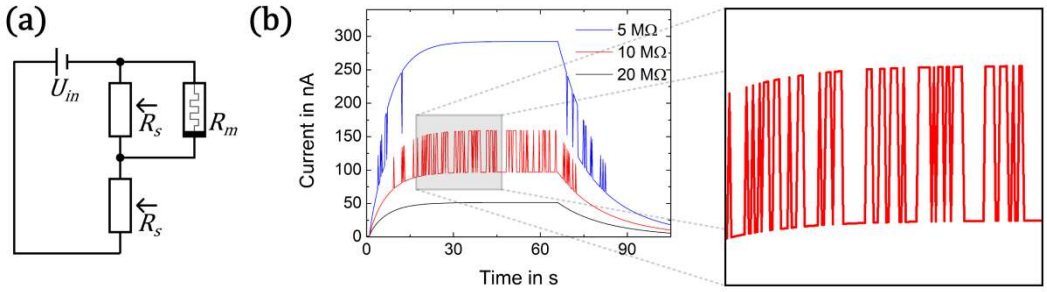

Figure 50: (a) Three component memsensor circuit with two identical sensor elements (with R_s) and a memristive element with diffusive memristive switching characteristics. Assuming an immediate binary switching between the memristive device's HRS and LRS, a transition region with continuous switching between both states can be observed for different stimulus strengths (b). The inset represents a magnified view on the most interesting area (grey rectangle) of the graph.

In conclusion, the simulation of memsensor circuits indicates the viability of incorporating nanoparticle-based memristive devices with diffusive switching characteristics in the context of memsensors. Especially Regime B appears to be very interesting for application purposes, e.g. as a memsensor with a spike-like current response towards UV stimuli in the context of neuromorphic engineering. However, the main limitation in the applied model for the memristive devices is the assumption of immediate binary switching. Experimentally, such behaviour is readily observed for the SET process in multistack nanoparticle-based memristive devices relying in AgAu NPs. Due to the experimental limitations with respect to the acquisition time in the range of 200 ms, further studies on the time-dependency of the switching process in nanoparticle-based memristive devices are necessary to give a reliable statement. However, even if the condition of immediate binary switching in multistack memristive devices will turn out not to be fully satisfied, the Regime B still renders interesting: In case there is a gradual, stepwise switching into additional intermediate resistance states, the instability of HRS and LRS in Regime B would allow to stabilise respective intermediate resistance states. As such, the memristive elements would behave more like a memristive devices with multilevel, analog switching characteristics.

4.3.2 Extension of the Memsensor Concept by Considering Multilevel Memristive Switching

The investigation of memsensor circuits so far was based on models for the memristive and sensor elements, which were in close relation to the devices fabricated in the framework of this thesis. In this section the concept of memsensors is extended to a more abstract model based on memristive elements with analog, multilevel switching characteristics (as schematically depicted in Figure 51 a). Such multilevel memristive switching was reported, e.g. by Jo et al., who investigated a thin film of amorphous Si with an embedded gradient of Ag NPs, formed by self-organization.[7] Furthermore, a sensor model with immediate response to the applied stimulus (as schematically shown in Figure 51 b) is chosen for the following simulations.

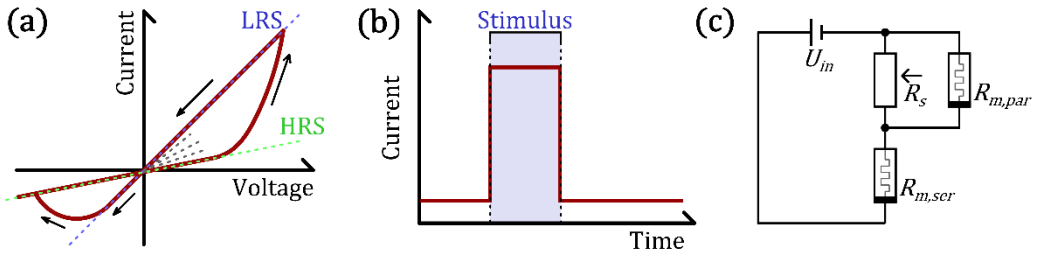

Figure 51: (a) The characteristic feature of a memristive device with multilevel, analog switching behaviour is the presence of a multitude of stable intermediate resistance states (grey, dotted lines) in addition to the global LRS and HRS. In this section, a model for analog memristive devices and a sensor model with immediate response to the applied stimulus (b) are chosen to investigate the electrical properties of a three-component memsensor circuit(c), which contains memristive elements in series ($R_{m,ser}$) and in parallel ($R_{m,par}$) to the sensing element (R_s).

In this section, a three-component memsensor circuit based on memristive elements in series (with $R_{m,ser}$) as well as in parallel (with $R_{m,par}$) to a sensitive element (with R_s) as shown in Figure 51 c will be investigated with respect to its response to the application and withdrawal of a stimulus. The main aspects of the memsensor modelling as well as the implications on the resulting memsensor properties are topic of this section while the full details are discussed in the following work:

> **A. Vahl**, J. Carstensen, S. Kaps, O. Lupan, T. Strunskus, R. Adelung, F. Faupel, *Concept and modelling of memsensors as two terminal devices with enhanced capabilities in neuromorphic engineering*, Scientific Reports. 9 (2019) 4361. doi: 10.1038/s41598-019-39008-5.

For a simple simulation of the proposed three component equivalent circuit, a perfect linear sensor is selected, whose resistance R_s depends linearly on the applied external stimulus α (Eq.4.5). Thus, the sensors resistance varies between its LRS and its HRS. Furthermore, the memristive elements' resistance is assumed to depend linearly on an internal state variable ω. As commonly used, for ω =0 the memristive element is in its HRS, for ω=1 it is in its LRS.

$$(4.5)\quad R_s\left(\alpha_{stim}\right) = R_{s,HRS} - \alpha \cdot \left(R_{s,HRS} - R_{s,LRS}\right) \qquad \text{with} \qquad \alpha = \left(\frac{\alpha_{stim}}{\alpha_{stim,\max}}\right)$$

$$(4.6)\quad R_m\left(\omega\right) = R_{m,HRS} - \omega \cdot \left(R_{m,HRS} - R_{m,LRS}\right) \qquad \text{with} \qquad \omega \in [0,1]$$

Both memristive elements are treated individually, each has an individual internal state variable ω_{ser} and ω_{par}. In order to model the change in resistivity, a voltage driven model in which the internal state of the memristive element is changed depending on the applied excitation potential U_m (Eq.4.7) is chosen. This approach is closely related to metal-cation-migration-based memristive devices (such as those presented in section 4.5.2) and is justified by the electrical-field-dependent ionisation and transport processes of charge carriers through insulating matrices.

$$(4.7)\quad \frac{\mathrm{d}\omega}{\mathrm{d}t} = \frac{U_m}{\tau}$$

A memristive element as described by Eq.4.7 would exhibit an infinite retention time of the resistance state. However, in real memristive devices there are always processes (such as dissolution of filaments by electromigration and diffusion) present that will drive the memristive device back to its original state. In this model these "backdriving forces" are expressed as a negative potential U_{back}, which counteracts the excitation potential. Although it is physically meaningful to assign different time constants (τ and τ_{back}) to the exciting and backdriving processes, for simulation purposes the number of free parameters can be reduced by transforming Eq.4.8 to Eq.4.9.

$$(4.8)\quad \frac{\mathrm{d}\omega}{\mathrm{d}t} = \frac{U_{ex}}{\tau} - \frac{U_{back}}{\tau_{back}}$$

$$(4.9)\quad \frac{\mathrm{d}\omega}{\mathrm{d}t} = \frac{U_{ex} - U_b}{\tau} \text{ with } U_b = U_{back}\frac{\tau}{\tau_{back}}$$

The excitation voltage for the parallel and serial memristive element results from the electrical equivalent circuit: Assuming an operation of the overall memsensor circuit at constant applied external voltage U_{in}, the potential drop over the serial ($U_{m,ser}$) and parallel ($U_{m,par}$) memristive element can be written as:

$$(4.10)\quad U_{m,ser} = U_{in} \cdot \frac{R_{m,ser}}{R_{m,ser} + \dfrac{R_{m,par} \cdot R_s}{R_{m,par} + R_s}}$$

$$U_{m,par} = U_{in} \cdot \frac{\dfrac{R_{m,par} \cdot R_s}{R_{m,par} + R_s}}{R_{m,ser} + \dfrac{R_{m,par} \cdot R_s}{R_{m,par} + R_s}} \tag{4.11}$$

According to the equivalent circuit, the overall resistance R of the three-component memsensor is described by the resistances of its components as written in Eq.4.12:

$$R = R_{m,ser}\left(\omega_{ser}\right) + \frac{R_{m,par}\left(\omega_{par}\right) \cdot R_s\left(\alpha\right)}{R_{m,par}\left(\omega_{par}\right) + R_s\left(\alpha\right)} \tag{4.12}$$

The next step in the development of the model is the formulation of the differential equation for the overall resistance. As already described in Eq.4.9, both memristive elements show a distinct time dependence regarding their internal state variable (and hence their resistance). Typical sensor devices also exhibit a time dependent response and recovery to applied stimuli. In this model however, the time dependence of the sensitive element is neglected, which is reasonable in case the time constants of the sensitive device are much smaller than the time constants of the memristive elements.

Based on this assumption, the full differential equation can be written as:

$$\begin{aligned} \frac{\mathrm{d}R}{\mathrm{d}t} = & -\frac{\mathrm{d}\omega_{ser}}{\mathrm{d}t} \cdot \left(R_{m,ser,HRS} - R_{m,ser,LRS}\right) \\ & + \frac{-\dfrac{\mathrm{d}\omega_{par}}{\mathrm{d}t} \cdot \left(R_{m,par,HRS} - R_{m,par,LRS}\right) \cdot R_s\left(\alpha\right)^2}{\left(R_{m,par,HRS} - \omega_{par} \cdot \left(R_{m,par,HRS} - R_{m,par,LRS}\right) + R_s\left(\alpha\right)\right)^2} \end{aligned} \tag{4.13}$$

For a numerical solution of this differential equation, the time derivative of both internal state variables (Eq.4.9) has to be discretized. In the discretized equation (Eq.4.14) the internal state variable at numerical simulation step i+1 depends on the earlier discussed potential drop over the respective memristive element as well as the previous state variable at step i.

$$\omega_{i+1} = \begin{cases} \omega_i + \dfrac{U_m - U_b}{\tau} & \text{for} \quad 0 \le \omega_i + \dfrac{U_m - U_b}{\tau} \le 1 \\ 1 & \text{for} \quad 1 < \omega_i + \dfrac{U_m - U_b}{\tau} \\ 0 & \text{for} \quad 0 > \omega_i + \dfrac{U_m - U_b}{\tau} \end{cases} \tag{4.14}$$

In addition, also the upper and lower boundaries for the state variable (1 and 0 respectively) are incorporated. Instead of including this necessity by adding two conditions for the upper

and lower boundary, also an appropriate window function could have been used. Window functions for memristive devices have already been proposed by Prodromakis et al. and Zha et al..[79,80] However, in this model the window function approach was not chosen in order to keep a simple representation of all parameters by physical quantities.

This three-component equivalent circuit model was applied in a numerical simulation of two application scenarios. Figure 52 shows the memsensor's behaviour towards IV hysteresis loops at various stimuli (a) as well as towards subsequent stimulus pulses at constant applied input voltage (b).

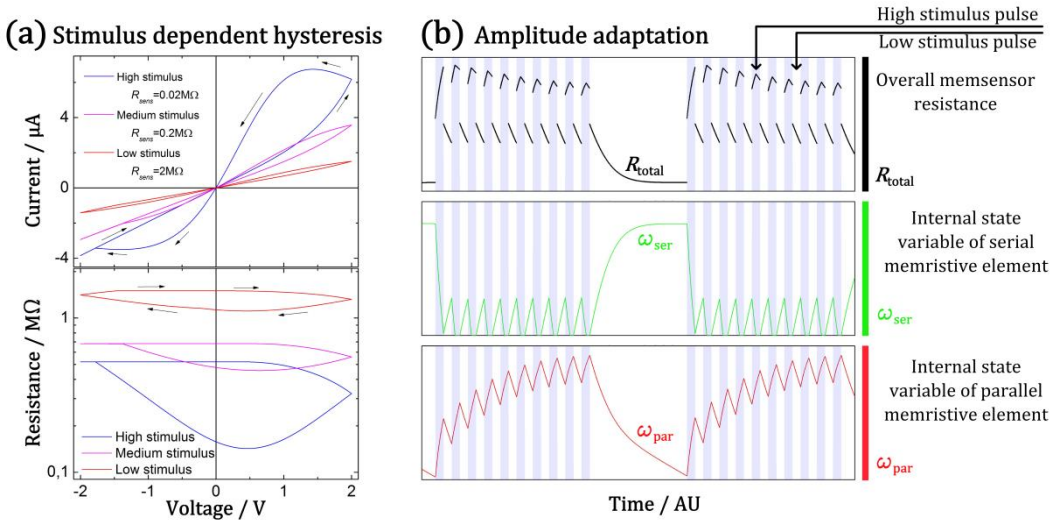

Figure 52: (a) Simulation of IV hysteresis for different stimulus levels applied at the sensory element; (b) The simulated response of a memsensor equivalent circuit to high and low stimulus pulses shows amplitude adaptation to consecutive stimulus pulses.

When the memsensor is subjected to a higher stimulus, the resistance of the sensor element and consequently also the resistance of the parallel sub-circuit is lowered. This results on the one hand in a lower overall resistance of the memsensor, which can be observed by comparing the blue and red curve in the R-V plot. On the other hand, the potential drop over the serial memristive element is relatively increased, which results in a more pronounced memristive switching. As a consequence, the width of the hysteresis loop is increased for higher stimulus strength. Thus, the extent of the IV hysteresis depends on the applied stimulus.

In case a sequence of stimulus pulses is applied to the memsensor at constant applied voltage, the response of the memsensor adapts to the applied stimulus. While for the first stimulus pulse, the amplitude of the change in resistance is the highest, with each subsequent pulse the amplitude decreases and gradually reaches a constant level of lower response. The origin of this amplitude adaptation lies in the interplay of the two memristive elements with analog memristive switching behaviour. While the serial memristive element (green colour) reacts fast and switches back to its HRS in each stimulus pulse, the parallel memristive element (red colour) gradually switches towards its LRS, which effectively results in the amplitude adaptation behaviour.

Both application scenarios offer high merits for applications in neuromorphic engineering: The stimulus dependent hysteresis for example would allow for selective memory state switching in a network. In a practical realisation, this could be used to manufacture a network of memory nodes, which can be written selectively by applying local optical signals. The amplitude adaptation of memsensors offers the potential of application as first layer of information processing, which processes the input stimuli and results in a sensitivity that is higher for abrupt changes than for gradual drift. Such memsensor device could close the gap between signal detection and processing, which is an essential feature for the design of biologically motivated circuits.

4.3.3 Conclusions for the Realization of a Thin Film Memsensor Device

In the previous chapters, memsensor circuits were modelled and the overall description of memsensors was quite abstract. A common feature of the described memsensor circuits is that each circuit incorporates one or more sensitive and memristive elements. In this section, the link between the modelled memsensor circuits and a potential thin film realisation will be closed.

A prerequisite for any memsensor is its accessibility to the external stimulus. In case of horizontal structures like nanowires, the memsensor is open to the surrounding and thus also any kind of sensory signal. For vertical structures, in which the active layer is sandwiched between two electrodes, integration into crossbar arrays is possible and was already demonstrated[23,129]. However, a structuring of the top electrode or a deliberate choice of top electrode material (e.g. ITO for transmission of optical stimuli) is mandatory in order to make the memsensor accessible to the external stimuli. For this reason, the simple design for a two-terminal memsensor discussed here relies on a thin film stack and lateral (horizontal) contacts. A schematic cross section of such memsensor stack is depicted in Figure 53.

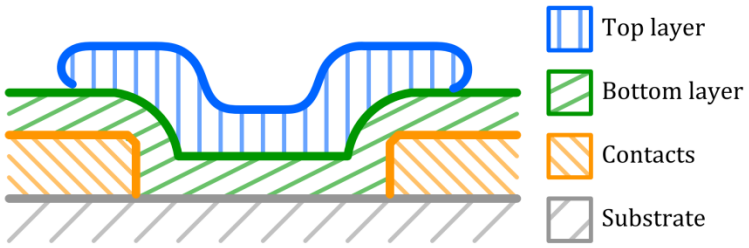

Figure 53: Schematic cross section of a thin film stack with the potential of resembling a memsensor. The drawing is not to scale.

Essentially, the memsensor stack contains four individual components: Onto a nonconductive substrate (grey colour) a metal contact layer (orange colour) with a lateral gap is applied, which is covered by a sequence of two layers (bottom layer: green colour, top layer: blue colour). Following this general scheme, the top layer is not covered by any contact or capping layer and thus is open to any stimulus. In Figure 54, the corresponding equivalent circuit under consideration of all possible interface and bulk resistances is shown.

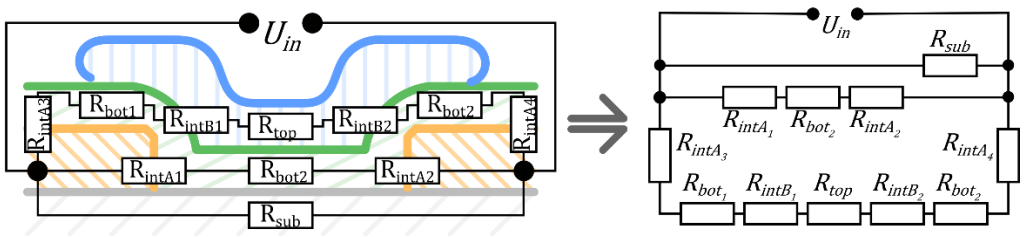

Figure 54: Schematic cross section of the proposed memsensor thin film stack including the depiction of the most relevant resistances.

This equivalent circuit can be substantially simplified to the dominating conduction path (Figure 55 a) using the following assumptions:

- In case an insulating substrate with sufficiently high resistivity (such as SiO_2) is chosen, the conduction through the substrate (with R_{sub}) can be neglected.
- In case the lateral gap between the contacts is much larger than the layer thickness of the bottom layer and the resistivity of the top layer material is lower than that of the bottom layer material, the conduction path through R_{bot2} can be neglected as $R_{bot2} >> (R_{bot1}+R_{bot3}+R_{top}+R_{intB1}+R_{intB2})$.

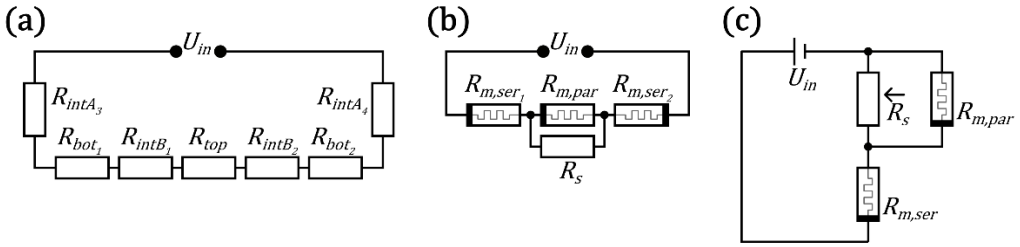

Figure 55: (a) Simplified equivalent circuit under the assumption that the dominating conduction path is through the top layer; (b) Corresponding equivalent circuit with memristive (R_m) and sensitive (R_s) elements; (c) Three-component memsensor circuit as discussed in section 4.3.2.

The general thin film stack layout allows combining two different thin films, one as the top layer and one as the bottom layer. The abstract two-terminal thin film memsensor stack can be put into the context of possible materials to be applied for the individual layers:

Because the top layer is well accessible by any kind of stimulus, this layer should incorporate the sensitive component. In the context of a potential application as top layer, materials such as semiconducting metal oxides appear very interesting, as they exhibit sensing properties towards UV-light and gas molecules as well as the potential to undergo memristive switching. Consequentially, the top layer itself could incorporate memristive and sensitive properties simultaneously. In the simplified equivalent circuit depicted in Figure 55 b, this corresponds to a memristive element (with $R_{m,par}$) in parallel to a sensitive element (with R_s). Assuming another memristive thin film to be applied as bottom layer, for example a nanoparticle-based memristive stack, two memristive elements (with $R_{m,ser1}$ and $R_{m,ser2}$) are added in series to the top layer. The resulting simplified equivalent circuit as shown in Figure 55 b exhibits strong similarities to the three-component memsensor circuit (Figure 55 c), which was discussed in terms of amplitude adaptation in the previous section. The usage of a nanoparticle-based memristive thin film as bottom layer offers the advantage that in principle similar memristive switching properties are observed independent of the applied polarity. For asymmetrical memristive devices (e.g. incorporating a Schottky-barrier), independent of the polarity one memristive element would always be operated under reverse bias. In this general layout, the lateral separation of the contacts directly relates to the resistance of the top layer R_{top}. Thus by deliberately choosing the width between the contacts, the resistance of the sensor R_s can be tailored. All in all, the two-layer thin film stack appears as a promising approach to fabricate two-terminal memsensor devices.

5. Conclusion and Outlook

This work evolves around the concept of memsensors, which unify the characteristic features of memristive devices and sensor devices. In terms of memsensor models, emerging features like amplitude adaptation are described and studied, and their close relation to stimulus response in biological neural assemblies renders memsensors as promising devices to be investigated in the context of neuromorphic engineering. On this background, the major objective of this thesis is to provide tools and building blocks and showcase pathways to incorporate memristive and sensitive properties into memsensor devices. For this purpose, a nanoparticle-based memristive device with diffusive memristive switching characteristics was developed and characterised in detail and sensors relying on semiconducting metal oxide thin films were studied.

Fabrication and characterization of memristive devices

In the framework of this thesis, memristive devices relying on noble metal alloy nanoparticles embedded in a dielectric matrix were successfully prepared and thoroughly characterised. The general concept of incorporating nanoparticles offers the advantage of field enhancement in between nanoparticles, predefining the location of memristive switching and yielding a more reproducible hysteresis loop while simultaneously omitting the necessity of electroforming. In this work, this overall design is expanded by using alloy nanoparticles with a well-defined composition, in which the less noble component acts as a source for the mobile metallic cations and the more noble component as a stable anchor inside the dielectric matrix. For the fabrication of AgAu and AgPt nanoparticles, the method of gas phase synthesis in a Haberland type gas aggregation source was extended by the introduction of a segmented target geometry. Upon utilizing Ag targets with embedded concentric wires made of Au or Pt, alloy nanoparticles with a narrow size distribution and mean diameters in the range of 10 nm were deposited from the gas phase. In addition, this single-target approach allows for a deliberate tailoring of the alloy nanoparticle composition by a variation of the operational pressure within the gas aggregation source.

These alloy nanoparticles were successfully incorporated into memristive nanocomposites, which were fabricated by sequential deposition of dielectric SiO_2 thin films and alloy nanoparticles. In order to study the electrical properties of such nanoparticle-based devices, single SiO_2/NP/SiO_2 stacks as well as multistack devices relying on multiple consecutively deposited SiO_2/NP stacks were prepared. The investigation of the memristive properties at the level of a single nanoparticle was realised by contacting individual nanoparticles with a conductive AFM tip. Reliable and reproducible diffusive memristive switching was observed with a statistical distribution of the respective switching voltages for multiple consecutive hysteresis loops. Multistack devices with a higher overall layer thickness (and consequentially a higher mechanical robustness) were contacted by flexible Pt wire in a conventional probe station. In agreement with the observations for contacting individual nanoparticles, the multistack memristive devices exhibit diffusive memristive switching with a stable operation window in between the switching voltages. As an example, in the AgAu NP multistack device no switching event was recorded in between 0.32 V (corresponding to

the RESET threshold) and 0.71 V (corresponding to the SET threshold), yielding an operation window width of 0.39 V.

The incorporation of a thin film of Cr as an additional wetting layer greatly impeded the overall device performance. In fact, in a two-day continuous c-AFM measurement, severe morphological changes in a range of several µm around the location of the tip were observed. Applying SEM EDX on the respective area, these structural alterations could be attributed to the migration and oxidation of Cr from the wetting layer, which indicates inferior long-term stability of the Cr wetting layer in the context of nanoparticle-based memristive devices.

The concept of multistack nanoparticle-based memristive devices turns out to be highly promising, as it allows for stable memristive switching with diffusive switching characteristics and a narrow distribution of the respective switching voltages. In comparison to other memristive devices with diffusive switching characteristics (such as the devices prepared by Wang et al., Nature Materials, 16 (2017) 101-108), the prepared multistack memristive devices relying on AgAu and AgPt nanoparticles are very competitive. The general concept of embedding alloy nanoparticles as a source for mobile silver cations into a dielectric matrix results in two degrees of freedom to design memristive devices with tailored switching properties: On the one hand, the composition of the nanoparticles and on the other hand the separation of the individual layers can be varied in order to impact the availability of mobile silver cations, the local electrical field and the overall resistance of the device. Considering this high versatility, the concept of memristive switching on the basis of noble metal alloy nanoparticles is very promising for future research on memristive devices.

Fabrication and characterization of sensor devices

Sensor devices relying on semiconducting metal oxide thin films were investigated with respect to their sensing performance towards UV-light and gas molecules. In general, two approaches were pursued in this context. First of all, the modification of sensing properties upon surface decoration with noble metal nanoparticles was investigated at the example of ZnO:Ag and ZnO:Fe thin film sensors. This approach shows a strong synergy with the deposition of alloy nanoparticles by gas phase synthesis, as already applied in the context of nanoparticle-based memristive devices. The surface decoration of the ZnO thin films with nanoparticles (Ag, AgAu and AgPt) results in a significant increase in sensitivity, which is related to a change in the electron depletion layer in the vicinity of the nanoparticles. For example, the gas response of a ZnO:Fe thin film towards ethanol was enhanced from 15 (for the pristine thin film) to 63 (for a thin film decorated with Ag nanoparticles). Simultaneously, the sensor exhibits only a minor response towards other gas species even at significantly higher concentrations, indicating a remarkable increase in ethanol-selectivity of such thin film sensors upon surface functionalization.

The second approach in the context of sensor devices was the deposition of thin films with tailored morphology by reactive DC magnetron sputtering. In this context, a special focus was put on the fabrication of nanocolumnar thin films. In case of TiO_2 thin films, a network of nanoscopic cracks was introduced to the thin film by a post deposition heat treatment. A variation in the availability of oxygen during the deposition was found to impact the resulting

thin film morphology. Applying a higher flow of oxygen results effectively in an enhancement in the nanocrack morphology with more defined cracks. This overall concept was transferred to the deposition of CuO thin films. In case of a high availability of oxygen, CuO thin films comprising of well separated columns with a high aspect ratio could be prepared even without the necessity of any post deposition heat treatment. An investigation of the gas sensing performance of a nanocolumnar CuO thin film sensor prototype showed response to H_2, n-butanol and 2-propanol with a change in resistivity of roughly 30% upon exposure towards the respective gas species.

In order to showcase the overall potential of combining the two concepts of tailored thin film morphology and surface decoration by nanoparticles, a thin film sensor device relying on nanocolumnar CuO thin films and AgAu nanoparticles was prepared. Upon surface decoration of the CuO thin film, the sensor exhibits a distinct change in selectivity: while the response to H_2 and n-butanol remained almost identical compared to the pristine CuO thin film, the gas response towards 2-propanol is enhanced roughly by a factor of 1.6. Although at first glance the sensor performance of the CuO/NP prototype appears inferior in comparison to the well-optimised doped ZnO thin film sensors, the possibility to deposit the semiconducting metal oxide thin film as well as alloy nanoparticles in a single PVD-based deposition step without the necessity of any heat treatment renders this approach very promising for further research on nanocomposite sensors.

Concept and modelling of memsensor devices

In the concept of memsensors, memristive and sensitive elements are combined in order to explore functionalities beyond the fundamental properties inherited from the individual components. The junction of sensing (stimulus dependent resistance = signal detection) and memristive switching (control over the resistance state = data processing) is in close analogy to signal detection and processing in biological systems. In order to study possible memsensor features such as adaptation, memsensor circuits are modelled and studied with respect to their electrical behaviour towards stimulus pulses.

The nanoparticle-based memristive devices with diffusive switching characteristics are modelled and combined with conventional sensors (ZnO microrods) in simple two- and three-component memsensor circuits. Biologically motivated functionalities such as a damping of the response towards subthreshold stimuli are observed in a numeric simulation of a memsensor featuring the serial connection of modelled nanoparticle-based memristive device and ZnO microrod sensor device. Upon the addition of a second sensor element to the memsensor circuit, in the numerical simulation an operational regime was observed, in which neither the LRS nor HRS of the diffusive memristive device were stable. Such regime renders very interesting for the operation of memsensor devices as (in the limits of the chosen model) it results in spike-like transitions in the current response.

The memsensor model was extended by considering memristive devices with idealised, analog, multilevel switching behaviour and a three-component memsensor circuit with two memristive elements, one in series and one in parallel to a sensitive element, is studied. In the simulation of such memsensor circuit, biologically motivated functionalities like

stimulus dependent hysteresis and amplitude adaptation are observed, which show a certain analogy to spike-frequency adaptation in neuron assemblies.

Outlook

In this early stage of research on memsensor devices, a reliable prediction of the range of applications in its entirety appears challenging and would go beyond the scope of this thesis. However, a short thought experiment will be employed to illustrate the tremendous application potential of memsensors:

> Take a sharp pencil and apply its tip with a mild, constant force onto your skin. As soon as the tip is touching your skin, you will feel a mild pain, reminding you of the pointy object. When you keep the force constant, slowly your skin adapts to the presence of the pencil and the mild pain vanishes from your consciousness.
>
> How does such behaviour relate to memsensors? Imagine an array of memsensors on a flexible polymer sheet, with the sensor component relying on mechanical sensing of a tactile stimulus. With carefully designed memsensors, in such array the individual device may adapt to the local stimulus and suppress any response to minor, subthreshold excitations. The memsensor array would react much like an artificial skin, with the built-in capability to detect and adapt to mechanical stimuli.

The short thought experiment illustrates the potential of memsensors to closely combine signal detection and data processing. This general concept exhibits strong parallels to signal processing in neuron assemblies. Consequently, memsensors appear as highly interesting research field in the context of biologically inspired devices in neuromorphic engineering. The minute combination of memristive and sensitive properties offers the chance to design two-terminal memsensors. In this respect, the general layout of thin film memsensor devices relying on a stack of sensitive and memristive layers and lateral contacts appears to be promising for further experimental studies on memsensors. Whether memsensor devices with integrated sensing and memristive switching capability will be able to live up to these promises will be essentially governed by the following aspects, which yield a broad field for further research:

- Will it be possible to manufacture memsensor devices with adequately narrow distribution of parameters?
- Will it be possible to integrate these devices into large scale networks with sufficient precision?
- Will the field of application be extended by realizing further emerging functionalities with memsensor devices?
- Will it be more efficient (in terms of energy and costs) to apply memsensor devices and arrays instead of a combination of conventional sensor arrays and signal processing electronics?

References

[1] J.J. Yang, D.B. Strukov, D.R. Stewart, Memristive devices for computing, Nat. Nanotechnol. 8 (2013) 13–24. doi:10.1038/nnano.2012.240.

[2] D.B. Strukov, G.S. Snider, D.R. Stewart, R.S. Williams, The missing memristor found., Nature. 453 (2008) 80–3. doi:10.1038/nature06932.

[3] D. Ielmini, Resistive switching memories based on metal oxides: Mechanisms, reliability and scaling, Semicond. Sci. Technol. 31 (2016) 063002–. doi:10.1088/0268-1242/31/6/063002.

[4] M.A. Zidan, J.P. Strachan, W.D. Lu, The future of electronics based on memristive systems, Nat. Electron. 1 (2018) 22–29. doi:10.1038/s41928-017-0006-8.

[5] A.H. Edwards, H.J. Barnaby, K.A. Campbell, M.N. Kozicki, W. Liu, M.J. Marinella, Reconfigurable Memristive Device Technologies, Proc. IEEE. 103 (2015) 1004–1033. doi:10.1109/JPROC.2015.2441752.

[6] F. Pan, S. Gao, C. Chen, C. Song, F. Zeng, Recent progress in resistive random access memories: Materials, switching mechanisms, and performance, Mater. Sci. Eng. R Reports. 83 (2014) 1–59. doi:10.1016/j.mser.2014.06.002.

[7] S.H. Jo, T. Chang, I. Ebong, B.B. Bhadviya, P. Mazumder, W. Lu, Nanoscale memristor device as synapse in neuromorphic systems., Nano Lett. 10 (2010) 1297–301. doi:10.1021/nl904092h.

[8] B.K. You, J.M. Kim, D.J. Joe, K. Yang, Y. Shin, Y.S. Jung, K.J. Lee, Reliable Memristive Switching Memory Devices Enabled by Densely Packed Silver Nanocone Arrays as Electric-Field Concentrators, ACS Nano. 10 (2016) 9478–9488. doi:10.1021/acsnano.6b04578.

[9] C. Minnai, A. Bellacicca, S.A. Brown, P. Milani, Facile fabrication of complex networks of memristive devices, (2017) 1–8. doi:10.1038/s41598-017-08244-y.

[10] C. Minnai, M. Mirigliano, S.A. Brown, P. Milani, The nanocoherer: an electrically and mechanically resettable resistive switching device based on gold clusters assembled on paper, Nano Futur. 2 (2018) 011002. doi:10.1088/2399-1984/aab4ee.

[11] S.G. Kim, J.H. Yoon, G.S. Kim, D.E. Kwon, K.J. Yoon, T.H. Park, C.S. Hwang, H.J. Kim, Y.J. Kwon, T.J. Ha, Y. Kim, W.M. Seong, J.W. Jeon, Fabrication of a Cu-Cone-Shaped Cation Source Inserted Conductive Bridge Random Access Memory and Its Improved Switching Reliability, Adv. Funct. Mater. 1806278 (2019) 1806278. doi:10.1002/adfm.201806278.

[12] T.J. Raeber, Z.C. Zhao, B.J. Murdoch, D.R. McKenzie, D.G. McCulloch, J.G. Partridge, Resistive switching and transport characteristics of an all-carbon memristor, Carbon N. Y. 136 (2018) 280–285. doi:10.1016/j.carbon.2018.04.045.

[13] Z. Wang, Q. Xia, J.J. Yang, R. Midya, Y. Li, Review of memristor devices in neuromorphic computing: materials sciences and device challenges, J. Phys. D. Appl. Phys. 51 (2018) 503002. doi:10.1088/1361-6463/aade3f.

[14] S.G. Kim, J.S. Han, H. Kim, S.Y. Kim, H.W. Jang, Recent Advances in Memristive Materials for Artificial Synapses, Adv. Mater. Technol. 3 (2018) 1–30. doi:10.1002/admt.201800457.

[15] M. Ignatov, M. Ziegler, M. Hansen, A. Petraru, H. Kohlstedt, A memristive spiking neuron with firing rate coding, Front. Neurosci. 9 (2015) 1–9. doi:10.3389/fnins.2015.00376.

[16] C.D. Wright, Precise computing with imprecise devices, Nat. Electron. 1 (2018) 212–213. doi:10.1038/s41928-018-0061-9.

[17] M.A. Zidan, Y. Jeong, W.D. Lu, Temporal Learning Using Second-Order Memristors, IEEE Trans. Nanotechnol. 16 (2017) 721–723. doi:10.1109/TNANO.2017.2710158.

[18] A. Dey, Semiconductor metal oxide gas sensors: A review, Mater. Sci. Eng. B Solid-State Mater. Adv. Technol. 229 (2018) 206–217. doi:10.1016/j.mseb.2017.12.036.

[19] W. Tian, H. Lu, L. Li, Nanoscale ultraviolet photodetectors based on onedimensional metal oxide nanostructures, Nano Res. 8 (2015) 382–405. doi:10.1007/s12274-014-0661-2.

[20] M. Ungureanu, R. Zazpe, F. Golmar, P. Stoliar, R. Llopis, F. Casanova, L.E. Hueso, A light-controlled resistive switching memory, Adv. Mater. 24 (2012) 2496–2500. doi:10.1002/adma.201200382.

[21] S. Carrara, D. Sacchetto, M.A. Doucey, C. Baj-Rossi, G. De Micheli, Y. Leblebici, Memristive-biosensors: A new detection method by using nanofabricated memristors, Sensors Actuators, B Chem. 171–172 (2012) 449–457. doi:10.1016/j.snb.2012.04.089.

[22] Z. Fan, X. Fan, A. Li, L. Dong, Nanorobotic in situ characterization of nanowire memristors and "memsensing," IEEE Int. Conf. Intell. Robot. Syst. (2013) 1028–1033. doi:10.1109/IROS.2013.6696477.

[23] C. Nyenke, L. Dong, Fabrication of a W/CuxO/Cu memristor with sub-micron holes for passive sensing of oxygen, Microelectron. Eng. 164 (2016) 48–52. doi:10.1016/j.mee.2016.07.005.

[24] A. Emboras, A. Alabastri, F. Ducry, B. Cheng, Y. Salamin, P. Ma, S. Andermatt, B. Baeuerle, A. Josten, C. Hafner, M. Luisier, P. Nordlander, J. Leuthold, Atomic Scale Photodetection Enabled by a Memristive Junction, ACS Nano. 12 (2018) 6706–6713. doi:10.1021/acsnano.8b01811.

[25] S. Gao, G. Liu, H. Yang, C. Hu, Q. Chen, An Oxide Schottky Junction Artificial Optoelectronic Synapse, ACS Nano. 13 (2019) 2634–2642. doi:10.1021/acsnano.9b00340.

[26] H. Ibach, H. Lüth, Solid-State Physics, 3rd ed., Springer-Verlag, Berlin Heidelberg, 2003.

[27] K.-N. Tu, J.W. Mayer, L.C. Feldman, Electronic Thin Film Science, 1st ed., Macmillan Publishing Company, New Yok, 1992.

[28] E. Lim, R. Ismail, Conduction Mechanism of Valence Change Resistive Switching Memory: A Survey, Electronics. 4 (2015) 586–613. doi:10.3390/electronics4030586.

[29] P. Mark, W. Helfrich, Space-Charge-Limited Currents in Organic Crystals, J. Appl. Phys. 33 (1962) 205–215. doi:10.1063/1.1728487.

[30] C. Acha, Graphical analysis of current-voltage characteristics in memristive interfaces, J. Appl. Phys. 121 (2017). doi:10.1063/1.4979723.

[31] Q. Kang, J. Cao, Y. Zhang, L. Liu, H. Xu, J. Ye, Reduced TiO2 nanotube arrays for photoelectrochemical water splitting, J. Mater. Chem. A. 1 (2013) 5766. doi:10.1039/c3ta10689f.

[32] L.O. Chua, Memristor—The Missing Circuit Element, IEEE Trans. Circuit Theory. 18 (1971) 507–519. doi:10.1109/TCT.1971.1083337.

[33] L.O. Chua, S.M. Kang, Memristive Devices and Systems, Proc. IEEE. 64 (1976) 209–223. doi:10.1109/PROC.1976.10092.

[34] Y. Hirose, H. Hirose, Polarity-dependent memory switching and behavior of Ag dendrite in Ag-photodoped amorphous As2S3films, J. Appl. Phys. 47 (1976) 2767–2772. doi:10.1063/1.322942.

[35] H.M. Upadhyaya, S. Chandra, Polarity-dependent memory switching effects in the Ti/CdxPb1-xS/Ag system, Semicond. Sci. Technol. 10 (1995) 332–338. doi:10.1088/0268-1242/10/3/016.

[36] M.. Jafar, D.. Hanemann, Switching in amorphous-silicon devices, Phys. Rev. B. 49 (1994). doi:10.1007/s13398-014-0173-7.2.

[37] R. Waser, M. Aono, Nanoionics-based resistive switching memories, Nat. Mater. 6 (2007) 833–840. doi:10.1038/nmat2023.

[38] G.W. Burr, B.N. Kurdi, J.C. Scott, C.H. Lam, K. Gopalakrishnan, R.S. Shenoy, Overview of candidate device technologies for storage-class memory, IBM J. Res. Dev. 52 (2008) 449–464. doi:10.1147/rd.524.0449.

[39] S. Vongehr, X. Meng, The Missing Memristor has Not been Found, Sci. Rep. 5 (2015) 1–7. doi:10.1038/srep11657.

[40] D.S. Jeong, R. Thomas, R.S. Katiyar, J.F. Scott, H. Kohlstedt, A. Petraru, C.S. Hwang, Emerging memories: resistive switching mechanisms and current status, Reports Prog. Phys. 75 (2012) 076502. doi:10.1088/0034-4885/75/7/076502.

[41] X.L. Hong, D.J.J. Loy, P.A. Dananjaya, F. Tan, C.M. Ng, W.S. Lew, Oxide-based RRAM materials for neuromorphic computing, J. Mater. Sci. 53 (2018) 8720–8746. doi:10.1007/s10853-018-2134-6.

[42] M.N. Kozicki, H.J. Barnaby, Conductive bridging random access memory - Materials, devices and applications, Semicond. Sci. Technol. 31 (2016) 113001. doi:10.1088/0268-1242/31/11/113001.

[43] E. Linn, R. Rosezin, S. Tappertzhofen, U. Böttger, R. Waser, Beyond von Neumann—logic operations in passive crossbar arrays alongside memory operations, Nanotechnology. 23 (2012) 305205. doi:10.1088/0957-4484/23/30/305205.

[44] J. Van Den Hurk, V. Havel, E. Linn, R. Waser, I. Valov, Ag/GeS x /Pt-based complementary resistive switches for hybrid CMOS/Nanoelectronic logic and memory architectures, Sci. Rep. 3 (2013) 2–6. doi:10.1038/srep02856.

[45] M. V. Il'ina, O.I. Il'in, Y.F. Blinov, V.A. Smirnov, A.S. Kolomiytsev, A.A. Fedotov, B.G. Konoplev, O.A. Ageev, Memristive switching mechanism of vertically aligned carbon nanotubes, Carbon N. Y. 123 (2017) 514–524. doi:10.1016/j.carbon.2017.07.090.

[46] L.A. Jauregui, Organic memristors come of age, Nat. Mater. (2018). doi:10.1038/nmat5014.

[47] J. Sun, Y. Fu, Q. Wan, Organic synaptic devices for neuromorphic systems, J. Phys. D. Appl. Phys. 51 (2018) 314004. doi:10.1088/1361-6463/aacd99.

[48] M. Hosomi, H. Yamagishi, T. Yamamoto, K. Bessho, Y. Higo, K. Yamane, H. Yamada, M. Shoji, H. Hachino, C. Fukumoto, H. Nagao, H. Kano, A novel nonvolatile memory with spin torque transfer magnetization switching: spin-ram, IEEE Int. Devices Meet. 2005. IEDM Tech. Dig. 00 (2005) 459–462. doi:10.1109/IEDM.2005.1609379.

[49] R.L. Stamps, S. Breitkreutz, J. Åkerman, A. V. Chumak, Y. Otani, G.E.W. Bauer, J.U. Thiele, M. Bowen, S.A. Majetich, M. Kläui, I.L. Prejbeanu, B. Dieny, N.M. Dempsey, B. Hillebrands, The 2014 Magnetism Roadmap, J. Phys. D. Appl. Phys. 47 (2014). doi:10.1088/0022-3727/47/33/333001.

[50] I. Valov, Interfacial interactions and their impact on redox-based resistive switching memories (ReRAMs), Semicond. Sci. Technol. 32 (2017) 093006. doi:10.1088/1361-6641/aa78cd.

[51] S. Dirkmann, Modellierung und Simulation memristiver Bauteile, Ruhr-Universität Bochum, 2018.

[52] R. Waser, R. Bruchhaus, S. Menzel, Redox-based Resistive Switching Memories, in:

R. Waser (Ed.), Nanoelectron. Inf. Technol. Adv. Electron. Mater. Nov. Devices, 3rd ed., Wiley-VCH, 2012: pp. 683–710.

[53] R. Dittmann, Valence Change in Nanoionic Oxide Cells, in: R. Waser, M. Wuttig (Eds.), Memristive Phenom. - From Fundam. Phys. to Neuromorphic Comput., 1st ed., Forschungszentrum Jülich GmbH, Jülich, 2016: pp. 701–725.

[54] K. Szot, W. Speier, G. Bihlmayer, R. Waser, Switching the electrical resistance of individual dislocations in single-crystalline $SrTiO_3$, Nat. Mater. 5 (2006) 312–320. doi:10.1038/nmat1614.

[55] M. Hansen, M. Ziegler, L. Kolberg, R. Soni, S. Dirkmann, T. Mussenbrock, H. Kohlstedt, A double barrier memristive device, Sci. Rep. 5 (2015) 13753. doi:10.1038/srep13753.

[56] S. Dirkmann, M. Ziegler, M. Hansen, H. Kohlstedt, J. Trieschmann, T. Mussenbrock, Kinetic simulation of filament growth dynamics in memristive electrochemical metallization devices, J. Appl. Phys. 118 (2015) 214501. doi:10.1063/1.4936107.

[57] S. Dirkmann, M. Hansen, M. Ziegler, H. Kohlstedt, T. Mussenbrock, The role of ion transport phenomena in memristive double barrier devices, Sci. Rep. 6 (2016) 1–12. doi:10.1038/srep35686.

[58] I. Valov, Electrochemical Metallization Memories, in: R. Waser, M. Wuttig (Eds.), Memristive Phenom. - From Fundam. Phys. to Neuromorphic Comput., 1st ed., Forschungszentrum Jülich GmbH, Jülich, 2016: pp. 677–699.

[59] A. Wedig, M. Luebben, M. Moors, D.Y. Cho, K. Skaja, T. Hasegawa, K.K. Adepalli, B. Yildiz, R. Waser, I. Valov, Nanoscale cation motion in TaOx, HfOx and TiOx memristive systems, Nat. Nanotechnol. 11 (2015) 67–74. doi:10.1038/nnano.2015.221.

[60] Y. Sun, M. Tai, C. Song, Z. Wang, J. Yin, F. Li, H. Wu, F. Zeng, H. Lin, F. Pan, Competition between Metallic and Vacancy Defect Conductive Filaments in a $CH_3NH_3PbI_3$-Based Memory Device, J. Phys. Chem. C. 122 (2018) 6431–6436. doi:10.1021/acs.jpcc.7b12817.

[61] N.F. Mott, R.W. Gurney, Electronic Processes in Ionic Crystal, 2nd Editio, Oxford University Press, Oxford, 1950.

[62] S. Menzel, Switching Kinetics of Redox-based Resistive Memories, in: R. Waser, M. Wuttig (Eds.), Memristive Phenom. - From Fundam. Phys. to Neuromorphic Comput., 1st ed., Forschungszentrum Jülich GmbH, Jülich, 2016: pp. 727–745.

[63] D. Mahalanabis, H.J. Barnaby, M.N. Kozicki, V. Bharadwaj, S. Rajabi, Investigation of Single Event Induced Soft Errors in Programmable Metallization Cell Memory, IEEE Trans. Nucl. Sci. 61 (2014) 3557–3563. doi:10.1109/TNS.2014.2358235.

[64] D. Mahalanabis, V. Bharadwaj, H.J. Barnaby, S. Vrudhula, M.N. Kozicki, A nonvolatile sense amplifier flip-flop using programmable metallization cells, IEEE J. Emerg. Sel. Top. Circuits Syst. 5 (2015) 205–213. doi:10.1109/JETCAS.2015.2433571.

[65] Y. Yang, P. Gao, S. Gaba, T. Chang, X. Pan, W. Lu, Observation of conducting filament growth in nanoscale resistive memories, Nat. Commun. 3 (2012) 732–738. doi:10.1038/ncomms1737.

[66] K.K. Neelisetty, X. Mu, S. Gutsch, A. Vahl, A. Molinari, F. von Seggern, M. Hansen, T. Scherer, M. Zacharias, L. Kienle, V.K. Chakravadhanula, C. Kübel, Electron Beam Effects on Oxide Thin Films—Structure and Electrical Property Correlations, Microsc. Microanal. (2019) 1–9. doi:10.1017/S1431927619000175.

[67] M. Lübben, S. Menzel, S.G. Park, M. Yang, R. Waser, I. Valov, SET kinetics of electrochemical metallization cells: Influence of counter-electrodes in SiO_2/Ag based systems, Nanotechnology. 28 (2017) 135205. doi:10.1088/1361-6528/aa5e59.

[68] S. Tappertzhofen, E. Linn, U. Bottger, R. Waser, I. Valov, Nanobattery effect in RRAMs-Implications on device stability and endurance, IEEE Electron Device Lett. 35 (2014) 208–210. doi:10.1109/LED.2013.2292113.

[69] T. Tsuruoka, K. Terabe, T. Hasegawa, I. Valov, R. Waser, M. Aono, Effects of Moisture on the Switching Characteristics of Oxide-Based, Gapless-Type Atomic Switches, Adv. Funct. Mater. 22 (2012) 70–77. doi:10.1002/adfm.201101846.

[70] T. Tsuruoka, I. Valov, S. Tappertzhofen, J. Van Den Hurk, T. Hasegawa, R. Waser, M. Aono, Redox Reactions at Cu,Ag/Ta2O5 Interfaces and the Effects of Ta2O5 Film Density on the Forming Process in Atomic Switch Structures, Adv. Funct. Mater. 25 (2015) 6374–6381. doi:10.1002/adfm.201500853.

[71] I. Valov, E. Linn, S. Tappertzhofen, S. Schmelzer, J. van den Hurk, F. Lentz, R. Waser, Nanobatteries in redox-based resistive switches require extension of memristor theory, Nat. Commun. 4 (2013) 1771. doi:10.1038/ncomms2784.

[72] C.C. Kuo, I.C. Chen, C.C. Shih, K.C. Chang, C.H. Huang, P.H. Chen, T. Chang, T.M. Tsai, J.S. Chang, J.C. Huang, Galvanic Effect of Au – Ag Electrodes for Conductive Bridging Resistive Switching Memory, 36 (2015) 1321–1324. doi:10.1109/LED.2015.2496303.

[73] W. Li, X. Liu, Y. Wang, Z. Dai, W. Wu, L. Cheng, Y. Zhang, Q. Liu, X. Xiao, C. Jiang, Design of high-performance memristor cell using W-implanted SiO2films, Appl. Phys. Lett. 108 (2016). doi:10.1063/1.4945982.

[74] B.J. Choi, A.C. Torrezan, K.J. Norris, F. Miao, J.P. Strachan, M.X. Zhang, D.A.A. Ohlberg, N.P. Kobayashi, J.J. Yang, R.S. Williams, Electrical performance and scalability of Pt dispersed SiO2 nanometallic resistance switch, Nano Lett. 13 (2013) 3213–3217. doi:10.1021/nl401283q.

[75] E. Linn, A. Siemon, R. Waser, S. Menzel, Applicability of well-established memristive models for simulations of resistive switching devices, IEEE Trans. Circuits Syst. I Regul. Pap. 61 (2014) 2402–2410. doi:10.1109/TCSI.2014.2332261.

[76] S. Menzel, U. Böttger, R. Waser, Simulation of multilevel switching in electrochemical metallization memory cells, J. Appl. Phys. 111 (2012). doi:10.1063/1.3673239.

[77] A. Ascoli, F. Corinto, V. Senger, R. Tetzlaff, Memristor model comparison, IEEE Circuits Syst. Mag. 13 (2013) 89–105. doi:10.1109/MCAS.2013.2256272.

[78] M.D. Pickett, D.B. Strukov, J.L. Borghetti, J.J. Yang, G.S. Snider, D.R. Stewart, R.S. Williams, Switching dynamics in titanium dioxide memristive devices, J. Appl. Phys. 106 (2009). doi:10.1063/1.3236506.

[79] T. Prodromakis, B.P. Peh, C. Papavassiliou, C. Toumazou, A versatile memristor model with nonlinear dopant kinetics, IEEE Trans. Electron Devices. 58 (2011) 3099–3105. doi:10.1109/TED.2011.2158004.

[80] J. Zha, H. Huang, T. Huang, J. Cao, A. Alsaedi, F.E. Alsaadi, A general memristor model and its applications in programmable analog circuits, Neurocomputing. 267 (2017) 134–140. doi:10.1016/j.neucom.2017.04.057.

[81] Y.N. Joglekar, S.J. Wolf, The elusive memristor: properties of basic electrical circuits, Eur. J. Phys. 30 (2009) 661–675. doi:10.1088/0143-0807/30/4/001.

[82] S. Benderli, T.A. Wey, On SPICE macromodelling of TiO2 memristors, Electron. Lett. 45 (2009) 377. doi:10.1049/el.2009.3511.

[83] Z. Biolek, D. Biolek, V. Biolková, SPICE Model of Memristor with Nonlinear Dopant Drift, Radioengineering. 18 (2009) 210–214.

[84] S. Shin, K. Kim, S.-M. Kang, Compact Models for Memristors Based on Charge-Flux

Constitutive Relationships, IEEE Trans. Comput. Des. Integr. Circuits Syst. 29 (2010) 590–598. doi:10.1109/TCAD.2010.2042891.

[85] N. Onofrio, D. Guzman, A. Strachan, Atomic origin of ultrafast resistance switching in nanoscale electrometallization cells, Nat. Mater. 14 (2015). doi:10.1038/nmat4221.

[86] A.R. Genreith-Schriever, R.A. De Souza, Field-enhanced ion transport in solids: Reexamination with molecular dynamics simulations, Phys. Rev. B. 94 (2016) 4–8. doi:10.1103/PhysRevB.94.224304.

[87] E. Solan, S. Dirkmann, M. Hansen, D. Schroeder, H. Kohlstedt, M. Ziegler, T. Mussenbrock, K. Ochs, An enhanced lumped element electrical model of a double barrier memristive device, J. Phys. D. Appl. Phys. 50 (2017). doi:10.1088/1361-6463/aa69ae.

[88] D. Li, M. Li, F. Zahid, J. Wang, H. Guo, Oxygen vacancy filament formation in TiO 2 : A kinetic Monte Carlo study, J. Appl. Phys. 112 (2012) 073512. doi:10.1063/1.4757584.

[89] B.C. Jang, Y. Nam, B.J. Koo, J. Choi, S.G. Im, S.H.K. Park, S.Y. Choi, Memristive Logic-in-Memory Integrated Circuits for Energy-Efficient Flexible Electronics, Adv. Funct. Mater. 28 (2018) 1–10. doi:10.1002/adfm.201704725.

[90] T. You, Y. Shuai, W. Luo, N. Du, D. Bürger, I. Skorupa, R. Hübner, S. Henker, C. Mayr, R. Schüffny, T. Mikolajick, O.G. Schmidt, H. Schmidt, Exploiting memristive BiFeO3 bilayer structures for compact sequential logics, Adv. Funct. Mater. 24 (2014) 3357–3365. doi:10.1002/adfm.201303365.

[91] A. Haj-Ali, R. Ben-Hur, N. Wald, R. Ronen, S. Kvatinsky, Not in Name Alone: A Memristive Memory Processing Unit for Real In-Memory Processing, IEEE Micro. 38 (2018) 13–21. doi:10.1109/MM.2018.053631137.

[92] E. Linn, A. Heittmann, From Memristive Gate-Array Logic to Neuromorphic Computing, in: R. Waser, M. Wuttig (Eds.), Memristive Phenom. - From Fundam. Phys. to Neuromorphic Comput., 1st ed., Forschungszentrum Jülich GmbH, Jülich, 2016: pp. 979–1021.

[93] Q. Xia, J.J. Yang, Memristive crossbar arrays for brain-inspired computing, Nat. Mater. 18 (2019) 309–323. doi:10.1038/s41563-019-0291-x.

[94] D.J. Wouters, Select Devices For Memristive Crossbar Arrays, in: R. Waser, M. Wuttig (Eds.), Memristive Phenom. - From Fundam. Phys. to Neuromorphic Comput., 1st ed., Forschungszentrum Jülich GmbH, Jülich, 2016: pp. 945–976.

[95] G.W. Burr, R.S. Shenoy, K. Virwani, P. Narayanan, A. Padilla, B. Kurdi, H. Hwang, Access devices for 3D crosspoint memory, J. Vac. Sci. Technol. B, Nanotechnol. Microelectron. Mater. Process. Meas. Phenom. 32 (2014) 040802. doi:10.1116/1.4889999.

[96] P. Cogez, M. Graef, B. Huizing, R. Mahnkopf, H. Ishiuchi, J. Shindo, S. Choi, J.H. Choi, C.H. Diaz, Y.C. See, B. Doering, P. Gargini, T. Kingscott, I. Steff, International Technology Roadmap for Semiconductors: 2012 Update Overview, (2012).

[97] E. Linn, S. Menzel, S. Ferch, R. Waser, Compact modeling of CRS devices based on ECM cells for memory, logic and neuromorphic applications, Nanotechnology. 24 (2013) 384008. doi:10.1088/0957-4484/24/38/384008.

[98] C. Mead, Neuromorphic Electronic Systems, Proc. IEEE. 78 (1990) 1629–1636. https://web.stanford.edu/group/brainsinsilicon/documents/MeadNeuroMorphElectro.pdf.

[99] S.H. Tan, P. Lin, H. Yeon, S. Choi, Y. Park, J. Kim, Perspective: Uniform switching of artificial synapses for large-scale neuromorphic arrays, APL Mater. 6 (2018) 120901. doi:10.1063/1.5049137.

[100] W. Gerstner, W. Kistler, Spiking neural models: single neurons, populations, plasticity, 2002.

[101] D. Ielmini, Brain-inspired computing with resistive switching memory (RRAM): Devices, synapses and neural networks, Microelectron. Eng. 190 (2018) 44–53. doi:10.1016/j.mee.2018.01.009.

[102] T. Chang, Y. Yang, W. Lu, Building Neuromorphic Circuits with Memristive Devices, IEEE Circuits Syst. Mag. 13 (2013) 56–73. doi:10.1109/MCAS.2013.2256260.

[103] K.A. Buchanan, J.R. Mellor, The activity requirements for spike timing-dependent plasticity in the hippocampus, Front. Synaptic Neurosci. 2 (2010) 1–5. doi:10.3389/fnsyn.2010.00011.

[104] G. Bi, M. Poo, Synaptic Modifications in Cultured Hippocampal Neurons: Dependence on Spike Timing, Synaptic Strength, and Postsynaptic Cell Type, J. Neurosci. 18 (1998) 1–9. doi:10.1523/JNEUROSCI.18-24-10464.1998.

[105] Y. Zhao, J. Jiang, Recent Progress on Neuromorphic Synapse Electronics: From Emerging Materials, Devices, to Neural Networks, J. Nanosci. Nanotechnol. 18 (2018) 8003–8015. doi:10.1166/jnn.2018.16428.

[106] H. Jeong, Memristor devices for neural networks, J. Phys. D. Appl. Phys. 52 (2018) 1–28.

[107] J. Benda, A.V.M. Herz, A Universal Model for Spike-Frequency Adaptation, Neural Comput. 15 (2003) 2523–2564. doi:10.1162/089976603322385063.

[108] Oxford Living Dictionaries, English, (n.d.). https://en.oxforddictionaries.com/definition/sensor (accessed December 11, 2018).

[109] G. Korotcenkov, Metal oxides for solid-state gas sensors: What determines our choice?, Mater. Sci. Eng. B Solid-State Mater. Adv. Technol. 139 (2007) 1–23. doi:10.1016/j.mseb.2007.01.044.

[110] O. Lupan, V. Postica, N. Wolff, O. Polonskyi, V. Duppel, V. Kaidas, E. Lazari, N. Ababii, F. Faupel, L. Kienle, R. Adelung, Localized Synthesis of Iron Oxide Nanowires and Fabrication of High Performance Nanosensors Based on a Single Fe 2 O 3 Nanowire, Small. 13 (2017) 1602868. doi:10.1002/smll.201602868.

[111] O. Lupan, V. Cretu, V. Postica, N. Ababii, O. Polonskyi, V. Kaidas, F. Schütt, Y.K. Mishra, E. Monaico, I. Tiginyanu, V. Sontea, T. Strunskus, F. Faupel, R. Adelung, Enhanced ethanol vapour sensing performances of copper oxide nanocrystals with mixed phases, Sensors Actuators, B Chem. 224 (2016) 434–448. doi:10.1016/j.snb.2015.10.042.

[112] A. Mirzaei, S.G. Leonardi, G. Neri, Detection of hazardous volatile organic compounds (VOCs) by metal oxide nanostructures-based gas sensors: A review, Ceram. Int. 42 (2016) 15119–15141. doi:10.1016/j.ceramint.2016.06.145.

[113] D.R. Miller, S.A. Akbar, P.A. Morris, Nanoscale metal oxide-based heterojunctions for gas sensing: A review, Sensors Actuators, B Chem. 204 (2014) 250–272. doi:10.1016/j.snb.2014.07.074.

[114] S.-B. Choi, J.K. Lee, W.S. Lee, T.G. Ko, C. Lee, Optimization of the Pt Nanoparticle Size and Calcination Temperature for Enhanced Sensing Performance of Pt-Decorated In2O3 Nanorods, J. Korean Phys. Soc. 73 (2018) 1444–1451. doi:10.3938/jkps.73.1444.

[115] Z. Yuan, J. Zhang, F. Meng, Y. Li, R. Li, Y. Chang, J. Zhao, E. Han, S. Wang, Highly Sensitive Ammonia Sensors Based on Ag-Decorated WO 3 Nanorods, IEEE Trans. Nanotechnol. 17 (2018) 1252–1258. doi:10.1109/TNANO.2018.2871675.

[116] B. Huang, Y. Wang, Q. Hu, X. Mu, Y. Zhang, J. Bai, Q. Wang, Y. Sheng, Z. Zhang, E.

Xie, A low temperature and highly sensitive ethanol sensor based on Au modified In2O3 nanofibers by coaxial electrospinning, J. Mater. Chem. C. 6 (2018) 10935–10943. doi:10.1039/c8tc03669a.

[117] H. Zhang, Y. Wang, X. Zhu, Y. Li, W. Cai, Bilayer Au nanoparticle-decorated WO3 porous thin films: On-chip fabrication and enhanced NO2 gas sensing performances with high selectivity, Sensors Actuators B Chem. 280 (2019) 192–200. doi:10.1016/j.snb.2018.10.065.

[118] K. Diao, J. Xiao, Z. Zheng, X. Cui, Enhanced sensing performance and mechanism of CuO nanoparticle-loaded ZnO nanowires: Comparison with ZnO-CuO core-shell nanowires, Appl. Surf. Sci. 459 (2018) 630–638. doi:10.1016/j.apsusc.2018.07.112.

[119] S. Park, Enhancement of hydrogen sensing response of ZnO nanowires for the decoration of WO3 nanoparticles, Mater. Lett. 234 (2019) 315–318. doi:10.1016/j.matlet.2018.09.129.

[120] C. Clavero, Plasmon-induced hot-electron generation at nanoparticle/metal-oxide interfaces for photovoltaic and photocatalytic devices, 8 (2014). doi:10.1038/nphoton.2013.238.

[121] K. Marchuk, K.A. Willets, Localized surface plasmons and hot electrons, Chem. Phys. 445 (2014) 95–104. doi:10.1016/j.chemphys.2014.10.016.

[122] N.T. Films, D.C. Ratchford, A.D. Dunkelberger, I. Vurgaftman, C. Owrutsky, P.E. Pehrsson, Quanti fi cation of E ffi cient Plasmonic Hot-Electron Injection in Gold Nanoparticle – TiO 2 Films, (2017). doi:10.1021/acs.nanolett.7b02366.

[123] K. Liu, M. Sakurai, M. Liao, M. Aono, Giant improvement of the performance of ZnO nanowire photodetectors by Au nanoparticles, J. Phys. Chem. C. 114 (2010) 19835–19839. doi:10.1021/jp108320j.

[124] M.M. Arafat, B. Dinan, S.A. Akbar, A.S.M.A. Haseeb, Gas sensors based on one dimensional nanostructured metal-oxides: A review, Sensors (Switzerland). 12 (2012) 7207–7258. doi:10.3390/s120607207.

[125] O. Lupan, V. Postica, R. Adelung, F. Labat, I. Ciofini, U. Schürmann, L. Kienle, L. Chow, B. Viana, T. Pauporté, Functionalized Pd/ZnO Nanowires for Nanosensors, Phys. Status Solidi - Rapid Res. Lett. 12 (2018) 1700321. doi:10.1002/pssr.201700321.

[126] V. Postica, A. Vahl, J. Strobel, D. Santos-Carballal, O. Lupan, A. Cadi-Essadek, N.H. De Leeuw, F. Schütt, O. Polonskyi, T. Strunskus, M. Baum, L. Kienle, R. Adelung, F. Faupel, Tuning doping and surface functionalization of columnar oxide films for volatile organic compounds sensing: Experiments and theory, J. Mater. Chem. A. (2018) 21–27. doi:10.1039/C8TA08985J.

[127] H. Li, S. Wu, P. Hu, D. Li, G. Wang, S. Li, Light and magnetic field double modulation on the resistive switching behavior in BaTiO3/FeMn/BaTiO3trilayer films, Phys. Lett. Sect. A Gen. At. Solid State Phys. 381 (2017) 2127–2130. doi:10.1016/j.physleta.2017.04.039.

[128] A. Vahl, J. Carstensen, S. Kaps, O. Lupan, T. Strunskus, R. Adelung, F. Faupel, Concept and modelling of memsensors as two terminal devices with enhanced capabilities in neuromorphic engineering, Sci. Rep. 9 (2019) 4361. doi:10.1038/s41598-019-39008-5.

[129] B. Zhu, H. Wang, Y. Liu, D. Qi, Z. Liu, H. Wang, J. Yu, M. Sherburne, Z. Wang, X. Chen, Skin-Inspired Haptic Memory Arrays with an Electrically Reconfigurable Architecture, Adv. Mater. 28 (2016) 1559–1566. doi:10.1002/adma.201504754.

[130] S. Chen, Z. Lou, D. Chen, G. Shen, An Artificial Flexible Visual Memory System Based on an UV-Motivated Memristor, Adv. Mater. 30 (2018) 1–9. doi:10.1002/adma.201705400.

[131] M. Ohring, Materials Science of Thin Films, 2nd ed., Academic Press, San Diego,

2002.

[132] D. Depla, S. Mahieu, Reactive Sputter Deposition, Springer Berlin Heidelberg, Berlin, Heidelberg, 2008. doi:10.1007/978-3-540-76664-3.

[133] A. Anders, A structure zone diagram including plasma-based deposition and ion etching, Thin Solid Films. 518 (2010) 4087–4090. doi:10.1016/j.tsf.2009.10.145.

[134] J.A. Thornton, High Rate Thick Film Growth, Annu. Rev. Mater. Sci. 7 (1977) 239–260. doi:10.1146/annurev.ms.07.080177.001323.

[135] W. Stöber, A. Fink, E. Bohn, Controlled growth of monodisperse silica spheres in the micron size range, J. Colloid Interface Sci. 26 (1968) 62–69. doi:10.1016/0021-9797(68)90272-5.

[136] J. Köhler, A. Knauer, The Mixed-Electrode Concept for Understanding Growth and Aggregation Behavior of Metal Nanoparticles in Colloidal Solution, Appl. Sci. 8 (2018) 1343. doi:10.3390/app8081343.

[137] M. Thiele, A. Knauer, D. Malsch, A. Csáki, T. Henkel, J.M. Köhler, W. Fritzsche, Combination of microfluidic high-throughput production and parameter screening for efficient shaping of gold nanocubes using Dean-flow mixing, Lab Chip. 17 (2017) 1487–1495. doi:10.1039/C7LC00109F.

[138] Z. Tian, X. Ge, Y. Wang, J. Xu, Nanoparticles and Nanocomposites With Microfluidic Technology, Elsevier Inc., 2019. doi:10.1016/B978-0-12-815067-2.00001-9.

[139] A. Slistan-Grijalva, R. Herrera-Urbina, J.F. Rivas-Silva, M. Ávalos-Borja, F.F. Castillón-Barraza, A. Posada-Amarillas, Assessment of growth of silver nanoparticles synthesized from an ethylene glycol-silver nitrate-polyvinylpyrrolidone solution, Phys. E Low-Dimensional Syst. Nanostructures. 25 (2005) 438–448. doi:10.1016/j.physe.2004.07.010.

[140] S. Veziroglu, M.Z. Ghori, M. Kamp, L. Kienle, H.-G. Rubahn, T. Strunskus, J. Fiutowski, J. Adam, F. Faupel, O.C. Aktas, Photocatalytic Growth of Hierarchical Au Needle Clusters on Highly Active TiO 2 Thin Film, Adv. Mater. Interfaces. 5 (2018) 1800465. doi:10.1002/admi.201800465.

[141] M.T. Nguyen, T. Yonezawa, Y. Wang, T. Tokunaga, Double target sputtering into liquid: A new approach for preparation of Ag-Au alloy nanoparticles, Mater. Lett. 171 (2016) 75–78. doi:10.1016/j.matlet.2016.02.047.

[142] M. Petr, O. Kylián, A. Kuzminova, J. Kratochvíl, I. Khalakhan, J. Hanuš, H. Biederman, Noble metal nanostructures for double plasmon resonance with tunable properties, Opt. Mater. (Amst). 64 (2017) 276–281. doi:10.1016/j.optmat.2016.12.021.

[143] H.T. Beyene, V.S.K. Chakravadhanula, C. Hanisch, M. Elbahri, T. Strunskus, V. Zaporojtchenko, L. Kienle, F. Faupel, Preparation and plasmonic properties of polymer-based composites containing Ag-Au alloy nanoparticles produced by vapor phase co-deposition, J. Mater. Sci. 45 (2010) 5865–5871. doi:10.1007/s10853-010-4663-5.

[144] N. Alissawi, V. Zaporojtchenko, T. Strunskus, I. Kocabas, V.S.K. Chakravadhanula, L. Kienle, D. Garbe-Schönberg, F. Faupel, Effect of gold alloying on stability of silver nanoparticles and control of silver ion release from vapor-deposited Ag-Au/polytetrafluoroethylene nanocomposites, Gold Bull. 46 (2013) 3–11. doi:10.1007/s13404-012-0073-6.

[145] H. Haberland, M. Karrais, M. Mall, Y. Thurner, Thin films from energetic cluster impact: A feasibility study, J. Vac. Sci. Technol. A Vacuum, Surfaces, Film. 10 (1992) 3266–3271. doi:10.1116/1.577853.

[146] A.M. Ahadi, V. Zaporojtchenko, T. Peter, O. Polonskyi, T. Strunskus, F. Faupel, Role of oxygen admixture in stabilizing TiOx nanoparticle deposition from a gas

aggregation source, J. Nanoparticle Res. 15 (2013). doi:10.1007/s11051-013-2125-0.

[147] Y. Huttel, L. Martínez, A. Mayoral, I. Fernández, Gas-phase synthesis of nanoparticles: present status and perspectives, MRS Commun. 8 (2018) 947–954. doi:10.1557/mrc.2018.169.

[148] Y. Huttel, Gas-Phase Synthesis of Nanoparticles, Wiley-VCH, 2017. doi:10.1002/9783527698417.

[149] A. Vahl, J. Strobel, W. Reichstein, O. Polonskyi, T. Strunskus, L. Kienle, F. Faupel, Single target sputter deposition of alloy nanoparticles with adjustable composition via a gas aggregation cluster source, Nanotechnology. 28 (2017) 175703. doi:10.1088/1361-6528/aa66ef.

[150] V.N. Popok, Cluster Beam Synthesis of Polymer Composites with Nanoparticles, Elsevier Inc., 2019. doi:10.1016/B978-0-12-815067-2.00002-0.

[151] F. Faupel, V. Zaporojtchenko, T. Strunskus, M. Elbahri, Metal-polymer nanocomposites for functional applications, Adv. Eng. Mater. 12 (2010) 1177–1190. doi:10.1002/adem.201000231.

[152] H. Hartmann, V.N. Popok, I. Barke, V. Von Oeynhausen, K.H. Meiwes-Broer, Design and capabilities of an experimental setup based on magnetron sputtering for formation and deposition of size-selected metal clusters on ultra-clean surfaces, Rev. Sci. Instrum. 83 (2012). doi:10.1063/1.4732821.

[153] M. Hanif, R.R. Juluri, M. Chirumamilla, V.N. Popok, Poly(methyl methacrylate) composites with size-selected silver nanoparticles fabricated using cluster beam technique, J. Polym. Sci. Part B Polym. Phys. 54 (2016) 1152–1159. doi:10.1002/polb.24021.

[154] S. Pratontep, S.J. Carroll, C. Xirouchaki, M. Streun, R.E. Palmer, Size-selected cluster beam source based on radio frequency magnetron plasma sputtering and gas condensation, Rev. Sci. Instrum. 76 (2005). doi:10.1063/1.1869332.

[155] B. Von Issendorff, R.E. Palmer, A new high transmission infinite range mass selector for cluster and nanoparticle beams, Rev. Sci. Instrum. 70 (1999) 4497–4501. doi:10.1063/1.1150102.

[156] K. Wegner, P. Piseri, H.V. Tafreshi, P. Milani, Cluster beam deposition: A tool for nanoscale science and technology, J. Phys. D. Appl. Phys. 39 (2006). doi:10.1088/0022-3727/39/22/R02.

[157] F. Di Fonzo, A. Gidwani, M.H. Fan, D. Neumann, D.I. Iordanoglou, J.V.R. Heberlein, P.H. McMurry, S.L. Girshick, N. Tymiak, W.W. Gerberich, N.P. Rao, Focused nanoparticle-beam deposition of patterned microstructures, Appl. Phys. Lett. 77 (2000) 910–912. doi:10.1063/1.1306638.

[158] J. Kousal, A. Shelemin, M. Schwartzkopf, O. Polonskyi, J. Hanuš, P. Solař, M. Vaidulych, D. Nikitin, P. Pleskunov, Z. Krtouš, T. Strunskus, F. Faupel, S. V. Roth, H. Biederman, A. Choukourov, Magnetron-sputtered copper nanoparticles: lost in gas aggregation and found by in situ X-ray scattering, Nanoscale. 10 (2018) 18275–18281. doi:10.1039/C8NR06155F.

[159] A. Vahl, J. Dittmann, J. Jetter, S. Veziroglu, S. Shree, N. Ababii, O. Lupan, O.C. Aktas, T. Strunskus, E. Quandt, R. Adelung, S.K. Sharma, F. Faupel, The impact of O2 /Ar ratio on morphology and functional properties in reactive sputtering of metal oxide thin films, Nanotechnology. 30 (2019) 235603. doi:10.1088/1361-6528/ab0837.

[160] E. Fuchs, H. Oppolzer, H. Rehme, Particle Beam Microanalysis, 1st ed., VCH Verlagsgesellschaft mbH, Weinheim, 1990.

[161] D.B. Williams, C.B. Carter, Transmission Electron Microscopy, 2nd ed., Springer Science+Business Media, New York, 2009.

[162] Z. Wang, M. Rao, R. Midya, S. Joshi, H. Jiang, P. Lin, W. Song, S. Asapu, Y. Zhuo, C. Li, H. Wu, Q. Xia, J.J. Yang, Threshold Switching of Ag or Cu in Dielectrics: Materials, Mechanism, and Applications, Adv. Funct. Mater. 28 (2018) 1–19. doi:10.1002/adfm.201704862.

[163] S. Dirkmann, M. Ziegler, M. Hansen, H. Kohlstedt, J. Trieschmann, T. Mussenbrock, Kinetic simulation of filament growth dynamics in memristive electrochemical metallization devices, J. Appl. Phys. 118 (2015) 214501. doi:10.1063/1.4936107.

[164] P. Grammatikopoulos, J. Kioseoglou, A. Galea, J. Vernieres, M. Benelmekki, R.E. Diaz, M. Sowwan, Kinetic trapping through coalescence and the formation of patterned Ag-Cu nanoparticles, Nanoscale. 8 (2016) 9780–9790. doi:10.1039/c5nr08256k.

[165] Z. Wang, S. Joshi, S.E. Savel'ev, H. Jiang, R. Midya, P. Lin, M. Hu, N. Ge, J.P. Strachan, Z. Li, Q. Wu, M. Barnell, G.L. Li, H.L. Xin, R.S. Williams, Q. Xia, J.J. Yang, Memristors with diffusive dynamics as synaptic emulators for neuromorphic computing, Nat. Mater. 16 (2017) 101–108. doi:10.1038/nmat4756.

[166] A. Mehonic, A.L. Shluger, D. Gao, I. Valov, E. Miranda, D. Ielmini, A. Bricalli, E. Ambrosi, C. Li, J.J. Yang, Q. Xia, A.J. Kenyon, Silicon Oxide (SiO x): A Promising Material for Resistance Switching?, Adv. Mater. 30 (2018) 1801187. doi:10.1002/adma.201801187.

[167] S. Tappertzhofen, I. Valov, T. Tsuruoka, T. Hasegawa, R. Waser, M. Aono, Generic relevance of counter charges for cation-based nanoscale resistive switching memories, ACS Nano. 7 (2013) 6396–6402. doi:10.1021/nn4026614.

[168] S. Tappertzhofen, R. Waser, I. Valov, Impact of the Counter-Electrode Material on Redox Processes in Resistive Switching Memories, ChemElectroChem. 1 (2014) 1287–1292. doi:10.1002/celc.201402106.

[169] Rebooting the IT revolution: A call to action, (n.d.). https://www.src.org/newsroom/rebooting-the-it-revolution.pdf (accessed November 28, 2018).

[170] M. Ueki, K. Takeuchi, T. Yamamoto, A. Tanabe, N. Ikarashi, M. Saitoh, T. Nagumo, H. Sunamura, M. Narihiro, K. Uejima, K. Masuzaki, N. Furutake, S. Saito, Y. Yabe, A. Mitsuiki, K. Takeda, T. Hase, Y. Hayashi, Low-power embedded ReRAM technology for IoT applications, in: 2015 Symp. VLSI Technol. (VLSI Technol., IEEE, 2015: pp. T108–T109. doi:10.1109/VLSIT.2015.7223640.

[171] R. Landauer, Irreversibility and Heat Generation in the Computing Process, IBM J. Res. Dev. 5 (1961) 183–191. doi:10.1147/rd.53.0183.

[172] V. V. Zhirnov, R. Meade, R.K. Cavin, G. Sandhu, Scaling limits of resistive memories, Nanotechnology. 22 (2011) 254027. doi:10.1088/0957-4484/22/25/254027.

[173] V. V. Zhirnov, Ultimate Physical Limit of Scaling, in: R. Waser, M. Wuttig (Eds.), Memristive Phenom. - From Fundam. Phys. to Neuromorphic Comput., 1st ed., Forschungszentrum Jülich GmbH, Jülich, 2016: pp. 909–942.

[174] Crossbar Inc., Crossbar ReRAM: Rethinking Simplicity., (n.d.). https://www.crossbar-inc.com/en/technology/reram-overview/ (accessed November 30, 2018).

[175] Crossbar Inc., Crossbar ReRAM Technology Crossbar ReRAM technology Overview, Santa Clara, 2018. https://www.crossbar-inc.com/assets/resources/white-papers/Crossbar-ReRAM-Technology.pdf.

[176] Everspin Technologies, Spin-transfer Torque MRAM Technology, (2018). https://www.everspin.com/spin-transfer-torque-mram-technology (accessed November 30, 2018).

[177] A. Malventano, How 3D XPoint Phase-Change Memory Works, PC Perspect. (2017). https://www.pcper.com/reviews/Editorial/How-3D-XPoint-Phase-Change-Memory-

Works/Selectors-Scaleability-and-Conclusion (accessed November 30, 2018).

[178] Micron, 3D XPoint Technology - Breakthrough Nonvolatile Memory Technology, (2018). https://www.micron.com/products/advanced-solutions/3d-xpoint-technology (accessed November 30, 2018).

[179] T. Register, Deep inside Nantero's non-volatile carbon nanotube RAM tech, (2016). https://www.theregister.co.uk/2016/08/31/nram_dev_nantero_signs_fujitsu (accessed November 30, 2018).

[180] R.G. Larson, T.J. Rehg, Spin Coating, in: Liq. Film Coat., Springer Netherlands, Dordrecht, 1997: pp. 709–734. doi:10.1007/978-94-011-5342-3_20.

[181] S.F. Kistler, P.M. Schweizer, eds., Liquid Film Coating, Springer Netherlands, Dordrecht, 1997. doi:10.1007/978-94-011-5342-3.

[182] C.J. Brinker, G.W. Scherer, Sol-Gel Science, 1st ed., Academic Press, San Diego, 1990.

[183] M. Schlesinger, M. Paunovic, eds., Modern Electroplating, 5th ed., John Wiley & Sons, Inc., Hoboken, 2010.

[184] S. Hoffmann-Eifert, Chemical Vapour Deposition Techniques, in: R. Waser, M. Wuttig (Eds.), Memristive Phenom. - From Fundam. Phys. to Neuromorphic Comput., 1st ed., Forschungszentrum Jülich GmbH, Jülich, 2016: pp. 339–363.

[185] K.K. Gleason, ed., CVD Polymers: Fabrication of Organic Surfaces and Devices, Wiley-VCH, 2015.

[186] J.E. Greene, Review Article: Tracing the recorded history of thin-film sputter deposition: From the 1800s to 2017, J. Vac. Sci. Technol. A Vacuum, Surfaces, Film. 35 (2017) 05C204. doi:10.1116/1.4998940.

[187] R. Dittmann, Physical Deposition Techniques, in: R. Waser, M. Wuttig (Eds.), Memristive Phenom. - From Fundam. Phys. to Neuromorphic Comput., 1st ed., Forschungszentrum Jülich GmbH, Jülich, 2016: p. 365-389.

[188] R. Eason, ed., Pulsed Laser Deposition of Thin Films APPLICATIONS-LED GROWTH OF FUNCTIONAL MATERIALS, John Wiley & Sons, Inc., Hoboken, 2007.

[189] D.B. Chrisey, G.K. Hubler, Pulsed laser deposition of thin films, J. Wiley, New Yok, 1994.

[190] V. Kouznetsov, K. Macák, J.M. Schneider, U. Helmersson, I. Petrov, A novel pulsed magnetron sputter technique utilizing very high target power densities, Surf. Coatings Technol. 122 (1999) 290–293. doi:10.1016/S0257-8972(99)00292-3.

[191] K. Macák, V. Kouznetsov, J. Schneider, U. Helmersson, I. Petrov, Ionized sputter deposition using an extremely high plasma density pulsed magnetron discharge, J. Vac. Sci. Technol. A Vacuum, Surfaces, Film. 18 (2000) 1533–1537. doi:10.1116/1.582380.

[192] J. Böhlmark, Fundamentals of High Power Impulse Magnetron Sputtering, 2006. doi:10.1063/1.3700242.

Appendix A: Overview on the Application of Memristive Devices as Memory

The main motivation to incorporate memristive devices in application scenarios is twofold: On the one hand, memristive devices are under investigation as non-volatile memory (NVM) with advantageous characteristics in conventional computing architectures. On the other hand, the unique electronic properties of memristive devices inspire applications that go beyond conventional electronics, such as neuromorphic engineering. In the main body of this thesis the discussion of the applications of memristive devices is mainly limited to the latter aspect. In order to paint the complete picture, this section serves to give an introduction to memristive devices in the context of memory applications. For a more detailed discussion on this matter the reader is referred to the 2015 report of the Semiconductor Industry Association and Semiconductor Research Corporation [169] and the comprehensive review articles of Daniele Ielmini on memristive switching.[3]

Memristive devices in the context of conventional computing architectures are regarded as an emerging memory technology to complement FLASH and DRAM. In this framework, memristive devices are typically termed resistive random access memory (RRAM or ReRAM). In contrast to DRAM, RRAM is a non-volatile memory and sufficient data retention times have been reported. MIM structures, as commonly used in RRAM, offer the promise of miniaturisation below the footprint of a DRAM cell. At the same time, RRAM is envisioned to outclass FLASH memory in terms of switching speed and energy per written bit.[3,170]

In terms of application as a non-volatile memory, memory devices are typically optimised with respect to the following characteristics: [1]

- The written state should be conserved for a sufficient time period and be undisturbed by a high number of consecutive read operations (Long retention times)
- Low write and read currents (Low power operation)
- Multiple well defined resistance states (Multilevel memory)
- Fast writing speed and low access times (High operation speed)
- Stable switching for a high number of switching cycles (High endurance)
- Small footprint (Miniaturization)
- Reasonable low manufacturing cost (Cost effectiveness)

The search for new, more efficient memory technologies is reasoned in the strong growth of computing and the related energy consumption. In currently available systems, the energy necessary to store a single bit E_b is roughly 10^{-14} J. Assuming a constant growth of the computing power over the next decades, even before the year 2040 the whole world's energy production of today would be consumed solely by computing units.[169] The ultimate limit for the energy necessary to store 1 bit of information is given by the so called Landauer limit, which reasons from the change in entropy upon directed writing: [171]

(A.1) $$E_b = k_B T \cdot \ln(2)$$

At room temperature, this fundamental limit lies in the order of 10^{-21} J, which is roughly 7 orders of magnitude lower than the energy necessary to store a single bit in currently available systems. This limit however does not take into account the memristive switching process itself, which typically involves the transport of metal cations or oxygen vacancies through a solid matrix. In terms of the scaling limits for RRAM devices, according to calculations of Zhirnov et al. already a gap of three atomic layers in between two metal contacts with an area of roughly 1 nm^2 each could represent a memristive device with sufficient retention.[172] Such a device would ideally exhibit a switching energy in the order of 10^{-17} J, more realistically of 10^{-18} J.[173]

So far, RRAM devices with write energies in the order of 10^{-13} J with reasonable retention times and high endurance (over 10^{10} cycles) as well as fast operation speeds (below 10ns) have been reported.[62] In order to fulfil the criteria of fast writing speeds (write typically voltages in the order of 1 V) and long data retention at subsequent read steps (read typically at voltages in the order of 0.1 V), the kinetics involved in the physical switching mechanism have to be strongly nonlinear.[62]

Accordingly, RRAM devices are regarded as promising candidates for future low power memory technologies. However, the reliability of RRAM devices remains one of the strongest concerns, due to the degradation mechanisms connected to the repeated migration of charge carriers under a locally high electric fields (1 $MVcm^{-1}$ and higher are reported) and the locally high current density (in the order of $MAcm^{-2}$).[3] Nevertheless, a number of companies have announced, developed or released a variety of commercial products based on RRAM technology. Some examples of such products and their respective manufacturers include:

- Crossbar Inc. (Application of ECM type devices in a crossbar array) [174,175]
- Everspin Technologies Inc. (Using STT MRAM)[176]
- Intel Corporation and Micron with "3D XPoint" (Probably relying on PCM type devices [177], arranged in a crossbar array)[178]
- Renesas (2Mb ReRAM prototype based on VCM switching) [170]
- Nantero Inc. (Using a carbon nano tube (CNT) array) [179]

Appendix B: Overview on Thin Film Deposition Methods

Thin film deposition methods in general follow one of two main concepts: The target material is brought either through a liquid phase (solution-based methods) or a gas phase (vapour-based methods) to the substrate, where it is deposited and forms a thin film. While the discussion of thin film deposition in the main body of the thesis is limited to the latter approach, in this section a broader overview on the matter of thin film deposition will be given.

Examples for solution based methods include spin coating, spray coating and dip coating.[180,181] These are common processes for polymeric thin films and ceramic thin films (e.g. derived from metal-organic precursors such as metal alkoxides in a sol gel process[182]). The solution in these cases typically contains the target material or its precursor dissolved by a suitable solvent. After the solution is applied to the substrate by spinning, spraying or dipping, the solvent evaporates. The evaporation can be assisted by a heating step. After the solvent is evaporated, a thin film of the target material remains. For the deposition of metallic thin films, electroplating in a liquid electrolyte can be applied. In this approach, due to an electrochemical redox reaction, ions of the target metal are reduced at the substrate surface to form a metallic thin film.[183]

Common vapour-phase-based methods are distinguished between chemical vapour deposition (CVD) and physical vapour deposition (PVD). In classical vapour phase deposition methods, the reaction chamber is evacuated and the flow of gases into the chamber is controlled in order to create a well-defined gas atmosphere. The main characteristic of any CVD process is the occurrence of chemical reactions, which can take place in gas phase and at the substrate surface.[184,185] The underlying processes and reaction equilibria are controlled by the supply rates of the respective feed gases and the specific conditions inside the reaction chamber, which can include the temperature distribution (e.g. substrate temperature and gas temperature), the local concentrations, electric fields and the presence of photon fluxes. Contemporary approaches include an expansion of CVD methods to oxidative (oCVD), hot filament (HFCVD) or plasma enhanced (PECVD) or atomic layer deposition (ALD).[184,185] For the fabrication of memristive devices, the most important CVD techniques are related to the use of metal-organic precursors (MOCVD) and ALD.[184] Closely related to CVD processes are chemical transport processes, such as the reduction of As_2O_3 in the presence of carbon, which dates back to the year 1629, or the Mond process and the van-Arkel-de-Boer process.[186]

In a physical vapour deposition process, atoms of the chosen solid state source (target) are brought into the gas phase and transported to the substrate, where a thin film is formed. Prior to the deposition process the deposition chamber is evacuated in order to increase the mean free path of the respective species in the gas phase. The mean free path λ describes the mean distance that an entity (e.g. an atom or a molecule) with the diameter d travels in between two successive scattering events. In the simplest case, the mean free path additionally depends on the pressure p as well as the temperature T as described in Eq.B.1: [187]

(B.1) $$\lambda = \frac{k_B \cdot T}{\sqrt{2\pi} \cdot p \cdot d^2}$$

In addition, the evacuation of the deposition chamber also ensures the formation of reproducible working conditions with a low level of contaminations.

Commonly, the atoms are brought from the target material into the gas phase either by using the increased vapour pressure due to heating (evaporation and electron beam evaporation), by collisions with high energetic ions (sputtering) or by interaction with a high power photon pulse (pulse laser deposition, PLD). In the following, the basic principle of the sputtering technique and its applicability for the deposition of metallic and oxide thin films will be explained. Further information on the matter of evaporation and PLD can be found in [131,187] and [187–189] respectively.

Sputter deposition processes are widely used in thin film deposition of various materials. A general overview over the historical development of the sputtering method is given by Greene et al..[186] In general, sputter deposition techniques can be classified by the underlying geometry (e.g. parallel plate, magnetron, hollow cathode), by the applied voltage (DC or AC) and by the type of gas atmosphere (inert or reactive) inside the deposition chamber. In its simplest form, a DC sputtering system employs a vacuum chamber in order to guarantee suitable mean free path, in which the anode (substrate) and the cathode (target) are placed. In the parallel plate geometry, both electrodes resemble plates. The system is evacuated and a certain supply of process gases (typically inert noble gases such as argon.) For reactive sputtering, additionally further gas molecules like oxygen or nitrogen can be introduced. In between the anode and the cathode, a high voltage is applied in order to ignite the plasma. This plasma discharge is somewhat comparable to the dielectric breakdown in insulators. In a plasma, a fraction of the neutral gas atoms or molecules is ionised. In this impact ionization process, an electron with a sufficiently high energy collides with a gas neutral G, oxidizing it to a positively charged ion G^+ and yielding a second electron: [131]

(B.2) $$e^- + G \rightarrow G^+ + 2e^-$$

The reaction shown in Eq.B.3 indicates that the number of electrons doubles with this impact ionization process. In case the distance between the electrodes *d* and the operational pressure *p* are chosen adequately, the multiplication of electrons results in an avalanche and consequently an electrical breakdown. The dependency of the necessary breakdown voltage V_b on the electrode distance and the pressure is given by the Paschen's law, where *A* and *B* are constants: [131]

(B.3) $$V_b = A \cdot \frac{p \cdot d}{\ln(p \cdot d) + B}$$

In the resulting plasma, negatively charged electrons, positively charged ions and neutral atoms (or molecules) coexist. Due to the electrical field between the cathode and the anode, positively charged noble gas ions from the plasma are accelerated towards the anode (target).

Atoms from the target material are released upon a collision cascade of the high energy argon ions with the target. In order for the emission of target atoms due to the collision cascade to be effective, the ion energy has to be sufficiently high. The number of sputtered atoms per incident ion is defined as the sputter yield. The sputtered atoms reach the substrate and are deposited there.

The ionization in a DC discharge with parallel plate geometry is typically rather low. In order to increase the ionization, other geometries such as hollow cathode or magnetron sputtering are applied. In hollow cathode sputtering, the planar cathode is replaced by a hollow cylindrical tube. Inside this hollow cathode the mobile electrons undergo a pendulum like motion, allowing for a higher number of collisions with the gas atoms or molecules. Accordingly, the plasma density is significantly enhanced. In case of magnetron sputtering, the cathode is still planar but is modified by introducing a magnetic field. This is typically realised by the usage of permanent magnets, which are placed inside the cathode apparatus below the target material. The magnetic field is chosen such that, due to Lorentz force, the electrons are trapped in a circular motion in an orbit above the target. As a result, the plasma density is significantly enhanced in comparison to parallel plate geometry, which yields a higher deposition rate and allows for stable operation at lower working gas pressures. The possibility to run the sputtering process at lower working pressure relates to fewer collisions of the sputtered atoms with gas atoms before reaching the substrate.

An interesting expansion to conventional magnetron sputtering is High Power Impulse Magnetron Sputtering (HIPIMS), which was developed by Kouznetsov et al. in 1999.[190,191] The technique relies on an increase of the plasma density in the vicinity of the magnetron due to the application of high power pulses. The individual pulses are separated by a long off-time, which allows the target to thermally equilibrate and hence makes high peak powers feasible. A good overview over the topic of HIPIMS is given in the work of J. Böhlmann.[192]